


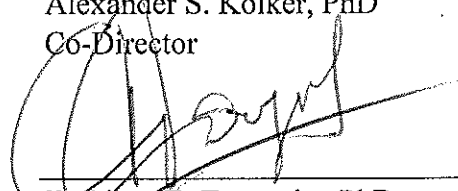
ACCRETION, COMPACTION, AND RESTORATION: SEDIMENT DYNAMICS AND
RELATIVE SEA-LEVEL RISE IN COASTAL WETLANDS

AN ABSTRACT SUBMITTED ON THE EIGHTEENTH DAY OF APRIL 2019
TO THE DEPARTMENT OF EARTH AND ENVIRONMENTAL SCIENCES
IN PARTIAL FULFILLMENT OF THE REQUIREMENTS
OF THE SCHOOL OF SCIENCE AND ENGINEERING
OF TULANE UNIVERSITY
FOR THE DEGREE
OF
DOCTOR OF PHILOSOPHY
BY



Molly E.H. Keogh

APPROVED:


Alexander S. Kolker, PhD
Co-Director


Torbjörn E. Törnqvist, PhD
Co-Director


Mead A. Allison, PhD


Gregg A. Snedden, PhD

ABSTRACT

Over the past two centuries, coastal wetlands have become increasingly threatened by accelerated relative sea-level rise and anthropogenic modification. Engineered structures such as sea walls, levees, and drainage systems prevent natural processes of sediment distribution, reducing the resilience of coastal ecosystems. Land subsidence and shoreline erosion combine with global sea-level rise to make low-elevation coastal zones increasingly vulnerable to submergence. This dissertation examines processes of sediment accumulation, compaction, and relative sea-level rise in coastal wetlands and assesses strategies for restoration. I find that organic content strongly controls sediment compaction in wetland sediments. At least 80% of compaction happens quickly, largely within the first 100 years after deposition and in the top 1 m of the subsurface. This rapid shallow compaction is generally not recorded by traditional methods of measuring relative sea-level rise in low-elevation coastal zones (i.e., tide gauges and global navigation satellite systems). As a result, tide gauges generally underestimate rates of relative sea-level rise in low-elevation coastal zones and these areas may be at a greater risk of flooding than previously realized. However, despite accelerated rates of relative sea-level rise and rapid sediment compaction, coastal restoration efforts such as river diversions can be successful in building new land in some areas. I find that sediment deposition responds non-linearly to water discharge, reaching a maximum at moderate discharge. Wetlands are more likely to keep up with relative sea-level rise if hydrodynamic conditions are optimized to retain mineral sediment in targeted restoration areas.

ACCRETION, COMPACTION, AND RESTORATION: SEDIMENT DYNAMICS AND
RELATIVE SEA-LEVEL RISE IN COASTAL WETLANDS

A DISSERTATION SUBMITTED ON THE EIGHTEENTH DAY OF APRIL 2019

TO THE DEPARTMENT OF EARTH AND ENVIRONMENTAL SCIENCES

IN PARTIAL FULFILLMENT OF THE REQUIREMENTS

OF THE SCHOOL OF SCIENCE AND ENGINEERING

OF TULANE UNIVERSITY

FOR THE DEGREE

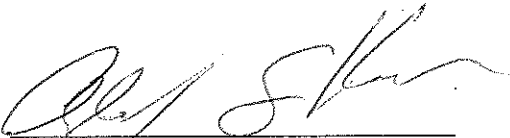
OF

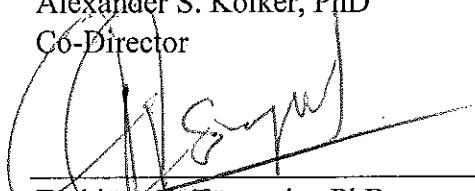
DOCTOR OF PHILOSOPHY

BY

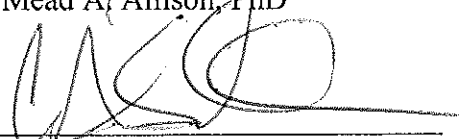

Molly E.H. Keogh

APPROVED:


Alexander S. Kolker, PhD
Co-Director


Torbjörn E. Törnqvist, PhD
Co-Director


Mead A. Allison, PhD


Gregg A. Snedden, PhD

ACKNOWLEDGEMENTS

I am grateful to have had the mentorship of two exceptional graduate advisors during my time at Tulane. Alex Kolker and Torbjörn Törnqvist are both excellent scientists, patient teachers, and genuinely kind and generous people. Thank you, Alex, for believing in me from start to finish. And Tor, thank you for taking me on for a second project, which grew into full-fledged collaboration.

I would also like to thank the other members of my graduate committee. Mead Allison always asked the tough questions, providing perspective that led to better science. Gregg Snedden's willingness to wade into the nitty-gritty of datasheets and calculations with me was greatly appreciated. Thanks also to Gregg for driving the airboat and always keeping us afloat.

Special thanks go to the Earth and Environmental Sciences graduate students for providing such a supportive and fun community. Thanks also to my New Orleans friends, especially Rachel Sortor for being the most reliable friend and board game compatriot, and Chris and Mallory Caterine and Sarah and Tyler Hudson for being top-notch neighbors, barbecuers (the James Beard nomination is surely on its way), and friends who talk about things other than science. I also really appreciate the limitless interest, encouragement, and love from my parents, Peg and John.

Finally, a special thank you to Carl, who is an amazing, supportive partner and brings joy to my life every day.

TABLE OF CONTENTS

ACKNOWLEDGEMENTS	ii
LIST OF TABLES	v
LIST OF FIGURES	vi
INTRODUCTION	1
CHAPTER 1: What is the role of organic matter in delta accretion and subsidence?.....	4
1. Introduction.....	5
2. Data.....	8
2.1. Coastwide Reference Monitoring System (CRMS) cores	9
2.2. Davis Pond cores.....	10
2.3. West Bay cores	10
2.4. Upper Lafourche cores.....	11
2.5. Myrtle Grove I core	11
3. Methods.....	12
3.1. Correcting for differences in sampling methods.....	12
3.2. Calculating effective stress	13
3.3. Calculating percent compaction.....	13
3.4. Calculating compaction rate	15
3.5. Calculating total compaction	15
3.6. Geotechnical modeling	16
4. Results.....	16
4.1. Developing an organic content – bulk density relationship.....	16
4.2. Evaluating the impact of effective stress on sediment compaction	19
4.3. Stratal thickness loss due to compaction	23
4.4. Potential for future compaction	24
4.5. Validity of assumptions	29
5. Discussion	32
5.1. Global variability in peat compaction.....	32
5.2. The future of deltaic wetlands.....	36
6. Conclusions.....	40

CHAPTER 2: Measuring rates of present-day relative sea-level rise in low-elevation coastal zones: A critical evaluation	42
1. Introduction.....	43
2. Data and Methods	48
3. Results.....	50
4. Discussion	55
4.1. Implications for the interpretation of tide gauge and GNSS records.....	55
4.2. An alternative method for measuring present-day rates of relative sea-level rise.....	61
5. Conclusions.....	65
6. Acknowledgements.....	66
CHAPTER 3: Hydrodynamic controls on sediment retention in an emerging diversion-fed delta	68
1. Introduction.....	69
2. Study Area	74
3. Methods.....	78
3.1. Calculation of seasonal sediment input.....	78
3.2. Calculation of Seasonal Sediment deposition.....	80
3.3. Calculation of seasonal sediment retention.....	83
4. Results.....	83
4.1. Geotechnical parameters	83
4.2. Seasonal sediment retention.....	84
5. Discussion	88
5.1. Controls on sediment retention	88
5.1.1. Water discharge, velocity, and turbidity	88
5.1.2. Vegetation	90
5.1.3. Basin geometry and energy level	91
5.2. Comparison with other systems	93
5.3. Implications for coastal restoration.....	95
6. Conclusions.....	100
7. Acknowledgements.....	101
8. Data Availability.....	101
CONCLUSIONS.....	102
LIST OF REFERENCES	104
APPENDICES	135

LIST OF TABLES

Table 1.1. Lithologic designations and geotechnical parameters used for modeling	25
Table 1.2. D-Settlement model results.....	28
Table 2.1. Tide gauges in coastal Louisiana	52
Table 2.2. GNSS stations in coastal Louisiana	55
Table 2.3. Holocene sediment thicknesses of LECZs around the world	60
Table 2.4. Benchmark foundation depths for tide gauges in The Netherlands.....	60
Table 3.1. Summary of parameters affecting sedimentation	86

LIST OF FIGURES

Figure 1.1. Location of 330 sediment cores used for analysis.....	9
Figure 1.2. Organic-matter content vs. depth	19
Figure 1.3. Organic content vs. bulk density	19
Figure 1.4. Effective stress vs. depth	21
Figure 1.5. Effective stress vs. compaction	22
Figure 1.6. Depth vs. compaction rate	23
Figure 1.7. Streamlined stratigraphy used for modeling.....	27s
Figure 1.8. Six model scenarios showing potential compaction.....	28
Figure 2.1. Schematic of a tide gauge and associated benchmark in three environments.	46
Figure 2.2. Location of tide gauges and GNSS stations	51
Figure 2.3. Elevation of the Pleistocene surface.....	54
Figure 2.4. Schematic dip-oriented cross section	54
Figure 2.5. Schematic of combined instrumentation to measure total subsidence	62
Figure 2.6. Probability density functions of mean shallow subsidence rates	64
Figure 3.1. The Mississippi River Delta, southeastern Louisiana, USA	72
Figure 3.2. Discharge and water level at Davis Pond and Mississippi River discharge....	75
Figure 3.3. Turbidity vs. TSS.....	79
Figure 3.4. Spatial patterns in sediment characteristics.....	86
Figure 3.5. Changes in soil geotechnical parameters with distance	87
Figure 3.6. Predicted Mississippi River TSS and predicted TSS input into Davis Pond ..	90
Figure 3.7. Three basin geometry types.....	93
Figure 3.8. Conceptual model of sediment deposition	98

INTRODUCTION

Coastal wetlands are some of the most dynamic environments on Earth, constantly reshaped by competing terrestrial, oceanic, and atmospheric forces. Over the past two centuries, however, coastal wetlands have become increasingly threatened by accelerated relative sea-level rise (RSLR) and anthropogenic modification. Worldwide, more than 625 million people live in river deltas and other low-elevation coastal zones (LECZs), including the populations of megacities such as Shanghai, Lagos, Cairo, and Buenos Aires (Neumann et al., 2015). Engineered structures such as sea walls, levees, and drainage systems prevent natural processes of sediment distribution, reducing the resilience of coastal ecosystems. Land subsidence and shoreline erosion combine with global sea-level rise to make LECZs increasingly vulnerable to submergence.

This dissertation investigates modern processes occurring in coastal wetlands and the challenges of maintaining LECZs in the face of accelerated RSLR. Although the Mississippi Delta serves as the primary study region for this research, many of the processes described here (subsidence, sea-level rise, coastal land loss, and environmental engineering) are often universal. LECZs around the world are at risk of drowning (Syvitski et al. 2009). At the same time, wetlands are highly resilient environments. In this dissertation, I examine how the balance between sediment accretion and subsidence controls coastal wetland growth and decay. The better we understand these processes, the

more prepared we will be to protect critical coastal environments and adapt to changing coastlines.

The first chapter of this dissertation investigates the role of organic material in the accretion and compaction of deltaic wetlands. Outside of active floodplains, modern deltaic wetlands are often organic-rich. In this chapter, I explore the relationships between soil organic content, compaction rate, and overburden mass. Results are used to assess the long-term sustainability of wetlands and to identify a tipping point in organic content, above which wetlands will likely no longer keep up with current and future rates of RSLR over century to millennial timescales.

Because organic-rich strata are susceptible to compaction, wetland soils often experience high rates of subsidence in the shallow subsurface. The second chapter of this dissertation investigates how shallow subsidence affects traditional methods of measuring RSLR. In deltas and other LECZs, tide gauges and GPS stations are typically anchored at depth and do not capture processes occurring above their foundations. As a result, these instruments do not record shallow subsidence, a major component of total subsidence. In LECZs, the accuracy of RSLR projections has major implications for land management, city planning, and flood preparedness.

Even under conditions of reduced sediment supply, rapid compaction, and the resulting high rates of RSLR, it remains possible to build new land in some targeted areas. The third chapter presented here explores options for coastal restoration. Specifically, I investigate how hydrology affects sedimentation within a delta plain. Maximizing mineral sediment retention increases the likelihood that wetlands will

successfully keep up with RSLR. Results show that sediment deposition responds non-linearly to water discharge, reaching an optimum at moderate discharge. I use these results to make recommendations for the operation of river diversions, an emerging restoration tool that reconnects rivers to their floodplains through engineered channels and restart natural land-building processes.

The chapters of this dissertation provide a three-pronged approach to understanding the processes that control the growth and decay of modern coastal wetlands. In the current era of accelerated RSLR, understanding these processes will help refine plans for coastal protection and restoration.

CHAPTER 1: WHAT IS THE ROLE OF ORGANIC MATTER IN DELTA ACCRETION AND SUBSIDENCE?

Molly Keogh, Torbjörn Törnqvist, Alexander Kolker, and Gilles Erkens

ABSTRACT

Globally, mineral sediment supply to deltaic wetlands has generally decreased as a result of the construction of levees and other flood-control infrastructure. As a result, in deltas with intact wetlands ecosystems, wetland sediments have become increasingly organic-rich. Because organic-rich sediments, especially peats, tend to be more compressible than their organic-poor counterparts, many modern wetlands are vulnerable to compaction, subsidence, and conversion to open water. Using a combination of sediment core data and numerical modeling, we examine organic-rich facies in the Mississippi Delta in order to identify the depth range and timescales over which most sediment compaction occurs. By comparing the bulk densities of sediments at the surface with similar deposits buried at depth, we quantify the thickness lost to compaction and investigate whether organic-rich sediments are able to maintain sufficient volume for the overlying wetlands to keep pace with relative sea-level rise. We find that organic content strongly controls sediment compaction. Most compaction occurs in the top 1 m of the

subsurface and within the first 100 years after deposition. The compaction rate decreases rapidly with depth and time. At a site in the Mississippi Delta with nearly 40 m of Holocene strata, the Holocene sediment package has already lost ~24% of its potential thickness due to compaction. In other areas, the top ~3-5 m of sediments are even more extensively compacted (~46-59%). Over 100-year timescales, renewed sediment deposition in highly organic-rich wetlands may cause more elevation loss to compaction than is gained due to accretion. On the other hand, marshes overlying crevasse splays and other organic-poor lithologies may support the weight of renewed deposition and allow net elevation gain. For example, the Mid-Barataria Sediment Diversion, which is currently planned for the lower Mississippi Delta, will likely cause another ~0.35-1.13 m of compaction but leave a net elevation gain of ~0.01-1.75 m.

1. INTRODUCTION

In many modern deltas, mineral sediment supply to the deltaic plain has decreased dramatically since the mid-20th century, largely due to the construction of dams, levees, and other flood-control infrastructure (Syvitski et al., 2005; Syvitski and Saito, 2007; Giosan et al., 2014). In the Yangtze and Mississippi Rivers, for example, dams have reduced the suspended sediment concentration by >40% and 50%, respectively (Yang et al., 2006; Blum and Roberts, 2009). Globally, 40% of river discharge is intercepted by large-capacity reservoirs (Vörösmarty et al., 2003), which have trapped more than 100 billion tons of sediment (Syvitski et al., 2005). Artificial levees prevent overbank deposition and the remaining sediment from reaching deltaic wetlands. Although wetlands may receive some mineral sediment through tidal exchange (e.g., Stevenson et

al., 1988), the turbidity of coastal waters has generally decreased as a result of increased sediment trapping on land (Syvitski et al., 2005). With reduced mineral sediment input, coastal wetlands must rely on the accumulation of organic matter to keep pace with sea-level rise. Reductions in mineral sediment supply are particularly important in areas such as river deltas where high subsidence rates lead to elevated rates of relative sea-level rise (Giosan et al., 2014). If relative sea-level rise exceeds vertical accretion, wetlands typically drown and convert to open water.

Previous work has debated the respective importance of organic and mineral matter in delta accretion. Because organic-rich sediments, especially peats, are typically more compressible than their organic-poor counterparts, many modern coastal wetlands are vulnerable to compaction-driven subsidence and conversion to open water resulting from the drowning and die-off of vegetation (e.g., Kaye and Barghoorn, 1964; Törnqvist et al., 2008; Van Asselen et al., 2010). Organic-poor marine muds are also highly compressible (Baldwin, 1971; Rieke and Chilingarian, 1974; Minderhoud et al., 2018; Zoccarato et al., 2018) and may be at least as compressible as organic-rich sediments in some cases (e.g., Chamberlain, 2017). Additionally, organic-poor marshes may also be less prone to storm-driven erosion than adjacent organic-rich marshes, making them especially important as coastal buffers (Amer et al., 2017).

Despite its compressibility, organic matter is an important component of accretion in some locations. For example, in fresh, intermediate, and brackish marshes of the modern Mississippi Delta, Nyman et al. (1990) found that in the top 38-50 cm, organic matter occupies 27-198% more sediment volume than mineral matter. This is likely

universally true for unconsolidated peats because of the low density of organic matter compared to mineral matter. Turner et al. (2002) found that vertical accretion in coastal marshes is related to organic accumulation but not sediment bulk density and suggested that there is a minimum rate of organic accumulation (but not mineral accumulation) necessary to for saltmarshes to survive RSLR. Similarly, Nyman et al. (2006) found that in the top 45-55 cm, vertical accretion is more closely correlated with organic accumulation rate than with mineral accumulation rate. Going further, Turner et al. (2006) studied sedimentation rates in cores up to ~40 cm in length using the radioisotopes ^{210}Pb and ^{137}Cs and concluded that organic accumulation controls vertical accretion over timescales of up to a century. In a review of 76 tidal freshwater marshes in North America and Europe, including both organic- and clastic-dominated systems, Neubauer (2008) quantified the relative importance of organic matter in the top ~30 cm and concluded that 62% of marsh accretion is due to organic accumulation and the remaining 38% is due to mineral sedimentation.

Sediment bulk density is known to increase with increasing burial depth (and thus also with time) as a result of compaction. However, details of the bulk density versus depth relationship are not well known. Near the surface (0-10 cm depth), coastal wetland sediments typically have very low bulk densities, generally within the range of 0.1-0.6 g cm⁻³ (Marsh et al., 1999; Nyman et al., 2006; Giosan et al., 2013; Keogh et al., 2019). At depth (>2 m), the bulk density of clastic deposits commonly reaches 1.5 g cm⁻³ (Kuecher et al. 1993; Brevik and Homburg, 2004). Jankowski et al. (2017) found that the majority of sediment compaction in the Mississippi Delta occurs in the top 5-10 m of strata,

suggesting that sediment bulk density may increase rapidly with initial burial. The research presented here suggests that this interval of rapid compaction may be restricted to even shallower depths.

In the present analysis, we use a combination of sediment core data and modeling to examine organic-rich facies in the Mississippi Delta. We identify the depth range and timescales over which most sediment compaction occurs and predict future compaction-driven surface elevation change. By comparing the bulk density of sediments at the surface with similar deposits buried at depth, we quantify the thickness lost to compaction and investigate whether organic-rich sediments are able to maintain sufficient volume for the overlying wetlands to keep pace with relative sea-level rise. To better understand the role of organic matter in delta accretion, we will test the following hypothesis: the bulk density of organic matter increases non-linearly with burial depth and overburden mass, with a high compaction rate during initial burial that decreases asymptotically to a slow but more constant rate at depth. As a result, the accumulation rate of organic matter in the Mississippi Delta is sufficient for wetlands to keep pace with relative sea-level rise over the short term (years to decades) but not over longer timescales (centuries to millennia) as compaction continues at a slow and steady rate.

2. DATA

To address this hypothesis, we synthesized sediment data from 5 sources consisting of 330 cores previously collected in coastal Louisiana, USA (details provided below). Data associated with each core include dry bulk density, loss-on-ignition (LOI, a

measure of organic content), and geochronology. All data will be released in conjunction with a forthcoming journal article. Core locations are shown in Figure 1.1.

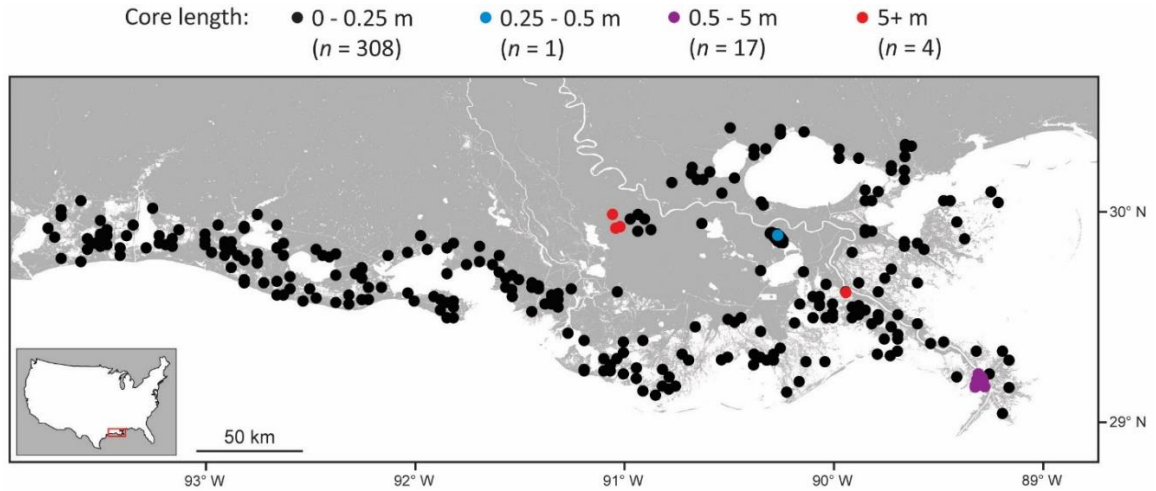


Figure 1.1. Location of 330 sediment cores across the Louisiana coast that were used for analysis. Colors correspond to core length.

2.1. Coastwide Reference Monitoring System (CRMS) cores

The majority of the cores used in this analysis ($n = 264$) were collected across the Louisiana coast as a part of the Coastwide Reference Monitoring System (CRMS; CPRA, 2018). At each CRMS station, three 24-cm sediment cores were collected immediately following site construction. Most CRMS sites were established between 2006 and 2010. Cores were collected by hand and analyzed as described in Folse et al. (2012). CRMS cores included in our analysis have dry bulk density and LOI measurements every 4 cm (for a total of 6 increments per core) and modern vertical accretion rates from feldspar marker horizons as calculated by Jankowski et al. (2017) based on at least 5 years of data collected between 2006 and 2015. Note that the vertical accretion rates postdate the time

interval covered by the cores. For each sample interval, dry bulk density and LOI measurements from each of the three triplicate cores were averaged to produce one value with an error. Linear extrapolation of modern vertical accretion rates was used to estimate the age of buried sediments, which may result in the overestimation of sample ages. The validity of this and other assumptions is discussed in detail in Section 4.5.

2.2. *Davis Pond cores*

Short (0.05-0.5 m) hand cores ($n = 45$) were collected in the receiving basin of the Davis Pond Freshwater Diversion, adjacent to the Mississippi River ~30 river km upstream of New Orleans. These cores were collected by Keogh et al. (2019) in 2015 and 2016. Data for five of these cores are previously unpublished. Dry bulk density, LOI, and activity of the radioisotope ^7Be were measured in 1-cm increments for the top 5 cm and in 5-cm increments below that to the base of the core. ^7Be activity and vertical accretion rates provided in Keogh et al. (2019) were used to estimate the age of buried sediments.

2.3. *West Bay cores*

Seventeen vibracores ~3-5 m in length were collected in the receiving basin of the West Bay Mississippi River Diversion, which is located ~7 km above Head of Passes near the mouth of the Mississippi River. In these cores, dry bulk density, LOI, and activities of the radioisotopes ^{210}Pb and ^{137}Cs were measured in 10-cm intervals (Kolker and Ameen, 2014). ^{210}Pb and ^{137}Cs activities were used to estimate the age of buried sediments. Sediment compaction, which often occurs during the collection of vibracores, ranged from 3-13% of total core length. Core length and bulk density measurements were

corrected for coring-related compaction, assuming that compaction occurred uniformly throughout the core.

2.4. Upper Lafourche cores

Three longer (~12-14 m) cores were collected with a Geoprobe in the upper Bayou Lafourche area near Paincourtville and Napoleonville, Louisiana, in 2014. Dry bulk density and LOI data are available in ~10-cm depth intervals beginning 0.6 m, 3.7 m, and 7.8 m below the surface (Jankowski, 2017). At shallower depths, bulk density and LOI values were estimated based on texture descriptions made in the field. Bulk density values were calculated using subsamples with a known volume collected in the field (Jankowski, 2017). The LOI data are previously unpublished and were provided by K.L. Jankowski. The ages of buried sediments were estimated using ^{14}C and optically stimulated luminescence (OSL) ages measured in organic and clastic sediments, respectively, in adjacent cores (Shen et al., 2015).

2.5. Myrtle Grove I core

In 2016, a 38.7 m piston core was collected near Myrtle Grove, Louisiana, about 2 km from the Mississippi River and ~60 river km downstream of New Orleans, as part of a subsidence monitoring superstation. Dry bulk density and LOI measurements were made at 5-25 cm intervals (Bridgeman, 2018) beginning at a depth of 1.2 m. At shallower depths, bulk density and LOI values were estimated based on texture descriptions. The bulk density values were calculated using subsamples of a known volume collected in the

lab (Bridgeman, 2018). ^{14}C and OSL ages measured in organic and clastic sediments, respectively, ($n = 12$; Bridgeman, 2018) were used to estimate the age of buried deposits.

3. METHODS

Data from 2886 samples in 330 sediment cores were used to assess the vulnerability of wetlands in coastal Louisiana to sediment compaction. In cores with vertical gaps between samples, measurements associated with each sample are assumed to also apply to sediment in the interval in between samples. This interval is defined here as the sample interval, and sample intervals are separated at the mid-point between sample depths. For each sample interval, we calculated effective stress, decompacted dry bulk density, decompacted thickness, percent compaction, and compaction rate. For cores longer than 0.5 m, values were integrated over the length of each core to calculate total compaction. Potential future compaction was modeled using the geotechnical modeling software D-Settlement.

3.1. Correcting for differences in sampling methods

In the Davis Pond and West Bay cores, dry bulk density was calculated using the measured LOI and estimated densities of 2.6 and 1.2 g cm^{-3} for mineral and organic matter, respectively (Adams 1973; Kolker et al. 2009; Morris et al. 2016). For all other cores used in this analysis, bulk density was directly measured using a subsampler with a known volume. Based on a comparison of these two methods using data from the Upper Lafourche and Myrtle Grove I cores, a correction factor of 1.75 was applied to all Davis

Pond and West Bay bulk density values. Details of this comparison are provided in Appendix I.

3.2. *Calculating effective stress*

Using measured values of LOI (%) and dry bulk density (g cm^{-3}) and following the method described in Van Asselen et al. (2018), effective stress (σ' , kPa) is calculated as

$$\sigma' = \sigma - \mu \quad (1)$$

where σ is total stress and μ is pore water pressure. Details are provided in Appendix 1.

For the purposes of this calculation, we assume that the clastic component of all sediments is silty clay loam (35% clay, 55% silt, and 10% sand), a dominant sediment texture in crevasse splays (Esposito et al., 2017), and that the specific gravity of organic matter, clay, silt, and sand is 1.47, 2.70, 2.65, and 2.65 g cm^{-3} , respectively. Although the grain size distribution is a required input for the calculation of effective stress (see Appendix I), the specific gravities of sand, silt, and clay are similar enough that the assumed grain size distribution has essentially no impact on the resulting effective stress value. All other assumptions, including values for pore volume and degree of saturation, are the same as those made in Van Asselen et al. (2018) and are described in Appendix I.

3.3. *Calculating percent compaction*

To calculate sediment compaction, we first identified a subset of near-surface sediment samples in our dataset to be used as a reference for uncompacted material. This

reference dataset includes all of the uppermost samples (0-4 cm) from the CRMS cores. These samples were assumed to be 0% compacted, given that at depths ≤ 4 cm, the sediment has experienced minimal loading from overlying material. The relatively even spacing of the CRMS sites across coastal Louisiana prevents the reference dataset from being biased toward any one region.

The reference dataset was then used to establish a relationship between uncompacted bulk density (ρd_u) and organic content (LOI). Using the TableCurve 2D software (<http://www.sigmaplot.co.uk/products/tablecurve2d/tablecurve2d.php>), 75 equations were tested for goodness-of-fit. Only monotonic equations with no more than three parameters were considered. The resulting best-fit relationship and measured LOI values were then used to estimate the uncompacted bulk density of sediment samples at the time of deposition, before they were buried and subjected to loading.

Samples included in the reference dataset were excluded from subsequent analyses. For the remainder of samples, a distinction was made between organic-rich sediments ($LOI \geq 26\%$) and organic-poor sediments ($LOI < 26\%$). Above $\sim 26\%$ organic content, mineral grains in a typical wetland sediment lose contact with one another and the sediment becomes supported by a matrix of organic matter (Den Haan and Kruse, 2007; Erkens et al., 2016).

Following Van Asselen (2011), the change in bulk density due to loading was used to calculate the uncompacted thickness of each sample interval (h_u):

$$h_u = (\rho d_c / \rho d_u) \times h_c \quad (2)$$

where h_c and ρd_c are the measured (compacted) interval thickness and bulk density, respectively. Because processes of accretion and compaction occur simultaneously, h_u is a theoretical maximum thickness that may never have existed in reality. Finally, compaction (C , %) was calculated as

$$C = (h_u - h_c) / h_u \times 100 \quad (3)$$

Note that here we are calculating sediment compaction by length, following Van Asselen et al. (2018). In contrast, Van Asselen (2011) calculated compaction by volume, ignoring lateral strain.

3.4. *Calculating compaction rate*

Based on the geochronology and vertical accretion rates available for each core, ages were calculated for all sediment intervals. Intervals were assigned to one of six age bins, indicating the time elapsed since deposition: 0-1 year, 1-10 years, 10-50 years, 50-100 years, 100-500 years, or 500-6000 years. For each interval, sediment compaction rate (R , % yr⁻¹) was calculated as

$$R = C / t \quad (4)$$

where t is the age of the sample in years.

3.5. *Calculating total compaction*

Following Van Asselen et al. (2018), total compaction per core (m) was calculated for all cores ≥ 0.5 m in length using the following equation:

$$\text{total compaction (m)} = \sum h_u - \sum h_c \quad (5)$$

Additionally, we calculated total percent compaction as:

$$\text{total compaction (\%)} = (\sum (h_u - h_c) / \sum h_u) \times 100 \quad (6)$$

3.6. *Geotechnical modeling*

The Deltares geotechnical modeling software D-Settlement (version 18.2, <https://www.deltares.nl/en/software/d-settlement-2/>) was used to predict sediment compaction that may occur at the Myrtle Grove site as a result of additional loading of the wetland. D-Settlement is a two-dimensional modeling program that incorporates processes of settlement (vertical lowering due to sediment compression and the resulting instantaneous volume change), consolidation (time-dependent volume reduction resulting from the release of over-pressurized porewater), and secondary creep (consolidation that continues after the sediment has reached a new pressure equilibrium). A detailed review of these processes is provided by Van Asselen et al. (2009). The Myrtle Grove I core was selected as the basis for modeling because it is nearly 40 m in length and contains features of interest for compaction modeling such as organic-rich intervals and sandier layers.

4. RESULTS

4.1. *Developing an organic content – bulk density relationship*

The 330 sediment cores used for analysis include a total of 2886 sample intervals with paired bulk density and LOI measurements. Of these, 264 sample intervals are included in our reference dataset of uncompacted sediment (samples from CRMS sites at

depths ≤ 4 cm; Figure 1.2). Another 864 samples are organic-rich (i.e., defined here as peat; $\text{LOI} \geq 26\%$) and 1757 samples are organic-poor ($\text{LOI} \leq 26\%$).

For our reference dataset of uncompacted sediments in coastal Louisiana, we find that the best-fit relationship between organic content (LOI) and bulk density (ρd_u) takes the form

$$\rho d_u = a + b \times \text{LOI}^c \quad (7)$$

where $a = -0.211$, $b = 2.247$, and $c = -0.489$ ($r^2 = 0.72$; Figure 1.3). Although this best-fit equation is different from the equation used in Van Asselen (2011), the curves are similar in shape. Our best-fit equation falls slightly below the Van Asselen equation, predicting lower bulk density values for given organic contents. Unlike the equation used in Van Asselen (2011), which was fit to fall just below their reference data cloud of uncompacted peat, our equation was fit to the center of our reference data cloud. We conclude that surface sediments in coastal Louisiana are more pristine than those found in the Rhine-Meuse Delta (which has been extensively modified by humans over the last 1000 years; Erkens et al., 2016) and are more likely to be entirely uncompacted.

Although the Mississippi Delta as a whole is heavily human impacted, our study sites are typically located in relatively pristine, natural wetland environments (i.e., undrained and vegetated with typical wetland plant species). Our best-fit equation and the equation used in Van Asselen (2011) are also similar in shape to the one used by Morris et al. (2016), which examined organic content and bulk density in coastal marshes across the United States. The Morris et al. (2016) equation was determined using an ideal mixing model

and fits to the center of their data cloud, which consists of sediment samples collected primarily in the uppermost 0.5 m (thus including both compacted and uncompacted sediments). The three curves differ the most at their inflection points, which occur at moderately-low LOI values (~5-20%). All three studies include multiple peat types (i.e., wood peat and herbaceous peat), suggesting that the differences we see in organic content bulk density are not due to peat type.

Note that because our best-fit line falls through the center of the reference data cloud, some of the reference data points fall below the line. Additionally, some data points in the dataset used for subsequent analyses also fall below the best-fit line (Figure 1.3). These points end up with negative values for calculated compaction. We do not expect that these intervals are expanding; instead, negative compaction values are likely mathematical artifacts that occur when studying large datasets and spatially variable parameters such as organic content and bulk density. We have chosen to include these samples in our dataset because the negative compaction values represent occasions where our methods under-predict compaction and balance out instances where our method may be over-predicting compaction.

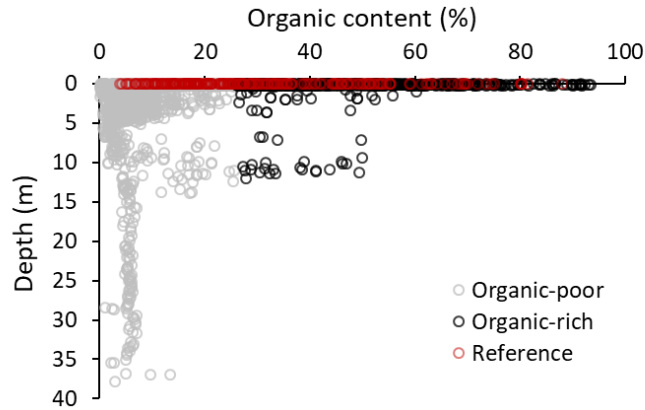


Figure 1.2. Organic-matter content vs. depth for 2886 sample intervals used for analysis. Reference samples (red markers, $n = 265$) are from the top 4 cm of the CRMS cores. Black markers indicate organic-rich samples ($\text{LOI} \geq 26\%$; $n = 864$). Grey markers indicate organic-poor samples ($\text{LOI} < 26\%$, $n = 1757$). Note that the black and grey markers include samples from all depths, excluding the samples that are part of the reference dataset.

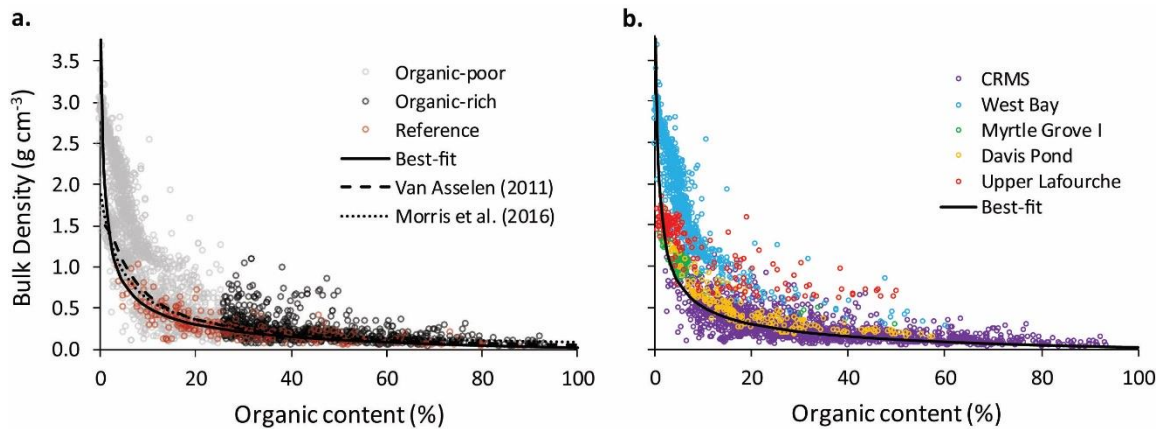


Figure 1.3. Relationship between organic content and bulk density for all 2886 sample intervals, sorted by organic content (a) and data source (b): CRMS ($n = 1584$), West Bay ($n = 808$), Myrtle Grove ($n = 138$), Davis Pond ($n = 194$), and Upper Lafourche ($n = 162$). The solid line in both panels represents the best-fit equation that is used for subsequent analyses in this paper ($r^2 = 0.72$). In panel a, the dashed line and the dotted line represent the best-fit equations used in Van Asselen (2011) and Morris et al. (2016), respectively.

4.2. Evaluating the impact of effective stress on sediment compaction

In the Mississippi Delta, effective stress varies closely with depth (Figure 1.4). In the analyses presented here, effective stress can be thought of as a function of depth for a

first-order interpretation of the relationships. Note that this tight depth-effective stress relationship may be true for locations with relatively homogenous stratigraphy (e.g., Yang and Aplin, 2004) but may be less applicable in regions with more variable stratigraphy.

In general, sediment compaction appears to increase rapidly with initial burial and the corresponding increase in effective stress (Figure 1.5). At ~10 kPa, which corresponds to a depth of ~1.2 m (Figure 1.4), compaction exceeds 45% in most organic-rich samples. At higher effective stresses, the increase in compaction proceeds at a much slower rate. Effective stresses of ~100 kPa correspond to compaction of ~60-80%.

The degree of compaction is controlled in part by organic content (Figure 1.5a and b). In general, sediment with higher organic content is more compacted than less organic-rich sediment under the same effective stress. Although organic content varies by peat type (e.g., Kazemian et al., 2011), compaction has not been shown to be significantly different between peat types (Van Asselen et al., 2018). Notably, although organic-rich samples tend to be more compacted than organic-poor samples, a significant amount of compaction has occurred in sediments with $\leq 26\%$ organic matter (Figure 1.5a and b). In the Myrtle Grove I core, for example, a thick interval of organic-poor silty clay (~11.5-35 m depth) has compacted by $27 \pm 9\%$

Age also appears to have an impact on compaction (Figure 1.5c and d). Logically, older samples tend to be more compacted than younger samples, likely due to higher effective stresses that result from deeper burial. Sediment samples at effective stresses of ~10 kPa, the tipping point above which most sediment compaction appears to have

occurred, are generally in the 50-100 year age bin, suggesting that the bulk of compaction occurs within the first 100 years after deposition. The rate of compaction decreases rapidly with depth, with most compaction occurring in the top 1 m of the subsurface (Figure 1.6). Compaction continues at depths below ~1 m at very slow but steady rates (<1% per year).

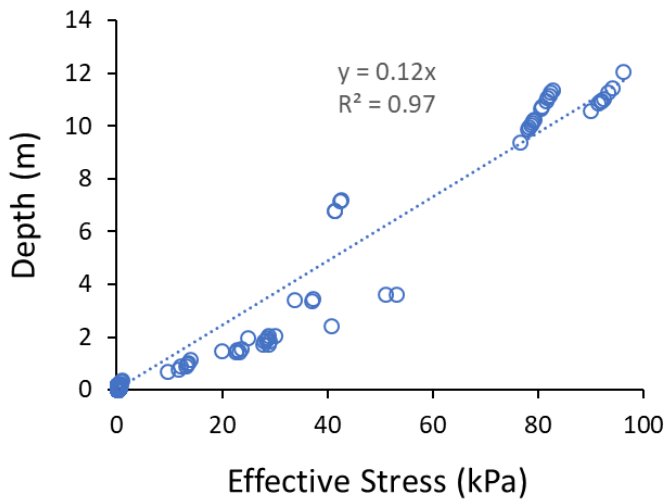


Figure 1.4. Effective stress vs. depth for 864 organic-rich sediment samples. The data shown here include samples from all cores at all depths but exclude the organic-rich samples that are part of the reference dataset.

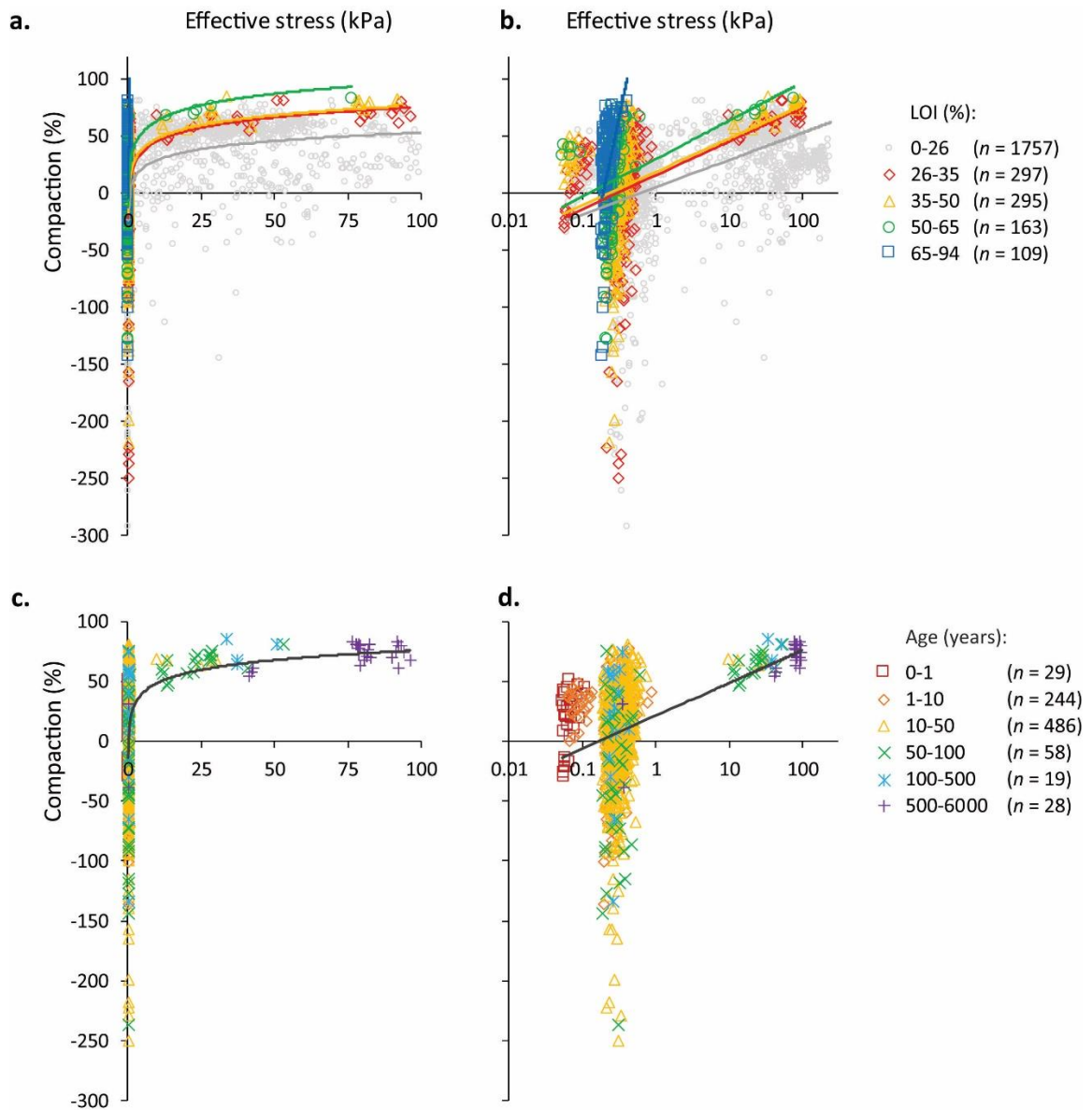


Figure 1.5. Effective stress vs. compaction for 864 organic-rich sediment samples, sorted by organic content (a, b) and age (c, d). In panels a and b, organic-poor samples are shown in grey. Effective stress is plotted on a linear scale in panels a and c and on a log scale in panels b and d. The best-fit logarithmic curves are the same in the right-hand and left-hand panels. For clarity, five organic-poor samples with compaction values of -300% to -600% are not shown.

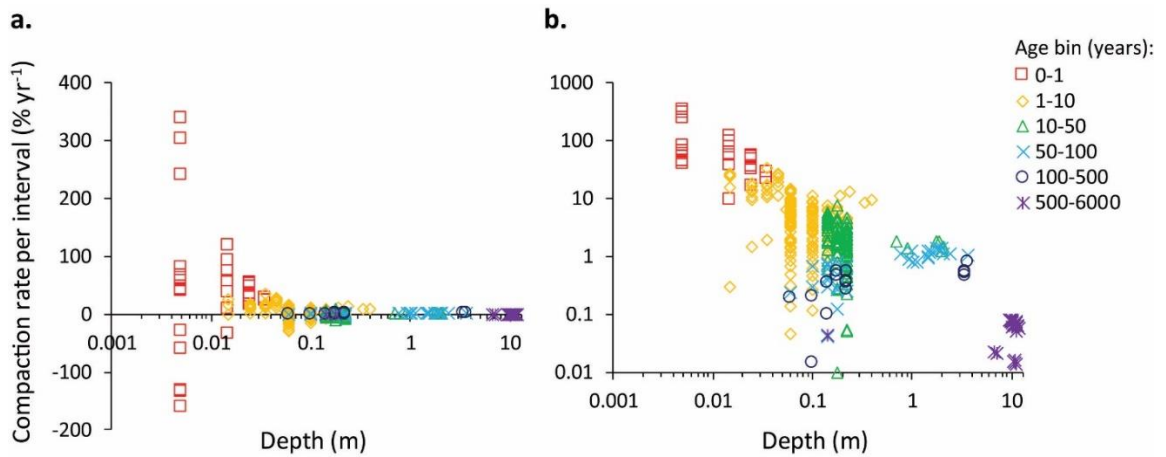


Figure 1.6. Depth vs. compaction rate per sample interval for six age bins of organic-rich sediment. In panel a, depth is shown on a log scale. Panel b shows only samples with positive compaction rates and both depth and compaction rate are plotted on a log scale. The compaction rates presented here correspond to individual sample intervals within a core and thus may not reflect rates occurring throughout a core or seen at the land surface.

4.3. Stratal thickness loss due to compaction

For cores longer than 50 cm, compaction in each sample interval was integrated to calculate the total amount of thickness loss that has occurred due to compaction. Total compaction ranges from 24% to 59% with a mean of $51 \pm 9\%$. At the location of the Myrtle Grove I core, we find that the Holocene sediment package has compacted by 24%, which corresponds to a thickness loss of 11.7 m. Note that processes of sediment accumulation and compaction occur simultaneously and the thickness loss values presented here do not represent true elevation loss. In West Bay, the top 3-5 m of strata have experienced even more extensive compaction ($54 \pm 4\%$), which corresponds to a thickness loss of 5.3 ± 1.1 m. Calculated compaction in the three Upper Lafourche cores ranged from 39-56%, corresponding to thickness losses of 7.7-14.2 m. In Davis Pond, the 0.5-m core was compacted by 31%, resulting in a thickness loss of 0.22 m. Note that the

Upper Lafourche and Myrtle Grove cores lack bulk density and LOI data for the top 0.6-7.8 m so these gaps were filled via estimation based on sediment texture descriptions.

4.4. Potential for future compaction

Although across the Mississippi Delta the Holocene sediment package has already compacted by ~25-60%, modeling using D-Settlement suggests that additional compaction is possible if the wetlands are loaded by renewed sediment deposition. The D-Settlement modeling was completed using the Darcy model of fluid flow through a porous medium and the Netherlands Standardization Institute (NEN) Bjerrum model of settlement, which uses linear strain sediment parameters (listed in Table 1.1 and described below) and follows the international standard for settlement predictions (Deltares, 2018).

In order to streamline the model, the stratigraphy from the Myrtle Grove I core (Bridgeman, 2018) was simplified into six lithologies (Figure 1.7; Table 1.1). Each lithology was given fixed values for the unit weights above and below the phreatic surface, vertical permeability, and over-consolidation ratio (OCR). OCR is a dimensionless parameter defined as the maximum effective stress experienced in the past divided by the present effective stress (Deltares, 2018). The results of a set of preliminary model experiments indicated that larger OCR values lead to extensive autocompaction (i.e., compaction that occurs without loading). For each sediment type, an OCR value was selected in order to limit the role of autocompaction.

Three additional geotechnical parameters were allowed to vary. To bracket a range of likely outcomes, two endmember stratigraphies (“weak stratigraphy” and “stiff stratigraphy”) were modeled for each lithology, using the typical ranges for the reloading/swelling ratio (RR), compression ratio (CR), and the coefficient of secondary compression ($C\alpha$; Table 1.1). RR is used to calculate the settlement that occurs at stresses less than the pre-loading stress. It relates the linear strain to the logarithm of stress during unloading. CR is used to calculate the settlement that occurs at stresses greater than the pre-loading stress. It relates the linear strain to the logarithm of the stress during initial loading. $C\alpha$ is used to calculate the secondary, time-dependent settlement. It relates linear strain to the logarithm of time after initial loading. Note that these three parameters are dimensionless ratios. Complete mathematical definitions are given in the D-Settlement User Manual (Deltares, 2018).

Table 1.1. Lithologic designations and geotechnical input parameters used for modeling. Geotechnical parameter values are from the Netherlands Standardization Institute (2006). Details are provided in Appendix I.

Depth (m)	Lithology	Unit weight above phreatic surface (kN m^{-3})	Unit weight below phreatic surface (kN m^{-3})	Vertical permeability (m s^{-1})	OCR	Weak stratigraphy			Stiff stratigraphy		
						RR	CR	$C\alpha$	RR	CR	$C\alpha$
0-1	Peat	11.00	10.50	5.00E-06	2.00	0.153	0.460	0.023	0.102	0.307	0.015
1-7	Silt loam	20.00	19.00	7.00E-06	1.25	0.011	0.033	0.001	0.008	0.023	0.001
7-10	Silty clay loam	20.00	19.00	1.03E-07	1.50	0.031	0.092	0.004	0.017	0.051	0.002
10-11.5	Sand	22.00	20.00	7.00E-06	1.00	0.004	0.012	0.000	0.002	0.006	0.000
11.5-35	Silty clay	19.00	18.00	7.00E-07	1.75	0.038	0.115	0.005	0.021	0.061	0.003
35-36.5	Sand	22.00	20.00	7.00E-06	1.00	0.004	0.012	0.000	0.002	0.006	0.000

The two stratigraphies were each subjected to three different loads (no loading, small river diversion, large river diversion) for a total of six scenarios. For the small and large diversion scenarios, the load consisted of silty clay loam (with a unit weight of 20 kN m^{-3} above and 19 kN m^{-3} below the phreatic surface) deposited at a rate of 1 cm yr^{-1} and 5 cm yr^{-1} , respectively, for 50 years. These deposition rates are comparable to rates observed seasonally in areas of the Mississippi Delta that are actively receiving river sediments (e.g., Rosenheim et al., 2013; Keogh et al., 2019), and that can persist up to centuries (Shen et al., 2015). Silty clay loam is a dominant sediment texture in crevasse splays (Esposito et al., 2017). The yearly load amount was deposited instantaneously on the first day of each model year. In the no-loading scenarios, an extremely small load was required in order to allow the model to run (a 1 mm-thick deposit with a unit weight of 10 kN m^{-3} above and below the phreatic surface). The groundwater table was set at 10 cm below the land surface for each scenario. The model was allowed to run for 100 years with results available at daily time steps.

At the Myrtle Grove I site, the four modeling scenarios that simulated loading from a river diversion resulted in 0.35-1.13 m of compaction (1.0-3.1%; Figure 1.8). Unlike the theoretical thickness losses reported above (section 4.3), this is an estimate of true thickness loss. For comparison, the two no-loading scenarios produced very minor compaction (0.1-0.2%). Much of the compaction occurred in the peat layer at the top of the sediment column. Although this peat layer is only 1 m thick, it compacted by 25-69%, depending on the loading scenario, and contributed 61-70% of the total compaction. The 23.5-m thick layer of silty clay also contributed significantly to the total compaction.

Although the silty clay compacted by only 0.2-1.1% in the loading scenarios, it contributed 16-23% of the total compaction due to its thickness. Detailed results from all six model scenarios are given in Table 1.2.

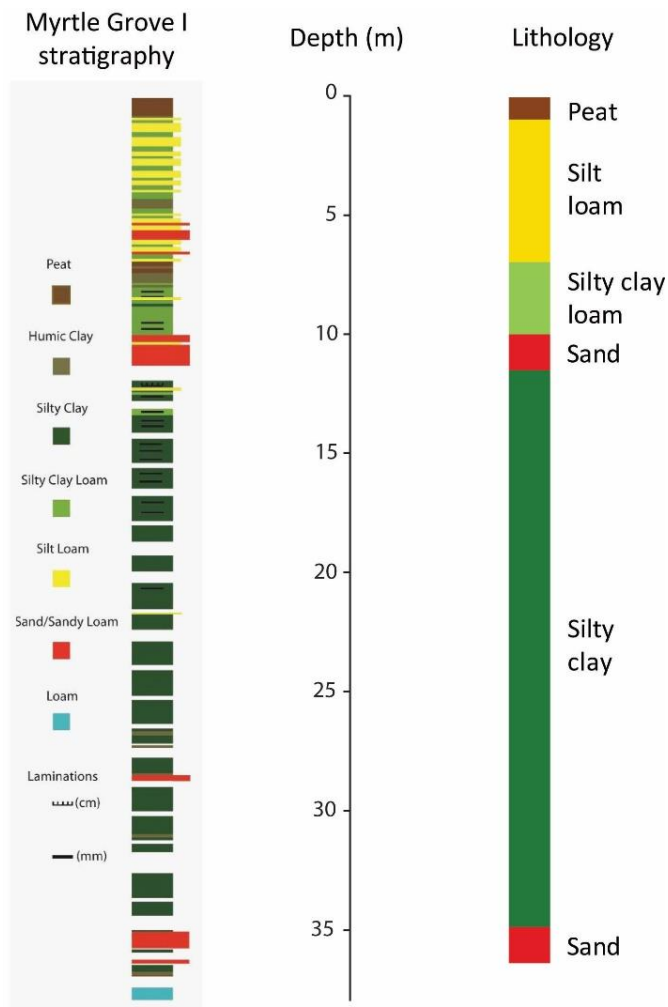


Figure 1.7. To streamline modeling, the stratigraphy in the Myrtle Grove I core [left, from Bridgeman (2018)] was simplified into six lithologies (right).

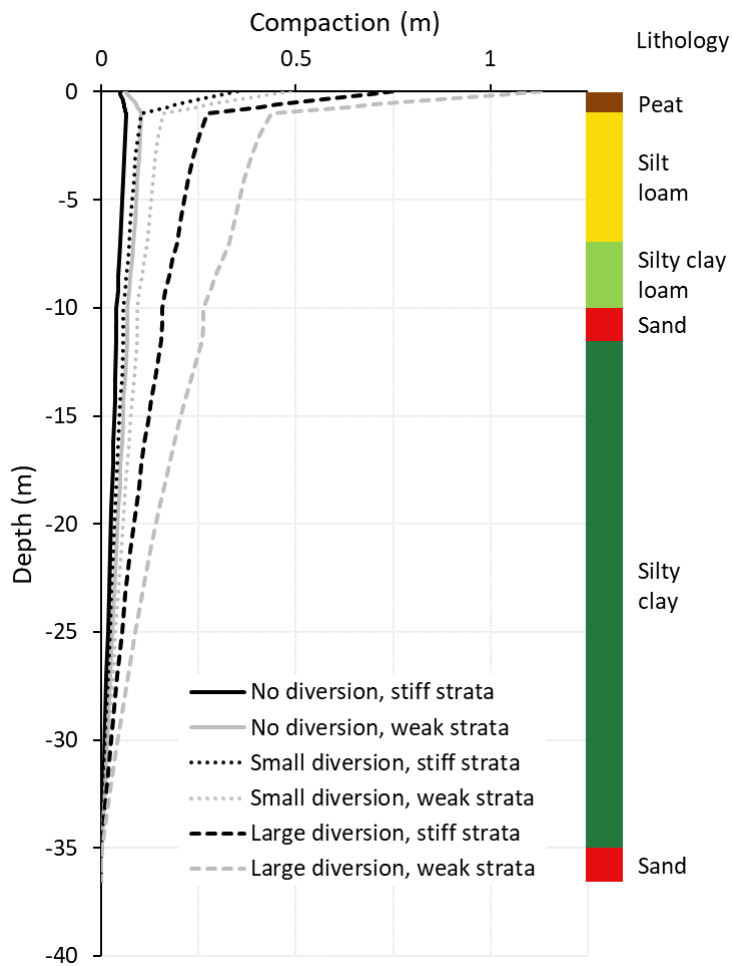


Figure 1.8. Six model scenarios showing potential compaction of the Myrtle Grove I stratigraphy.

Table 1.2. D-Settlement model results of six scenarios showing potential compaction of stratigraphy at the Myrtle Grove I site.

Modeling scenario	Lithology	Original thickness (m)	Compacted thickness (m)	Total compaction (m)	Compaction (% of layer)	Compaction (% of total)	Total accretion (load thickness; m)	Net surface elevation change (m)
No diversion, weak strata	Peat	1	1.04	0.061	-4.20	-66.13	0.001	-0.060
	Silt loam	6	5.98		0.35	33.87		
	Silty clay loam	3	2.98		0.57	27.42		
	Sand (upper)	1.5	1.50		0	0		
	Silty clay	23.5	23.44		0.28	104.84		
	Sand (lower)	1.5	1.50		0	0		

No diversion, stiff strata	Peat	1	1.016	0.047	-1.60	-34.04	0.001	-0.046
	Silt loam	6	5.985		0.25	31.91		
	Silty clay loam	3	2.991		0.30	19.15		
	Sand (upper)	1.5	1.5		0	0		
	Silty clay	23.5	23.461		0.17	82.98		
	Sand (lower)	1.5	1.5		0	0		
Small diversion, weak strata	Peat	1	0.671	0.487	32.90	67.56	0.5	0.013
	Silt loam	6	5.959		0.68	8.42		
	Silty clay loam	3	2.975		0.83	5.13		
	Sand (upper)	1.5	1.499		0.07	0.21		
	Silty clay	23.5	23.409		0.39	18.69		
	Sand (lower)	1.5	1.5		0	0		
Small diversion, stiff strata	Peat	1	0.754	0.349	24.60	70.49	0.5	0.151
	Silt loam	6	5.969		0.52	8.88		
	Silty clay loam	3	2.985		0.50	4.30		
	Sand (upper)	1.5	1.5		0.00	0.00		
	Silty clay	23.5	23.443		0.24	16.33		
	Sand (lower)	1.5	1.5		0	0		
Large diversion, weak strata	Peat	1	0.308	1.130	69.20	61.24	2.5	1.370
	Silt loam	6	5.892		1.80	9.56		
	Silty clay loam	3	2.932		2.27	6.02		
	Sand (upper)	1.5	1.499		0.07	0.09		
	Silty clay	23.5	23.24		1.11	23.01		
	Sand (lower)	1.5	1.499		0.07	0.09		
Large diversion, stiff strata	Peat	1	0.525	0.748	47.50	63.50	2.5	1.752
	Silt loam	6	5.922		1.30	10.43		
	Silty clay loam	3	2.961		1.30	5.21		
	Sand (upper)	1.5	1.498		0.13	0.27		
	Silty clay	23.5	23.346		0.66	20.59		
	Sand (lower)	1.5	1.5		0	0		

4.5. *Validity of assumptions*

Our reference dataset includes samples with good spatial coverage across the Louisiana coast and a broad range of organic contents (4-88%). However, because of the lack of reference data at organic contents below 4%, the shape of the curve is not well constrained at the lower end. Some of the cores used for analysis, particularly the Myrtle

Grove I core, include sediments with very low organic content (i.e., <4%), likely due to the decomposition of organic matter. These most organic-poor samples are not well represented by our reference dataset. Through experimentation with other fit equations, we found that small changes in the shape of the curve can have relatively large changes in calculated compaction.

In each core, vertical accretion rates were linearly extrapolated in order to estimate the age of each sample interval. By using this method, we are assuming that vertical accretion rates are constant through large stretches of time and varied stratigraphy. In reality, accretion rate is likely highly variable. Organic-rich intervals tend to accumulate slowly, whereas organic-poor crevasse splay deposits accumulate more rapidly (e.g., Shen et al., 2015). This variability in accretion rate (and thus age distribution) has implications for our calculations of compaction rate. In West Bay, for example, near-surface sediment samples are likely younger than predicted because accretion rates in the modern diversion-fed wetland are likely higher than longer-term average rates. In contrast, samples at the base of organic-rich intervals at depth are likely older than predicted because the peat likely accumulated at a rate slower than the long-term average. This method of estimating sample age also assumes zero compaction of newly-deposited sediments and thus our calculated ages may be overestimated in some cases. As a result of these assumptions, interpretations should focus on the six age bins used for analysis rather than individual sample ages.

In calculating compaction, we assumed that the clastic component of all sediments is silty clay loam (35% clay, 55% silt, and 10% sand). Although Bird et al.

(2004) determined that the particle size distribution of clastic matter is less important in determining bulk density than is the sediment organic content, Van Asselen et al. (2009) disagreed. In their review of peat compaction studies, Van Asselen et al. (2009) pointed out that sediments enriched in silt and clay are more compacted than sand-rich intervals, suggesting that grain size distribution is in fact an important control on compaction. In the Mississippi Delta, however, wetlands are primarily mud-dominated, with minor sand (e.g., Snedden et al., 2007; Esposito et al., 2017). As a result, our original assumption of grain size distribution is acceptable.

Additionally, we assumed that all sediments, regardless of elevation, are 98% saturated by groundwater. This assumption is reasonable for cores taken at or very near sea level (i.e., those from West Bay and Davis Pond as well as at Myrtle Grove and most CRMS sites). During astronomical and meteorological low tides, however, these locations may experience short-duration drainage of the top ~10-20 cm of sediment, which would then be vulnerable to compaction. Locations near sea-level also periodically experience water loading due to tidal, meteorological, or diversion-driven flooding, which temporarily increases effective stress and may cause additional compaction. Cores at elevations above sea level or in areas with an artificially lowered groundwater table (i.e., those from Upper Lafourche and inland CRMS sites) likely have a permanently drained interval at the surface that is subject to accelerated compaction. In the Upper Lafourche area, the groundwater table is typically a few meters below the land surface. In this study, we do not account for drainage or flooding and thus our estimates of compaction should be considered minimum values.

Our method of calculating compaction produces negative compaction values for some samples. These samples generally fall into one of two main categories: 1) very organic-poor sediments with high bulk density, and 2) very low-bulk density, surficial samples with small (1- to 4-cm) sampling intervals. In the first category, organic content is low enough that other factors are likely more important in controlling bulk density. In the second category, we expect that small changes in thickness that occur over small sampling intervals are leading to exaggerated compaction values. We have included all calculated compaction values, including negative values, in our calculations of total compaction per core. We expect that negative values balance out excessively high values and lead to realistic results. However, our estimates of compaction again should be considered minimum numbers.

5. DISCUSSION

Subsidence driven by the compaction of organic-rich sediment poses a major risk to coastal landscapes, particularly in areas where mineral sediment supply has been reduced. Unlike many other causes of wetland subsidence (e.g., fluid withdrawal, glacial isostatic adjustment, tectonics), compaction-driven subsidence is both large in magnitude and widespread across delta settings globally, making it especially difficult to mitigate (Törnqvist et al., 2008; Teatini et al., 2011; Van Asselen, 2011; Marriner et al., 2012; Zhang et al., 2015; Allison et al., 2016).

5.1. Global variability in peat compaction

In the Mississippi Delta, peat compaction (measured by length) appears to reach a maximum at ~80% (Figure 1.5). Above ~30 kPa (and up to maximum observed effective stresses of ~100 kPa), increases in overburden no longer correspond to significant increases in compaction, suggesting a mechanical limit to compaction potential. The bulk of compaction in organic-rich sediments appears to occur rapidly after initial deposition and burial. In the Mississippi Delta, we find that ~80% of the apparent maximum compaction has occurred by the time sediment samples reach effective stresses of ~10 kPa (Figure 1.5). According to the generalized effective stress versus depth relationship shown in Figure 1.4, an overburden of 10 kPa corresponds to a depth of 1.2 m. However, a closer analysis of changes in compaction rate with depth and age suggests that most compaction occurs in the top 1 m below the land surface and within the first 100 years after deposition (Figure 1.6). Below this depth, the rate of sediment compaction decreases rapidly from ~1% yr⁻¹ to ≤0.1% yr⁻¹.

This rapid decrease in compaction rate occurs on a shorter timescale than suggested by previous studies. In a study of the interior Cumberland Marshes of Canada, Van Asselen et al. (2011) found that most peat compaction coincides with initial loading and occurs primarily within the first few hundred years. Subsidence rates decreased once the peat was buried by ~2 m of overburden, but compaction continued at a slower rate eventually reaching a maximum modeled compaction of ~40%. Similarly, a modeling study of saltmarsh dynamics found that compaction rates decreased dramatically from 5.7 to 1.7 mm yr⁻¹ after 350 years (Zoccarato and Teatini, 2017). These differences in compaction rate through time are likely due to the temporal resolution of each study. Van

Asselen et al. (2011) averaged compaction rates over 50-year time intervals and the initial modeling time step used by Zoccarato and Teatini (2017) was 100 years. Our database of 330 cores includes nearly 2000 sediment samples collected in the uppermost 1 m of the subsurface and within the first 50-100 years after deposition, giving our analysis unparalleled depth-time resolution.

Upper limits to compaction may be variable, perhaps driven by local differences in organic content and affected by processes of peat degradation such as drainage, oxidation, and diagenetic remineralization. In some areas of the Mekong Delta, for example, sediment compaction appears to plateau at ~70% (Zoccarato et al., 2018). In the Rhine-Meuse Delta, the most heavily-loaded sediments have compacted by only ~65%, which corresponds to effective stresses of 60-70 kPa (Van Asselen et al., 2018). The higher compaction values observed in the Mississippi Delta are likely due to the fact that our reference samples have lower bulk densities and are probably more pristine than the reference sediments in the Mekong and Rhine-Meuse deltas.

Due to the relatively thin Holocene sediment package in the Rhine-Meuse Delta (20-25 m; Hijma et al., 2009), natural loading produces effective stresses of generally no more than ~25 kPa (Van Asselen et al. 2018). Although anthropogenic loading can produce effective stresses up to 60-70 kPa, sparse data at high effective stresses makes it difficult to determine if compaction plateaus at an apparent maximum value.

Hypothetical further increases in effective stress may lead to greater compaction in the Rhine-Meuse Delta.

Non-deltaic coastal peats are also subject to extensive compaction. In Singapore, Bird et al. (2004) found that mangrove sediments overlain by up to 9 m of overburden were compacted by up to 67%. This compaction may be driven by drainage during low tide. At a site in the United Kingdom now ~18 km inland from the Bristol Channel, Haslett et al. (1998) found a maximum compaction of 55% in a peat overlain by ~2 m of intertidal clay. Though studies of marshes in coastal Louisiana consistently find that sediment compaction is the primary driver of surface elevation change (Cahoon et al., 1995; Törnqvist et al., 2008), compaction in marshes on the U.S. Atlantic coast is more variable and difficult to interpret. Whereas Bloom (1964) found that peat in a tidal marsh in Connecticut had compacted by 13-44%, meta-analysis of field data from salt marshes on the Atlantic coasts of North America and Europe by Kirwan et al. (2016) suggested that modern rates of sediment compaction are near zero. Compaction rates on the Atlantic coast may be low because marshes in these areas are typically highly organic-rich ($\geq 30\%$ LOI) and thus have low effective stresses (Redfield, 1972; Bricker-Urso et al., 1989; Kolker et al., 2009; Brain et al. 2015).

Some peats may reach higher compaction values because they start out at a lower bulk density. The close coincidence of the Morris et al. (2016) best-fit curve (which represents a combination of compacted and uncompacted sediments) and the Van Asselen (2011) curve (which represents uncompacted sediments only) together with the observation that our best-fit equation for uncompacted sediments underlies both of these other curves suggests that the reference datasets used in these other studies were not

entirely compaction-free. By starting out at lower bulk densities, the relatively pristine wetlands in the Mississippi Delta may have a greater potential for compaction.

5.2. *The future of deltaic wetlands*

In the modern era of accelerated relative sea-level rise, increased sediment accretion will be essential for the survival of many deltas (Giosan et al., 2014). Although wetlands starved of regular sediment deposition tend to rapidly lose elevation (Syvitski et al., 2009), renewed sedimentation can dramatically increase vertical accumulation rates over short timescales. In the Ganges-Brahmaputra Delta, for example, poldered islands have lost up to 1.5 m of elevation while neighboring un-embanked wetlands have remained stable (Auerbach et al., 2015). After catastrophic cyclone-related embankment failure occurred on one poldered island, the interior of the island was reconnected to tidal flooding and sediment accretion rates increased by an order of magnitude. Over two years, tens of cm of new sediment was deposited in the subsided interior of the island (Auerbach et al., 2015). Similarly-high rates of vertical accretion have occurred in the Sacramento-San Joaquin Delta, where leveed islands have subsided by up to 7 m below sea level and intentional flooding resulted in sediment accumulation rates of up to 9 cm yr⁻¹ (Miller et al., 2008).

In the Mississippi Delta, river diversions are one of the primary methods proposed to combat wetland subsidence. Diversions are engineered structures that divert a portion of the river's water, sediment, and nutrient load into an adjacent wetland. In order for diversions to be successful in building land, the thickness of newly deposited sediment must exceed the elevation lost to compaction. Over 100-year timescales, it is possible that

renewed sediment deposition in highly organic-rich wetlands may cause more elevation loss to compaction than is gained due to accretion. On the other hand, marshes overlying crevasse splays and other organic-poor facies may support the weight of renewed deposition and allow for net elevation gain. Low rates of sediment compaction are not necessarily detrimental to wetland building, however. Modeling by Nienhuis et al. (2018) found that the largest crevasse splays form in association with moderate sediment compaction, which provided the accommodation necessary for the accumulation of new material.

The modeling results presented here suggest that the stratigraphy at Myrtle Grove may successfully support the weight of diversion-deposited sediments. Although renewed deposition from a river diversion may cause as much as 1.13 m of compaction, vertical accretion may outpace compaction and result in a net elevation gain of 0.01-1.75 m (Table 1.2). Multiple new river diversions are currently planned for the lower Mississippi Delta, and the success of these diversions will be critical for wetland restoration efforts (CPRA, 2017). Net elevation gain is as much as 12 times greater when the pre-existing strata are stiffer and compaction is limited. Stiffer stratigraphy becomes increasingly important with larger diversions that deposit more sediment. As a result, river diversions must be sited thoughtfully. The results presented here suggest that Myrtle Grove is a good location for the proposed Mid-Barataria Sediment Diversion in terms of compaction and subsidence. Diversions will likely build more sustainable land if they are sited in areas with existing stable stratigraphy (e.g., immediately adjacent to the river atop

existing crevasse splay deposits rather than in more distal, organic-rich inter-distributary basins).

Although river diversions may be viable tools for coastal restoration in relatively organic-poor locations such as Myrtle Grove, other locations in the Mississippi Delta and in deltas around the world are much more organic rich. The Rhine-Meuse Delta, for example, has much more extensive peat deposits (Van Asselen et al., 2018). In this type of environment, deposition of dense, organic-poor sediment from a river diversion may cause more compaction of the peat than is made up for with vertical accretion, rendering the diversion counter-productive. Interestingly, some deltas such as the Mekong have exceedingly high rates of sediment compaction despite being relatively organic-poor (Zoccarato et al., 2018). In the Mississippi Delta, we find that organic-poor sediments are commonly compacted by ~50% and can be compacted by as much as 80% (Figure 1.5a and b). Regardless of organic content, the thickness of the Holocene succession in the Rhine-Meuse Delta is only 20-25 m (Hijma et al., 2009) compared to 25-40 m in the Mekong Delta (Ta et al., 2002; Tanabe et al., 2003b) and 50-100 m in the Mississippi Delta (Heinrich et al., 2015). Even if percent compaction is higher in the Rhine-Meuse Delta due to the high organic content of the sediments, surface elevation change may be greater in the Mississippi Delta.

Some previous studies have suggested that organic accumulation alone may be sufficient for coastal wetlands to keep pace with relative sea-level rise (e.g., Turner, 1997). However, given that organic matter can compact by up to 80%, our findings show that deltas are unlikely to simply grow themselves out of their elevation deficit even if

short-term vertical accretion rates equal or exceed rates of relative sea-level rise. The compaction of both organic-rich and organic-poor sediment leads to vertical displacement of wetland stratigraphy when compared to compaction-free basal peat samples. In coastal North Carolina, where wetland sediment packages are relatively thin (<2 m), Brain et al. (2015) found that stratigraphy was vertically displaced by only ~ 2 cm. In locations with thicker Holocene stratigraphy, however, vertical displacement can be much more extensive. In the Rhine-Meuse Delta, for example, sediments have subsided by as much as ~ 3 m (Van Asselen, 2011). In the Mississippi Delta, vertical displacement rates averaged over millennial timescales are as high as 5 mm yr^{-1} and total displacement is as much as 8 m at Myrtle Grove (Törnqvist et al., 2008; Bridgeman, 2018). This magnitude of displacement is comparable to the calculations of compaction presented here, which suggest that wetland sediments have lost nearly 12 m of thickness to compaction at Myrtle Grove and up to 14 m in Upper Lafourche.

Globally, accelerated subsidence rates are often seen in areas where the groundwater table has been artificially lowered (e.g., Phien-wej et al., 2006; Erban et al., 2014; Higgins et al., 2014; Minderhoud et al., 2017). Drainage of a wetland results in the double effect of reduced pore water pressure, which increases effective stress, and aeration, which causes peat oxidation (e.g., Erkens et al., 2016). One of the best ways to prevent peat compaction is to maintain the pore water pressure, i.e., maintain groundwater levels at or near the surface. As the global population increases, however, groundwater extraction will likely increase in order to reclaim land, prevent flooding, and provide drinking water. Continued extraction may create a feedback cycle of continued

groundwater table lowering and land subsidence (e.g., Erkens et al., 2016). Human manipulation of coastal areas (e.g., groundwater extraction, loading) will likely cause greater compaction in more pristine (i.e., un-drained, un-loaded) and organic-rich landscapes that have lower initial bulk densities. Strategies to limit compaction-related subsidence may become increasingly important as rates of global sea-level rise continue to accelerate and the elevation deficit in deltas and other low-elevation coastal zones increases (e.g., Bettinetti et al., 1996; SFEI-ASC, 2016; CPRA, 2017).

6. CONCLUSIONS

In low-elevation coastal zones, the compaction of organic matter is often an important control on landscape evolution (e.g., Long et al., 2006; Törnqvist et al., 2008; Erkens et al., 2016). In this analysis of sediment compaction in the Mississippi Delta, we identify the depth range and timescales over which most sediment compaction occurs and make predictions regarding future compaction-driven surface elevation change. We reach the following conclusions:

- Organic content strongly controls sediment compaction.
- Sediment compaction rate decreases rapidly with depth and time.
- Most compaction occurs in the top 1 m of the subsurface and within the first 100 years after deposition.
- At Myrtle Grove, Louisiana (near a proposed river diversion site), the Holocene sediment package has already lost 24% of its thickness due to compaction.

- Renewed deposition from the Mid-Barataria Sediment Diversion will likely cause another ~0.35-1.13 m of compaction, increasing total compaction to 25-27%, but leave a net elevation gain of ~0.01-1.75 m.

CHAPTER 2: MEASURING RATES OF PRESENT-DAY RELATIVE SEA-LEVEL RISE IN LOW-ELEVATION COASTAL ZONES: A CRITICAL EVALUATION

Molly E. Keogh and Torbjörn E. Törnqvist

ABSTRACT

Although tide gauges are the primary source of data used to calculate multi-decadal to century-scale rates of relative sea-level change, we question the usefulness of tide-gauge data in rapidly subsiding low-elevation coastal zones (LECZs). Tide gauges measure relative sea-level rise (RSLR) with respect to the base of associated benchmarks. Focusing on coastal Louisiana, the largest LECZ in the United States, we find that these benchmarks ($n = 35$) are anchored an average of 21.5 m below the land surface. Because at least 60% of subsidence occurs in the top 5 m of the sediment column in this area, tide gauges in coastal Louisiana do not capture the primary contributor to RSLR. Similarly, Global Navigation Satellite System (GNSS) stations ($n = 10$) are anchored an average of >14.3 m below the land surface and therefore also do not capture shallow subsidence. As a result, tide gauges and GNSS stations in coastal Louisiana, and likely in LECZs worldwide, systematically underestimate rates of RSLR as experienced at the land surface. We present an alternative approach that explicitly measures RSLR in LECZs

with respect to the land surface and eliminates the need for tide-gauge data in this context. Shallow subsidence is measured by rod surface-elevation table–marker horizons (RSET-MHs) and added to measurements of deep subsidence from GNSS data, plus sea-level rise from satellite altimetry. We show that for a LECZ the size of coastal Louisiana (25,000–30,000 km²), about 40 RSET-MH instruments suffice to collect useful data. Rates of RSLR obtained from this approach are substantially higher than rates as inferred from tide-gauge data. We therefore conclude that LECZs may be at higher risk of flooding, and within a shorter time horizon, than previously assumed.

1. INTRODUCTION

In the current era of accelerated sea-level rise, accurate measurements of relative sea-level change are critical to predict the conditions that coastal areas will face in coming decades and beyond. Such measurements traditionally come from tide gauges, which provide the longest available instrumental records of relative sea-level rise (RSLR). Some of the oldest tide gauges have records spanning 150–200+ years [e.g. Key West, USA (Maul and Martin, 1993); Brest, France; Świnoujście, Poland; New York, USA; and San Francisco, USA (Woodworth et al., 2011); and Boston, USA (Talke et al., 2018)]. Tide-gauge data have played a central role in calculations of global sea-level rise (e.g. Gornitz et al., 1982) and they continue to do so today (e.g. Church and White, 2011; Church et al., 2013; Hay et al., 2015).

Tide-gauge data are also heavily relied upon to evaluate the vulnerability of low-elevation coastal zones (LECZs) (e.g. Syvitski et al., 2009; Nicholls and Cazenave, 2010; Kopp et al., 2014; Pfeffer and Allemand, 2016). LECZs include large deltas and coastal

plains that often have accumulated thick packages (tens of meters or more) of highly compressible Holocene strata and are the home to some of the world's largest population centers (e.g. Tokyo, Shanghai, Bangkok, Manila) that are increasingly at risk due to RSLR. At the regional level, tide-gauge data have been used to study a variety of spatially variable processes. For example, in coastal Louisiana, the largest LECZ in the United States, tide-gauge data have been used to measure land subsidence (Swanson and Thurlow, 1973), the acceleration of RSLR (Nummedal, 1983), multi-decadal rates of subsidence and RSLR (Penland and Ramsey, 1990), and the impact of fluid extraction on RSLR (Kolker et al., 2011).

The Permanent Service for Mean Sea Level (PSMSL; <http://www.psmsl.org>; Holgate et al., 2013) maintains records for nearly 2000 tide gauges globally, including five in coastal Louisiana: Eugene Island (data from 1939-1974), Grand Isle (1947-present), South Pass (1980-1999), Shell Beach (2008-present) and New Canal Station (2006-present). In many parts of the world, however, tide gauges with long, continuous records are few and far between. As a result, many studies of RSLR rely on tide-gauge records that are too short (longer than 50 years is preferable but at least 30 years is necessary to filter out natural variability due to phenomena such as storms, El Niño-Southern Oscillation cycles, changes in the orbital declination of the moon, shifts in ocean currents, and atmospheric pressure variability; Pugh, 1987; Douglas, 1991; Shennan and Woodworth, 1992), are from inappropriate locations (e.g. outside of the area being studied), or both. For example, of the 32 tide gauges used by Syvitski et al. (2009), 21 were located outside the delta of interest, 11 had records of <30 years, and 8 had both

shortcomings. Furthermore, subsidence rates are highly spatially variable, often increasing or decreasing 2- to 4-fold within short distances (a few km or less) as a result of subsurface fluid withdrawal and differential compaction, among other factors (e.g. Teatini et al., 2005; Törnqvist et al., 2008; Minderhoud et al., 2017; Koster et al., 2018; also see the review by Higgins, 2016). As a result, tide gauges provide limited information on subsidence rates beyond the instrument's immediate surroundings. Even if a tide gauge has a sufficiently long record and is appropriately located, it is critical to determine what processes the tide gauge is measuring, and what it is not measuring. In LECZs, this is commonly not straightforward.

Tide gauges measure RSLR with respect to a nearby set of benchmarks. Leveling campaigns are conducted regularly [for example, at least once every six months for National Oceanic and Atmospheric Administration (NOAA) tide gauges; NOAA, 2013] to account for any changes in the elevation of the tide gauge with respect to these reference points. Tide gauges are typically leveled using a benchmark designated as the primary benchmark; secondary benchmarks are used to assess the stability of the primary benchmark (NOAA, 2013).

Figure 2.1 shows a schematic of tide gauges and associated benchmarks in three contrasting environments. Along rocky coastlines, benchmarks are typically anchored directly onto bedrock that is exposed at the surface (Figure 2.1a). A tide gauge in such a setting therefore measures RSLR with respect to the land surface. In contrast, benchmarks in LECZs are typically anchored at depth. In thin LECZs, which are defined herein as those with unconsolidated sediment packages <20 m thick, benchmark

foundations typically penetrate the surficial layer of unconsolidated (usually Holocene) sediment and are anchored in the underlying consolidated (usually Pleistocene) strata (Figure 2.1b). In thick LECZs, defined as possessing unconsolidated sediment packages that are >20 m thick, benchmark foundations are generally not sufficiently deep to reach the consolidated strata and are anchored within the unconsolidated sediment (Figure 2.1c).

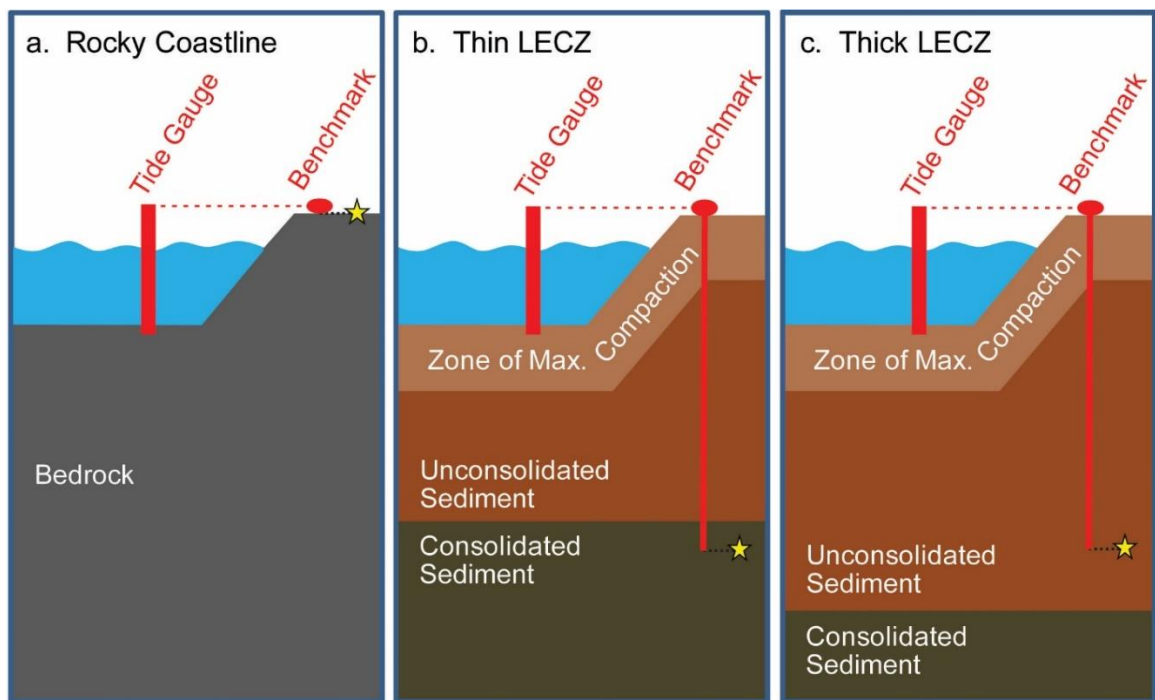


Figure 2.1. Schematic of a tide gauge and associated benchmark on a rocky coastline (a), a thin LECZ (b), and a thick LECZ (c). In all three environments, the tide gauge measures RSLR with respect to the base of the benchmark foundation, which is indicated by a star in each panel.

Regardless of the environment, all tide gauges measure changes in water surface elevation with respect to the foundation depth of their associated benchmarks. As a result, tide gauges with benchmarks anchored at depth do not account for processes occurring in the shallow subsurface, above the benchmark foundation (Cahoon, 2015). For the

purposes of this study, we define the subsidence that occurs above a benchmark's foundation as "shallow subsidence" (*sensu* Cahoon et al., 1995). Subsidence below a benchmark's foundation is termed "deep subsidence". In coastal Louisiana, at least 60% of subsidence occurs in the shallowest 5-10 meters (Jankowski et al., 2017). Tide gauges with benchmarks anchored at depth do not record this key component of RSLR (Cahoon, 2015). This issue was also recognized by Jankowski et al. (2017) and Nienhuis et al. (2017), but neither study elaborated on this problem. Here, we present a detailed assessment of benchmark information associated with tide gauges, followed by a discussion of its implications as well as methods to remedy this issue.

In order to better understand the contribution of vertical ground motion to RSLR, tide-gauge data are often used in conjunction with Global Navigation Satellite System (GNSS) data (e.g. Mazzotti et al., 2009; Wöppelmann et al., 2009; Wöppelmann and Marcos, 2016; see also the Intergovernmental Oceanographic Commission manuals on sea-level measurement and interpretation, available at http://www.psmsl.org/train_and_info/training/manuals/). In LECZs, GNSS stations are typically mounted on existing buildings or attached to rods that are driven to refusal (i.e. the depth at which friction prevents deeper penetration; see International GNSS Service station information at <http://www.igs.org/network> and National Geodetic Survey station information at <https://www.ngs.noaa.gov/CORS/>) and record the deep subsidence that occurs beneath their foundations. Similar to tide gauges, GNSS stations are nearly always anchored at depth and thus face many of the same concerns: they do not record shallow subsidence that occurs in the strata above the depth of their foundations.

Accurate measurements of RSLR are vital to predict the sustainability of world deltas and for communities in LECZs to adapt to their changing coastlines. In this study, we investigate the nature of tide gauge benchmarks and GNSS station foundations in coastal Louisiana and assess the implications for measurements of RSLR and subsidence in LECZs worldwide. Re-analysis of time series from tide gauges and GNSS stations is not the purpose of our study. Instead, we present an alternative approach to measuring RSLR in LECZs where shallow subsidence is determined using the rod surface-elevation table–marker horizon method [RSET-MH; see Webb et al. (2013) and Cahoon (2015) for detailed descriptions of this method] and deep subsidence is determined using GNSS data. Using the Mississippi Delta (a thick LECZ) and the Chenier Plain (a thin LECZ) in coastal Louisiana as the primary study areas, we determine benchmark foundation depths and the type of strata in which the foundations are anchored. This allows us to determine which subsidence processes are measured by tide gauges and GNSS stations and to evaluate their usefulness as recorders of RSLR. We then place our findings in the context of LECZs worldwide. Our results suggest that tide gauges (and existing analyses of tide-gauge data) in these environments may underestimate rates of RSLR as observed at the land surface, and as a result, many LECZs may be at higher risk of submergence than previously recognized.

2. DATA AND METHODS

Relative sea level and subsidence data are abundant in the Mississippi Delta and Chenier Plain, making coastal Louisiana an excellent target to assess methods of measuring RSLR. Records for at least 131 operational or previously operational tide

gauges in this region are maintained by NOAA (<https://tidesandcurrents.noaa.gov>), the U.S. Army Corps of Engineers (USACE; <http://www.rivergages.com> and Veatch, 2017), and the U.S. Geological Survey (USGS; <http://nwis.waterdata.usgs.gov>). Although 37 of these tide gauges have records spanning more than 30 years, many of their records are incomplete and have large data gaps. Many other tide gauges in coastal Louisiana have short records; nearly half have time series <10 years and a quarter are <2 years long (see Table A2.1 for information on all 131 tide gauges).

By means of exhaustive record combing of NOAA, USACE, and USGS archives, benchmark foundation depths were determined for tide gauges located in the Holocene landscape of the Mississippi Delta and Chenier Plain. Foundation depths were then compared to the local elevation of the Pleistocene surface (with respect to the North American Vertical Datum of 1988, NAVD 88; Heinrich et al., 2015). Because the land surface elevations at the tide gauge locations are close to sea level, the elevation of the Pleistocene surface is essentially equivalent to its depth beneath the land surface. When a tide gauge is associated with multiple benchmarks, the benchmark with the deepest known foundation was used for this analysis. For comparison, the analysis was repeated using primary benchmarks only.

A similar approach was taken to determine foundation depths of GNSS stations. GNSS station information was compiled from Dokka et al. (2006) and Karegar et al. (2015). Of the 45 GNSS stations used for analysis by one or both studies, 17 are located in the Holocene landscape of coastal Louisiana. GNSS station foundation depths were

compared to the local depth of the Pleistocene surface, similar to what was done for the tide gauges.

3. RESULTS

The 131 tide gauges in coastal Louisiana were examined for benchmark information (Table A2.1, Figure 2.2). Benchmark foundation depths are available for only 35 tide gauges (Table 2.1), including 31 maintained by NOAA and 4 maintained by USACE (see Table A2.1 for information on all 131 tide gauges). Each of these NOAA tide gauges is associated with 3 to 11 benchmarks (mean = 6 benchmarks), 77% of which have known foundation depths. The total number of associated benchmarks is unknown for the USACE tide gauges. Benchmarks with known foundation depths are typically mounted on steel rods driven to refusal. Benchmarks with unknown foundation depths are typically mounted on concrete structures of a variety of types (e.g. building foundations, bridge abutments, and seawalls). These concrete structures are likely to have foundations that extend into the subsurface, but specific construction details are unknown. It is important to note that an unknown foundation depth should not be interpreted as a foundation depth of zero. The remaining 96 tide gauges (73% of the total) have no available benchmark foundation information.

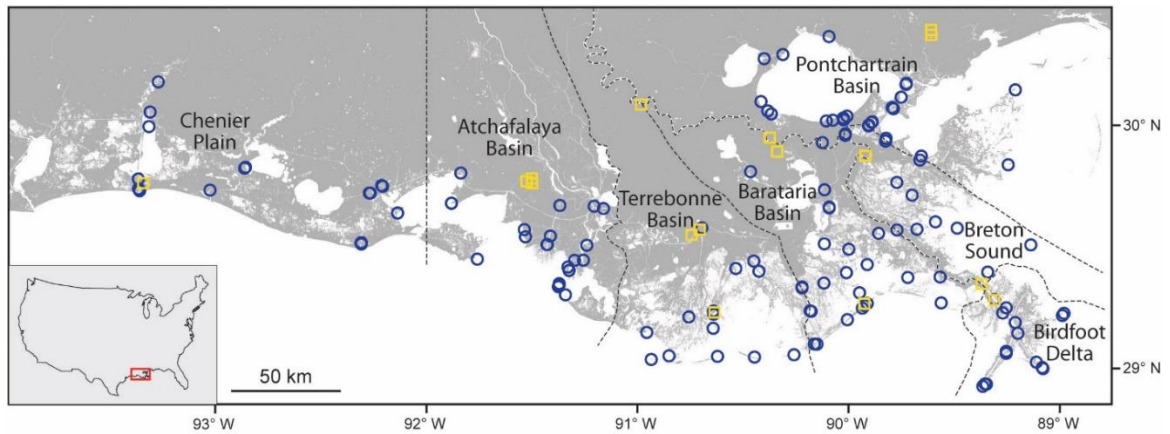


Figure 2.2. Location of tide gauges (circles, $n = 131$) and GNSS stations (squares, $n = 17$) in the Holocene landscape of coastal Louisiana. Dashed lines delineate geographic areas discussed in the text.

For tide gauges with available benchmark information, benchmark foundation depths range from 0.9 to 35.1 m, with a mean of 21.0 ± 5.4 m and a median of 20.7 m. Deepest known benchmarks are anchored an average of 21.5 ± 7.4 m below the ground surface, with a median depth of 23.2 m. Comparing this mean to the mean foundation depth of primary benchmarks (21.4 ± 3.9 m, $n = 23$), we find that there is no meaningful difference. Note that for 8 of these 23 tide gauges (35%), the primary benchmark is also the benchmark with the deepest known foundation. The mean foundation depth for the shallowest known benchmarks is 17.3 ± 7.0 m.

When a tide gauge is associated with multiple benchmarks, the benchmark with the deepest known foundation was used for this analysis. Figure 2.3 shows the location of tide gauges in coastal Louisiana (circles) and the foundation depth of their associated benchmarks relative to the local depth to the Pleistocene surface. The depth to the Pleistocene surface from the land surface at tide gauge locations ranges from 5 to 142 m, with a mean of 47 ± 34 m and a median of 44 m (Figure 2.4). Thus, benchmark

foundations are anchored an average of 26 m above the Pleistocene surface. Only 11 of the 35 tide gauges (31%) have benchmarks anchored in Pleistocene strata; the remaining 24 tide gauges (69%) have benchmarks anchored in Holocene strata.

Of the 17 GNSS stations in coastal Louisiana, 10 (59%) have known foundation depths (Table 2.2, Figure 2.3). Information for all 17 GNSS stations in coastal Louisiana is available in Table A2.2. Foundation depths of the 10 GNSS stations range from 1 to 36.5 m, with a mean of 14.3 ± 11.9 m and a median of 14.9 m (Table 2.2). Note that for two GNSS stations only minimum foundation depths are available; these minimum values are used in the analysis in order to produce conservative results. At GNSS station locations, the depth to the Pleistocene surface ranges from 10 to 78 m, with a mean of 39 ± 20 m and a median of 35 m (Figure 2.4). Thus, GNSS station foundations are anchored an average of 25 m above the Pleistocene surface. Only one of the 10 GNSS stations (10%) is anchored in Pleistocene strata, whereas the remaining 9 GNSS stations (90%) are anchored in Holocene strata. Figure 2.3 shows the location of GNSS stations in coastal Louisiana (squares) and their foundation depth relative to the local depth to the Pleistocene surface.

Table 2.1. Tide gauges in the Holocene landscape of coastal Louisiana with known foundation information ($n = 35$).

Tide gauge name	Agency	Latitude	Longitude	Maximum benchmark foundation depth (m)	Depth to Pleistocene surface (m)	Benchmark foundation height above Pleistocene surface (m)
Amerada Pass	NOAA	29.4500	-91.3383	27.4	21	Set in Pleistocene
Barataria Waterway	USACE	29.6694	-90.1106	7.4	36	29
Bay Gardene	NOAA	29.5983	-89.6183	23.2	43	20
Bay Rambo	NOAA	29.3617	-90.1400	24.4	54	30
Bayou Petit Caillou	USACE	29.2543	-90.6635	24.4	57	33

Bayou St. Denis	NOAA	29.4967	-90.0250	23.2	44	21
Billet Bay	NOAA	29.3717	-89.7517	21.9	52	30
Breton Island	NOAA	29.4933	-89.1733	16.8	70	53
Calcasieu Pass	NOAA	29.7683	-93.3433	25	18	Set in Pleistocene
Caminada Pass	NOAA	29.2100	-90.0400	21.9	55	33
Chef Menteur Pass	NOAA	30.0650	-89.8000	35.1	13	Set in Pleistocene
Comfort Island	NOAA	29.8233	-89.2700	16.8	38	21
Cypremort Point	NOAA	29.7133	-91.8800	19.4	10	Set in Pleistocene
East Bay	NOAA	29.0533	-89.3050	14.6	106	91
East Timbalier Island	NOAA	29.0767	-90.2850	28.8	46	17
Freshwater Canal Locks	NOAA	29.5517	-92.3050	17.1	15	Set in Pleistocene
Grand Isle	NOAA	29.2633	-89.9567	19.8	57	37
Grand Pass	NOAA	30.1267	-89.2217	23.2	15	Set in Pleistocene
Greens Ditch	NOAA	30.1117	-89.7600	21.9	8	Set in Pleistocene
Hackberry Bay	NOAA	29.4017	-90.0383	30.5	52	22
Lafitte	NOAA	29.6667	-90.1117	30.5	37	7
Lake Judge Perez	NOAA	29.5583	-89.8833	24.4	39	15
Leeville	NOAA	29.2483	-90.2117	28	57	29
Martello Castle	NOAA	29.9450	-89.8350	19.51	19	Set in Pleistocene
Mendicant Island	NOAA	29.3183	-89.9800	24.4	55	31
Mermentau River	USACE	29.7704	-93.0135	1.5	6	5
North Pass	NOAA	29.2050	-89.0367	15.2	142	127
Pass Manchac	NOAA	30.2967	-90.3117	20.7	15	Set in Pleistocene
Pelican Island	NOAA	29.2667	-89.5983	21.9	64	42
Pilottown	NOAA	29.1783	-89.2583	32	88	56
Port Eads	USACE	29.0147	-89.1658	0.9	128	127
Shell Beach	NOAA	29.8683	-89.6733	27.4	27	Set in Pleistocene
Southwest Pass	NOAA	28.9250	-89.4183	24.4	109	85
St. Mary's Point	NOAA	29.4317	-89.9383	24.4	50	26
Weeks Bay	NOAA	29.8367	-91.8367	14.3	5	Set in Pleistocene

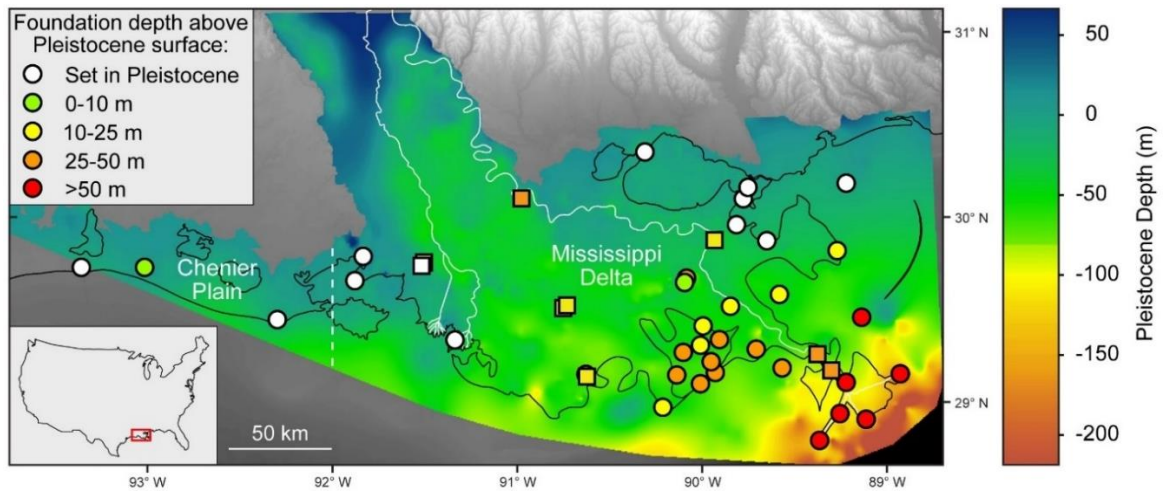


Figure 2.3. Elevation of the Pleistocene surface in coastal Louisiana (with respect to NAVD 88), which approximates the depth of the Pleistocene surface beneath the land surface given land surface elevations close to mean sea level. Circles and squares indicate tide gauge and GNSS station locations, respectively, and are color coded according to foundation height above the Pleistocene surface. Note that two GNSS stations (ENG1 and ENG2, see Table 2.2) have the same coordinates (and the same foundation depth) and plot on top of one another. The dashed white line, located at longitude 92° W, divides the Mississippi Delta from the Chenier Plain. Solid white lines show the Mississippi and Atchafalaya Rivers. Black lines indicate shorelines. Pleistocene depth information is from Heinrich et al. (2015).

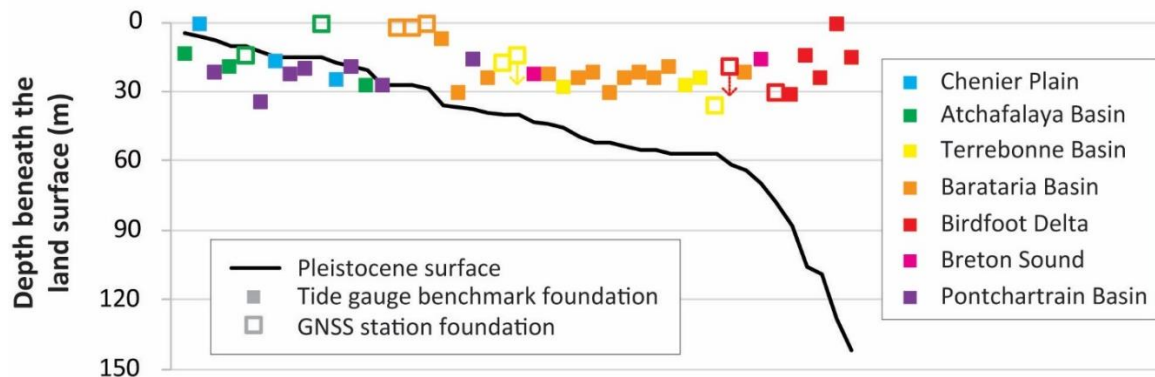


Figure 2.4. Schematic dip-oriented cross section comparing the depth of tide gauge benchmarks and GNSS station foundations to the local depth to the Pleistocene surface. Sites are arranged by increasing depth of the Pleistocene surface. Note that two GNSS stations have minimum foundation depths (see Table 2.2), indicated here by small, downward-pointing arrows. See Figure 2.2 for the location of geographic areas.

Table 2.2. GNSS stations in the Holocene landscape of coastal Louisiana with known foundation information ($n = 10$).

GNSS station code	Latitude	Longitude	Foundation depth (m)	Depth to Pleistocene surface (m)	Foundation height above Pleistocene surface (m)	Data source
AWES	30.10	-90.98	1	29	28	Karegar et al. (2015)
BVHS	29.34	-89.41	>20	62	<42	Dokka et al. (2006); Karegar et al. (2015)
ENG1	29.88	-89.94	~3	27	~24	Karegar et al. (2015)
ENG2	29.88	-89.94	~3	27	~24	Dokka et al. (2006)
FRAN	29.80	-91.53	14.7	10	Set in Pleistocene	Dokka et al. (2006)
FSHS	29.81	-91.50	1	15	14	Karegar et al. (2015)
HOMA	29.57	-90.76	18.3	40	22	Dokka et al. (2006)
HOUM	29.59	-90.72	>15	40	<25	Dokka et al. (2006); Karegar et al. (2015)
LMCN	29.25	-90.66	36.5	57	21	Dokka et al. (2006); Karegar et al. (2015)
VENI	29.28	-89.36	30.5	78	48	Dokka et al. (2006)

4. DISCUSSION

4.1. Implications for the interpretation of tide gauge and GNSS records

In coastal Louisiana, foundation information for tide gauge benchmarks and GNSS stations is often not available, essentially precluding the interpretation of resulting time series in terms of rates of RSLR. Although many of the tide gauges listed in Table 2.1 are not useful for RSLR analyses due to their short records, all of the benchmarks used for the present analysis are currently published and considered stable. Furthermore, some of the tide gauges that currently have short time series could become important in the future as their records become longer (e.g. Shell Beach). Because all tide gauge

benchmarks with known foundation information are anchored at depth rather than at ground level, and most (91%) are anchored well below the land surface (>10 m), their interpretation is far from straightforward. Tide gauges with benchmarks anchored at depth measure deep subsidence plus the component of RSLR associated with changes in real (geocentric) ocean level, but do not capture shallow subsidence, often a dominant element of total subsidence in this region. Similarly, all GNSS stations are anchored at depth (60% are anchored >10 m deep) and also do not record shallow subsidence. Thus, tide gauges and GNSS stations in coastal Louisiana systematically underestimate the rates of local RSLR and subsidence, respectively.

Many tide gauges in coastal Louisiana have benchmarks that are mounted on existing concrete structures. The primary benchmark for the Grand Isle tide gauge, for example, is mounted on a seawall. Similar to tide gauges that measure RSLR with respect to a benchmark mounted on a steel rod driven to depth, the Grand Isle tide gauge produces a time series of RSLR with respect to the foundation of the concrete structure into which its primary benchmark is mounted. Although we were unable to acquire construction details for the seawall at Grand Isle, it is highly unlikely that it is simply resting on the land surface. We expect that the seawall foundation extends at least several meters into the subsurface in order to provide stability and protection to the adjacent Grand Isle Coast Guard station. Five other tide gauges also have primary benchmarks anchored on concrete structures: Caminada Pass, East Bay, Freshwater Canal Locks, Lafitte, and Martello Castle. Although all of these primary benchmarks are likely anchored at some depth below the surface, it is conceivable that their foundations are

shallower than that of the deepest benchmarks (e.g. 19.8 m at Grand Isle). This may reduce the underestimation of the rate of RSLR measured by these tide gauges.

On the other hand, the RSET-MH data presented by Jankowski et al. (2017) suggest that shallow subsidence occurs dominantly in the uppermost 5 m in coastal Louisiana. Using data from 274 monitoring stations, Jankowski et al. (2017) calculated a mean shallow subsidence rate of $6.8 \pm 7.9 \text{ mm yr}^{-1}$. Limiting this analysis to stations where the instrument is anchored in Pleistocene strata and the overlying (Holocene) strata are $<5 \text{ m}$ thick, we find a mean shallow subsidence rate of $6.4 \pm 5.4 \text{ mm yr}^{-1}$ ($n = 55$). The similarity between these two numbers suggests that shallow subsidence is concentrated in the uppermost 5 m in this region. The implication would be that tide gauges with benchmarks anchored as little as 5 m below the surface would still not capture shallow subsidence and thus underestimate the rate of RSLR.

If a tide gauge benchmark is anchored in Pleistocene deposits, deep subsidence consists solely of subsidence within the Pleistocene and underlying strata (Figure 2.1b). This scenario is common in LECZs with a relatively thin Holocene sediment package, such as the Chenier Plain. In the Chenier Plain, the Pleistocene surface subsides at a rate of $\sim 1 \text{ mm yr}^{-1}$, yet the wetland surface is subsiding notably faster, at a rate of 7.5 mm yr^{-1} on average (Jankowski et al., 2017). The remaining 6.5 mm yr^{-1} of shallow subsidence occurs above the depth of local benchmark foundations and is typically not captured by tide gauges in this region.

In the case of a benchmark that is anchored in Holocene strata, deep subsidence also includes subsidence of the part of the Holocene sediment column that underlies the

benchmark foundation. This scenario (Figure 2.1c) is common in LECZs with thick sediment packages such as the Mississippi Delta, and further complicates the interpretation of tide-gauge data. Compaction of deeper Holocene strata may result in an increase in the measured rate of RSLR when compared to tide gauges with benchmarks anchored in Pleistocene strata. However, tide gauges with benchmarks anchored in Holocene strata still record rates of RSLR that are considerably lower than what is seen at the land surface in the Mississippi Delta ($13 \pm 9 \text{ mm yr}^{-1}$; Jankowski et al., 2017). For example, Kolker et al. (2011) and Karegar et al. (2015) calculated modern RSLR rates from tide-gauge data in the Mississippi Delta of $\sim 3 \text{ mm yr}^{-1}$ (after adding the long-term rate of RSLR measured at Pensacola, Florida) and at least $\sim 7 \text{ mm yr}^{-1}$, respectively.

Around the world, many LECZs have sediment packages that exceed 20 m in thickness, and some are as thick as 100 m or more (Table 2.3). Benchmarks in these areas are likely constructed in a broadly similar fashion to those in coastal Louisiana: either attached to rods driven to refusal or mounted on existing structures with non-negligible foundation depths. Tide-gauge benchmarks in The Netherlands, for example, are anchored 5-25 m deep (R. Hoogland, personal communication, 2018) and generally reach the Pleistocene basement except in areas where the Holocene sediment thickness is greatest (Table 2.4). Thus, conditions in The Netherlands are roughly comparable to those in the Chenier Plain of coastal Louisiana (and likely other “thin” LECZs): tide gauges do not capture the shallow subsidence component of RSLR, but because benchmarks are generally anchored in a relatively stable substrate they are easier to

interpret than many of the tide gauges in the Mississippi Delta (and likely other “thick” LECZs) where benchmarks are essentially “floating” in the Holocene succession.

In LECZs globally, tide gauges likely underestimate the local rate of RSLR. A lack of reliable RSLR data will be increasingly problematic in several large deltas that are home to major population centers (e.g. Ganges-Brahmaputra, Song Hong, Yangtze, Mekong, Nile) and are experiencing rapid subsidence (Alam, 1996; Mathers and Zalasiewicz, 1999; Shi et al., 2008; Erban et al., 2014; Gebremichael et al., 2018). In these areas and in LECZs globally, people and infrastructure may therefore be even more vulnerable to flooding than previously recognized (e.g. Syvitski et al., 2009; Tessler et al., 2015).

Two studies that considered delta vulnerability on a global scale (Ericson et al., 2006; Tessler et al., 2015) are noteworthy because they did not depend on tide-gauge data. These studies determined RSLR by adding the historic rate of real (geocentric) sea-level rise to natural and anthropogenic subsidence data (Ericson et al., 2006) or by combining sea-level rise from satellite altimetry with subsidence estimates associated with fluid extraction (Tessler et al., 2015). While these approaches bypass the problems with tide gauges discussed above, they are also inherently limited by the need to characterize individual deltas by single metrics, by relying on measurements of global rather than local sea-level rise, and/or by not considering all major subsidence processes (notably shallow compaction). In the next section, we build on the recent study by Jankowski et al. (2017) to offer an alternative approach to measure RSLR in LECZs.

Table 2.3. Holocene sediment thicknesses of LECZs around the world, measured close to the shoreline where coastal strata tend to be the thickest.

Low-elevation coastal zone	Maximum	LECZ	Reference
	thickness (m)	type	
Chenier Plain, Miranda, New Zealand	3-5	thin	Woodroffe et al. (1983)
Chenier Plain, SW Louisiana, USA	5-10	thin	Heinrich et al. (2015)
Venice Lagoon, Italy	10-15	thin	Zecchin et al. (2009)
Chao Phraya Delta, Thailand	10-15	thin	Tanabe et al. (2003a)
Vistula Delta, Poland	10-20	thin	Mojski (1995)
Rhine-Meuse Delta, The Netherlands	20-25	thick	Hijma et al. (2009)
Huanghe Delta (modern), China	20-25	thick	Xue (1993); Yi et al. (2003)
Po Delta, Italy	20-25	thick	Amorosi et al. (2017)
Tokyo Lowland, Japan	20-60	thick	Tanabe et al. (2015)
Mekong Delta, Vietnam	25-40	thick	Ta et al. (2002); Tanabe et al. (2003b)
Nobi Plain, Japan	30-40	thick	Hori et al. (2011)
Shatt al-Arab Delta, Iraq	30-40	thick	Larsen (1975)
Nile Delta, Egypt	30-50	thick	Stanley and Warne (1993)
Song Hong Delta, Vietnam	35-40	thick	Funabiki et al. (2007)
Fly Delta, Papua New Guinea	35-45	thick	Harris et al. (1993)
Ganges-Brahmaputra Delta, Bangladesh	50-100	thick	Goodbred and Kuehl (2000)
Mississippi Delta, SE Louisiana, USA	50-100	thick	Heinrich et al. (2015)
Yangtze Delta, China	60-90	thick	Li et al. (2000)
Indus Delta, Pakistan	110-120	thick	Clift et al. (2010)

Table 2.4. Benchmark foundation depths and local depth to the Pleistocene surface for tide gauges in The Netherlands. Benchmark depths from R. Hoogland (personal communication, 2018). Pleistocene surface depths are from Vos et al. (2011).

Tide gauge name	Agency	Latitude	Longitude	Benchmark foundation depth (m)	Depth to Pleistocene surface (m)	Benchmark foundation height above Pleistocene surface (m)
Vlissingen	Rijkswaterstaat	51.4422	3.5961	17.6	4-6	Set in Pleistocene
Hoek van Holland	Rijkswaterstaat	51.9775	4.1200	14	20-22	6-8
IJmuiden	Rijkswaterstaat	52.4622	4.5547	13	18-20	5-7
Den Helder	Rijkswaterstaat	52.9644	4.7450	5-25	2-4	Set in Pleistocene
Harlingen	Rijkswaterstaat	53.1756	5.4094	5-25	4-6	Likely set in Pleistocene
Delfzijl	Rijkswaterstaat	53.3264	6.9331	20	6-8	Set in Pleistocene

4.2. An alternative method for measuring present-day rates of relative sea-level rise

In order to accurately measure present-day RSLR in LECZs, we propose an alternative approach that combines measurements of shallow subsidence from RSET-MHs with measurements of deep subsidence and the oceanic component of sea-level rise from GNSS and satellite altimetry data, respectively (Figure 2.5). This approach results in RSLR measurements expressed with respect to the land surface and eliminates the need for tide-gauge data. Nevertheless, we stress that best scientific practices will make use of all available data and compare the results of various measurement techniques. Furthermore, tide gauges remain critical for measuring many other processes, including tides (the original purpose of tide gauges) and event-scale phenomena such as storm surge, and remain invaluable in this regard.

In principle, both GNSS stations and tide gauges could be used to measure deep subsidence and these data could then be combined with measurements of shallow subsidence (plus geocentric sea-level rise, in the case of GNSS data) to calculate RSLR. However, tide gauges must have sufficiently long time series (at least 30 years) and known foundation depths to be useful in this context. In coastal Louisiana, the number of tide gauges that meet these criteria ($n = 5$) are fewer than the number of GNSS stations with known foundation depths ($n = 10$). Additionally, concerted efforts are currently underway to address the complexities regarding GNSS monumentation. At a newly constructed subsidence superstation located in the lower Mississippi Delta, for example, three GNSS instruments are anchored at different depths in order to obtain a depth-integrated subsidence profile (Allison et al., 2016). Although this type of analysis is new,

it can greatly improve our understanding of subsidence in LECZs in the future.

Furthermore, GNSS data are less susceptible to short-term environmental conditions (i.e. wind speed and direction, tides, atmospheric pressure changes) than are tide gauge data.

Thus, GNSS is the preferred method for measuring deep subsidence.

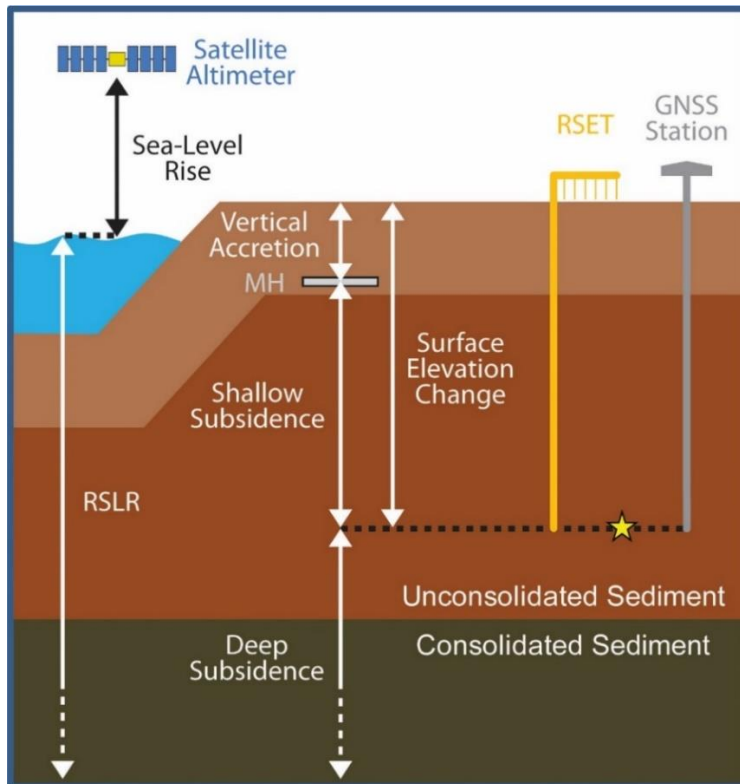


Figure 2.5. Schematic of combined instrumentation that includes a RSET-MH, which measures shallow subsidence, and a GNSS station, which measures deep subsidence. To measure shallow subsidence using a RSET-MH, surface elevation change is subtracted from vertical accretion (Cahoon, 2015). Surface elevation change is the change in height from a horizontal arm at a fixed elevation to the wetland surface, measured using vertical pins. Vertical accretion is the thickness of sediment that accumulates above a feldspar marker horizon. If constructed with similar foundation depths (as shown by the star), the RSET-MH and GNSS station collect data that are complementary and can be added together and combined with satellite altimetry data to calculate the rate of RSLR.

Although RSET-MHs, GNSS, and satellite altimetry all have unique limitations, technology is rapidly improving and reducing these shortcomings. Until recently, for example, satellite altimetry was ineffective in coastal areas (Cipollini et al., 2017).

However, the launch of the Surface Water and Ocean Topography (SWOT; <https://swot.jpl.nasa.gov/home.htm>) mission in 2021 is one of several efforts that are expected to significantly improve the quality of sea-surface records in the coastal zone and could therefore become an important element of the approach advocated here (Vignudelli et al., 2011). One remaining limitation of our proposed method of measuring RSLR is that RSET-MHs are only useful in wetland environments such as marshes (e.g. Day et al., 2011) and mangroves (e.g. Lovelock et al., 2015). However, space-based geodetic methods such as interferometric synthetic-aperture radar (InSAR) are effective at measuring subsidence rates (the sum of shallow and deep subsidence rates) in heavily human-modified delta environments (e.g. urban areas, agricultural land; Dixon et al., 2006; Jones et al., 2016; Da Lio et al., 2018), and thus can be complementary to RSET-MH datasets in this context. Care must be taken though to avoid reliance on permanent scatterers (e.g. buildings) with foundations at depth that may also not fully capture the shallow subsidence component. Ideally, RSET-MHs are installed with similar foundation depths as nearby GNSS stations in order to confirm that the two instruments are neither duplicating nor missing subsidence intervals. In coastal Louisiana, however, 33% of GNSS stations have no known foundation information, and this lack of information is likely a common phenomenon worldwide.

Currently, coastal Louisiana has nearly 350 RSET-MHs operated by the USGS as part of the Coastwide Reference Monitoring System (CRMS; <https://lacoast.gov/crms2>), which provide shallow subsidence data at high spatial resolution. Although data from a single RSET-MH are commonly too noisy to produce a reliable trend (Jankowski et al.,

2017), partly because most RSET-MHs were installed within the last decade and thus have time series that are mostly <10 years long, such a high density of RSET-MHs is not necessary to produce adequate estimates of shallow subsidence rates for a wider region. Using a Monte Carlo approach, we took random samples from subsets of the full RSET-MH dataset for coastal Louisiana ($n = 274$) to determine the smallest sample size that would still produce reasonable outcomes with an acceptable error. While determining the acceptable error is inherently somewhat arbitrary, the results show that in coastal Louisiana a minimum of 40 RSET-MHs would be needed in order to produce a mean shallow subsidence rate with a sufficiently narrow 95% confidence interval (4.54–9.18 mm yr⁻¹; Figure 2.6). In terms of density and given the size of coastal Louisiana (25,000–30,000 km²), we estimate that two RSET-MHs per 1000 km² would suffice. Although this density is slightly higher than strictly needed in coastal Louisiana, it is conceivable that higher densities may be necessary in smaller LECZs.

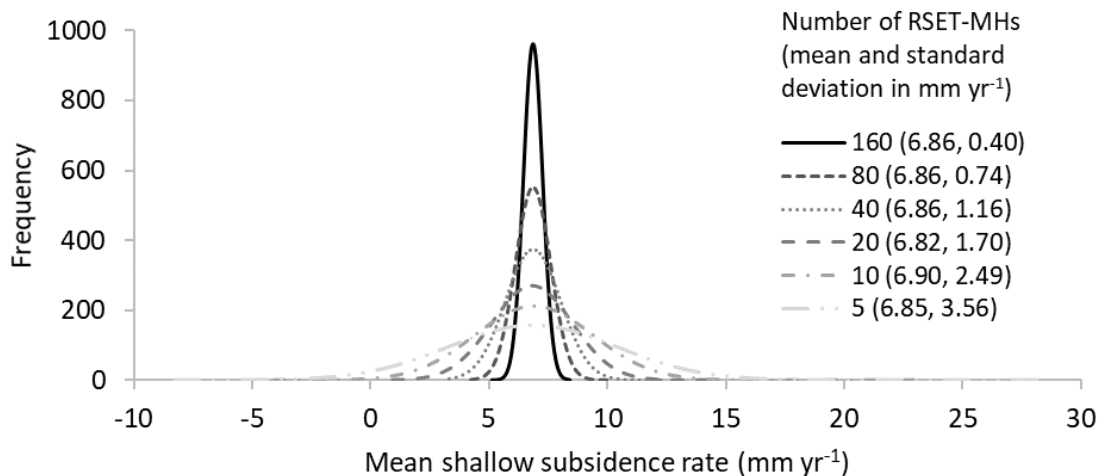


Figure 2.6. Probability density functions of the mean shallow subsidence rate for a given number of RSET-MHs, calculated using a Monte Carlo simulation and 10,000 randomizations per analysis.

In addition, averaging data from at least 40 RSET-MHs will encompass the high spatial variability commonly seen in shallow subsidence. In coastal Louisiana, spatial correlation in subsidence rates is largely limited to distances <5 km, and no correlation exists beyond 25 km (Nienhuis et al., 2017). As a result, the relevance of a single measurement of shallow subsidence is limited to the area immediately around the instrument. Around the world, tide gauges are generally spaced tens if not hundreds of kilometers apart. Even if tide gauges had benchmarks anchored at the land surface and were able to measure shallow subsidence, there simply are not enough tide gauges with records that are sufficiently long for RSLR analysis to capture the large spatial variability in shallow subsidence. In LECZs worldwide, our ability to predict local rates of RSLR will improve as more RSET-MHs are added to a growing global network. We therefore echo Webb et al. (2013) who first proposed this type of global RSET-MH network, arguing that the instruments are low-cost and produce highly valuable measurements of shallow subsidence.

5. CONCLUSIONS

In the Mississippi Delta and Chenier Plain of coastal Louisiana, tide gauge benchmarks and GNSS stations are anchored an average of 21.5 ± 7.4 m and $>14.3 \pm 11.9$ m below the land surface, respectively. By comparison, the local depth to the Pleistocene surface averages 47 ± 34 m at tide gauge locations and 39 ± 20 m at GNSS stations. Instruments located in the Chenier Plain, a thin LECZ with Holocene strata typically only 5-10 m thick, are generally anchored in consolidated Pleistocene strata. In

the Mississippi Delta, a LECZ where the Holocene sediment package is an order of magnitude thicker, tide gauge benchmarks and GNSS stations are typically anchored within unconsolidated Holocene strata and therefore produce time series that are very difficult to interpret. Instruments anchored at depth do not capture shallow subsidence, a major component of total subsidence in this area. As a result, tide gauges and GNSS stations in coastal Louisiana, and likely in LECZs worldwide, underestimate rates of RSLR and subsidence with respect to the land surface by a variable but unknown amount.

In order to accurately measure present-day RSLR in LECZs, we propose an alternative method which combines measurements of shallow subsidence from RSET-MHs with measurements of deep subsidence and the oceanic component of sea-level rise from GNSS stations and satellite altimetry, respectively. This approach produces rates of RSLR that are explicitly tied to the land surface and eliminates the need for tide-gauge data in this context. We find that for an area the size of coastal Louisiana, a minimum density of two RSET-MHs per 1000 km² is necessary in order to obtain robust shallow subsidence data. We support the call for a global network of RSET-MHs as first put forward by Webb et al. (2013) and recently echoed by Osland et al. (2017). Data from such a global network will help refine existing plans for coastal adaptation that presently may be inadequate to deal with potentially higher-than-anticipated rates of RSLR.

6. ACKNOWLEDGEMENTS

This work was supported by the U.S. National Science Foundation (EAR-1349311). We would like to thank Carl Swanson for writing the Python code to run the Monte Carlo analysis, William Veatch for locating benchmark information for USACE

tide gauges, and Rena Hoogland (Rijkswaterstaat, The Netherlands) and Marc Hijma (Deltares, The Netherlands) for providing Dutch benchmark data. We appreciate comments on the manuscript provided by Don Cahoon. Thoughtful reviews by Phil Woodworth and an anonymous referee led to considerable improvements.

CHAPTER 3: HYDRODYNAMIC CONTROLS ON SEDIMENT RETENTION IN AN EMERGING DIVERSION-FED DELTA

Molly E. Keogh, Alexander S. Kolker, Gregg A. Snedden, and Alisha A. Renfro

ABSTRACT

The morphodynamics of river-dominated deltas are largely controlled by the supply and retention of sediment within deltaic wetlands and the rate of relative sea-level rise. Yet, sediment budgets for deltas are often poorly constrained. In the Mississippi River Delta, a system rapidly losing land due to natural and anthropogenic causes, restoration efforts seek to build new land through the use of river diversions. At the Davis Pond Freshwater Diversion, a new crevasse splay has emerged since construction was completed in 2002. Here, we use beryllium-7 activity in sediment cores and USGS measurements of discharge and turbidity to calculate seasonal sediment input, deposition, and retention within the vegetated Davis Pond receiving basin. In winter/spring 2015, which included an experimental period of high discharge through the diversion, Davis Pond received 106,800 metric tons of sediment, 44% of which was retained within the basin. During this time, mean flow velocity was 0.21 m s^{-1} and mean turbidity was 56 formazin nephelometric units (FNU). In summer/fall 2015, the Davis Pond basin received

35,900 metric tons of sediment, 81% of which was retained. Mean flow velocity in summer/fall was 0.10 m s^{-1} and mean turbidity was 55 FNU. The increase in sediment retention from winter/spring 2015 to summer/fall 2015 may be due in part to the corresponding drop in water flow velocity, which allowed more sediment to settle out of suspension. Although high water discharge increases sediment input and deposition, increased turbulence associated with higher current velocity appears to increase sediment throughput and thereby decrease the sediment trapping efficiency. Sediment retention in Davis Pond is on the high end of the range seen in deltaic wetlands, perhaps due to the enclosed geometry of the receiving basin. Future diversion design and operation should target moderate water discharge and flow velocities in order to jointly maximize sediment deposition and retention and provide optimal conditions for delta growth.

1. INTRODUCTION

The morphodynamics of river-dominated deltas are largely controlled by relative sea-level rise and the supply and retention of sediment within deltaic wetlands. Over the last century, human engineering of river channels has greatly reduced the amount of sediment delivered to deltas (Stanley and Warne 1993, Syvitski et al. 2005, Yang et al. 2005, Blum and Roberts 2009, Meade and Moody 2010). Dams reduce downriver suspended sediment concentration and containment levees prevent overbank deposition. Yet, despite recent reductions in fluvial sediment supply to many coastlines around the world, some rivers still carry sufficient sediment to build new deltas at their mouths [e.g. Atchafalaya and Wax Lake deltas, Louisiana (Roberts et al. 2003, Rosen and Xu 2013, Carle et al. 2015); Río Sínú Delta, Colombia (Suarez 2004); Río Patía Delta, Colombia

(Restrepo and Kettner 2012)]. In these cases, reduced sediment supply may be mitigated by high rates of sediment retention within the delta complex.

Today, many low-lying river deltas starved of sediment input are threatened by subsidence, sea-level rise, and other natural and anthropogenic processes such as dredging (Turner 1997), subsurface fluid withdrawal (Kolker et al. 2011), sediment compaction (Törnqvist et al. 2008), hurricane and storm surge erosion (Barras 2006), and eustatic sea-level rise (Blum and Roberts 2009), which together may impair the sustainability of these landscapes. At the same time, deltas and other low-elevation coastal zones are home to over 625 million people globally (Neumann et al. 2015) and support numerous mega-cities (Syvitski and Saito 2007). In the Mississippi River Delta (MRD; Figure 3.1a), the combination of natural and anthropogenic processes has resulted in rapid land loss, with nearly 5,000 km² of land having converted to open water over the last 80 years (Couvillion et al. 2011). Built over the last ~7,500 years as distributary channel avulsions relocated sediment depocenters, the MRD is now largely in the transgressive phase of the delta cycle (Frazier 1967, Roberts 1997). Since the 1950s, sediment load in the Mississippi River has decreased by half (Blum and Roberts 2009, Meade and Moody 2010). Though growth and decay of individual delta lobes is a natural part of the delta cycle, the abovementioned anthropogenic impacts (dredging, subsurface fluid withdrawal, eustatic sea-level rise) have exacerbated land loss in the MRD, threatening coastal Louisiana's economy, infrastructure, and the overall sustainability of the delta (Turner 1997, Blum and Roberts 2009, Kolker et al. 2011).

Current restoration efforts in the MRD aim to maximize wetland building using the remaining sediment load in the river. Freshwater and sediment diversions play a central role in these endeavors (CPRA 2017). These diversions are strategic, gated structures through the river levee that are designed to mimic natural deltaic land-building processes by restoring the delivery of fresh water, sediment, and nutrients to the adjacent wetlands (Roberts et al. 2003, Snedden et al. 2007, Kim et al. 2009). Interestingly, river diversions are anthropogenic countermeasures intended to mitigate land loss caused in large part by other anthropogenic activities. Each diversion structure can be engineered to optimize a variety of physical and ecological parameters specific to its location and purpose, including water discharge, velocity, and stage as well as impacts to fisheries in the basin and navigation in the Mississippi River (Allison and Meselhe 2010, De Mutsert 2017, Peyronnin et al. 2017). When river water flows through a diversion, it leaves the engineered realm and typically enters a relatively natural wetland setting. As water spreads across the wetland, it slows and drops its suspended sediments. Over time, if sediment deposition exceeds that which is lost through erosion and relative sea-level rise, wetlands may expand laterally and gain elevation (Roberts 1997). The percent of sediment retained within a diversion receiving basin is critical in determining whether the wetlands expand or succumb to subsidence and sea-level rise. Indeed, a close analysis of Blum and Roberts (2009) indicates that large shifts in sediment retention rate can convert projections of land loss in the MRD to land gain, even under conditions of accelerated sea-level rise.

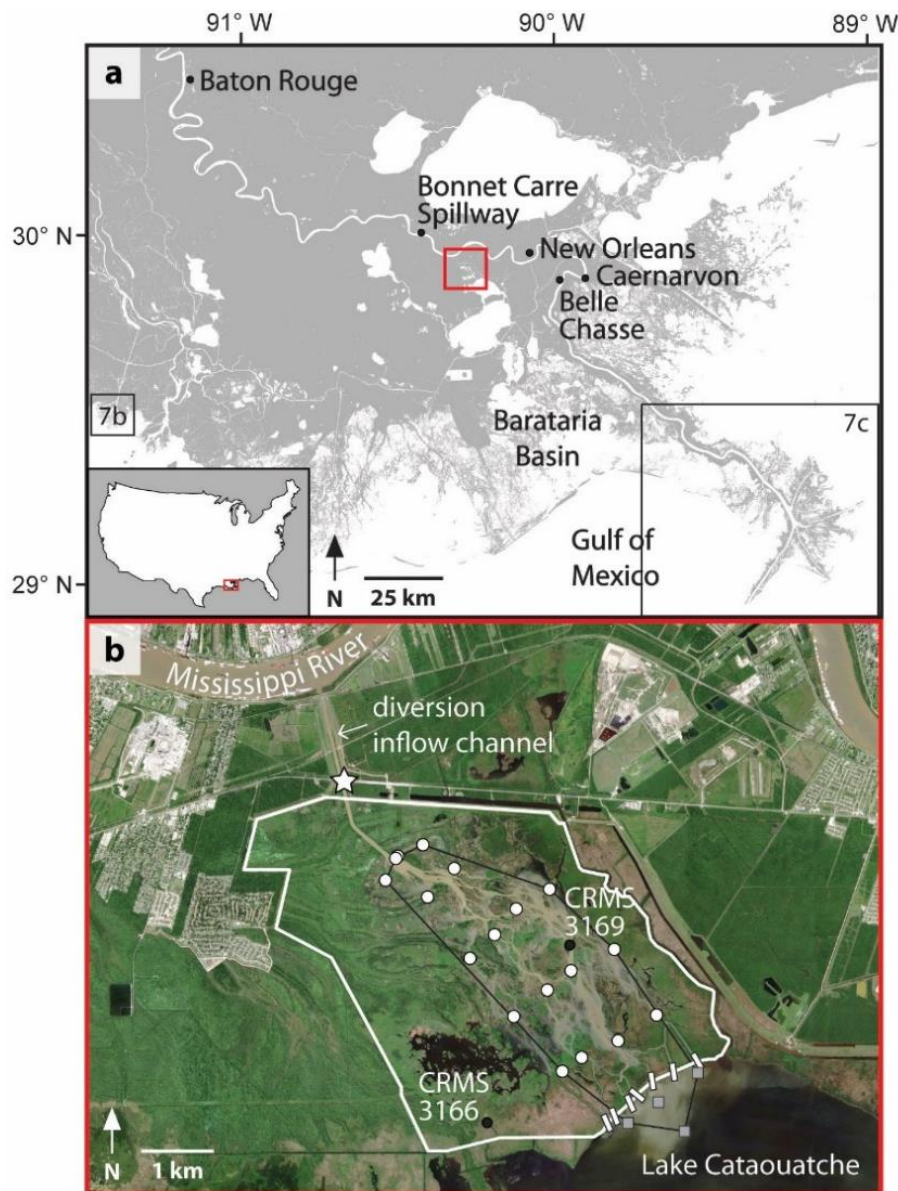


Figure 3.1. (a) The Mississippi River Delta, southeastern Louisiana, USA. The red box indicates Davis Pond Freshwater Diversion (shown in detail in b). The boxes indicate locations shown in detail in Figures 3.7b and c. (b) Satellite imagery of the Davis Pond area on April 6, 2016. The receiving basin is outlined in white; the coring area is outlined in black. Spring 2015 coring locations within the receiving basin are shown as white circles (note that two coring locations at the mouth of the diversion inflow channel are very close together and have symbols that largely overlap); grey squares indicate coring locations outside the receiving basin. White rectangles mark the 7 outflow channels that drain Davis Pond. The star indicates U.S. Geological Survey channel monitoring station 295501090190400 and black circles show the locations of two Coastwide Reference Monitoring System (CRMS) stations. Satellite imagery modified from Google Earth.

Many interrelated factors affect sediment retention within a wetland, including vegetation type and density (Gleason et al. 1979, Braskerud 2001, Adame et al. 2010), basin elevation gradient (Hook 2003), and water residence time (Kleiss 1996, Koskiaho 2003). The purpose of this study is to further quantify hydrodynamic controls on sediment retention in a developing delta. Specifically, we compare sediment input, deposition, and retention at high and low water discharge through a river diversion. We hypothesize that optimal sediment deposition is determined by a balance between sediment supply and retention that varies with water discharge. Whereas increasing discharge delivers more suspended sediment to a developing delta, decreasing flow velocity reduces sediment throughput and leads to a greater percent sediment retention. Here, sediment throughput is defined as sediment that passes into and immediately out of a basin without being deposited. This hypothesis is tested in the receiving basin of the Davis Pond Freshwater Diversion, a sheltered, low-gradient freshwater marsh in southeastern Louisiana (Figure 3.1b).

Our hypothesis implies that increasing water and sediment input to a deltaic wetland does not always lead to greater sediment deposition within the wetland. This is a novel hypothesis because previous discussions of river diversions have assumed that higher discharge is always better in terms of wetland building (e.g. Peyronnin et al. 2017). We suggest instead that there may be a tipping point along the discharge continuum, above which the increased water discharge no longer results in additional land building and increases the potential for detrimental ecosystem impacts. Diverting excess water may increase the inundation depth of wetlands and stress on vegetation (e.g.

Snedden et al. 2015), intensify the flood risk for local landowners and communities (e.g. McAlpin et al. 2008), and more drastically alter the basin's salinity regime and harm local fisheries (e.g. Reed et al. 2007). Although Peyronnin et al. (2017) suggest that the operation of diversions during winter months would limit damage to vegetation and fisheries, further research is needed on this topic.

The ideal operation regime for a river diversion maximizes sediment delivery and deposition while minimizing water delivery. The water discharge associated with an ideal operation regime is expected to vary between diversions based on location, maximum discharge potential, geometry, and other site-specific characteristics. Here, we present short-term sediment accumulation rates for high- and low-flow seasons and compare them to long-term retention rates measured in the MRD and other deltas. Our findings may enhance the efficacy of engineered river diversions as restoration tools (specifically the planned Mid-Barataria Sediment Diversion in the lower Mississippi River Delta) and help ensure that optimal hydrodynamic conditions are achieved for sustainable delta building.

2. STUDY AREA

Davis Pond Freshwater Diversion is located on the right descending bank of the Mississippi River, ~30 km upstream from New Orleans, Louisiana (Figure 3.1b). Davis Pond is a controlled diversion that redirects a variable amount of water from the river into a low-gradient receiving basin in upper Barataria Basin (Figure 3.2a). Mean discharge through the diversion was $\sim 36 \text{ m}^3 \text{ s}^{-1}$ over the study period (Nov. 2014 – Oct. 2015). Occasional periods of high discharge increase the flow up to a maximum of $\sim 300 \text{ m}^3 \text{ s}^{-1}$

and raise the water level in the receiving basin (Figure 3.2b). These high discharge events typically last a few weeks and are often timed to coincide with a springtime rising limb of the Mississippi River hydrograph (Figure 3.2c) when basin salinities are elevated.

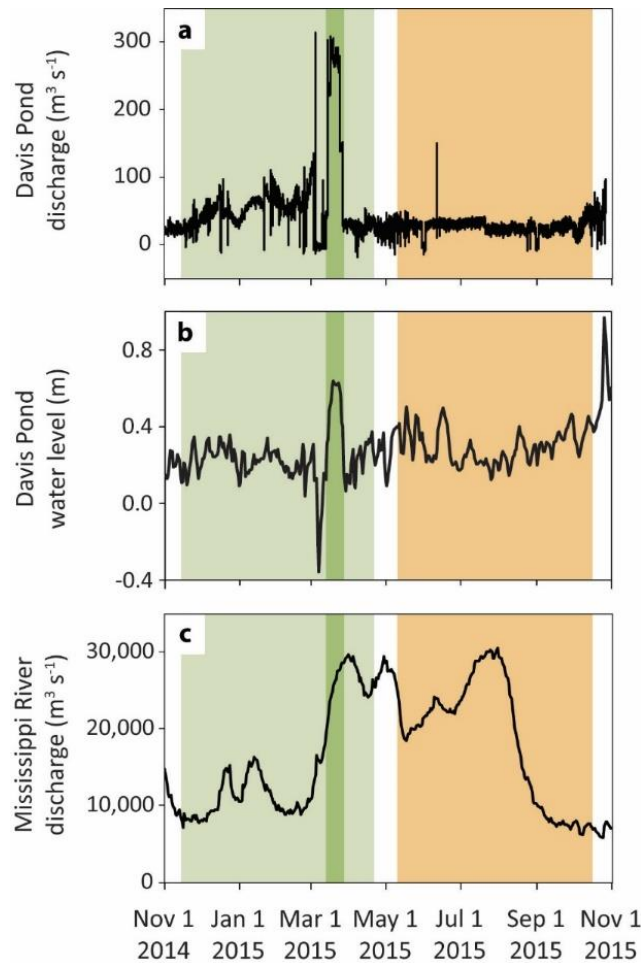


Figure 3.2. Discharge through the Davis Pond inflow channel (a), water level in the Davis Pond receiving basin (b), and Mississippi River discharge at Belle Chasse (c) from Nov. 1, 2014 to Oct. 31, 2015. The two 159-day seasons used for analysis are shaded: winter/spring is in green and summer/fall is in orange. The dark green bar in the winter/spring season marks the two-week experimental high discharge event in Davis Pond.

Subsidence in the MRD averages $\sim 9 \text{ mm yr}^{-1}$ (CPRA 2017, Nienhuis et al. 2017).

Although subsidence is often highly spatially variable in wetland environments, recent studies suggest that subsidence in the Davis Pond area is near or slightly below the delta-

wide mean (CPRA 2017, Nienhuis et al. 2017). In the MRD, the rate of relative sea-level rise averages 13 mm yr^{-1} (CPRA 2017, Jankowski et al. 2017). Meanwhile, rates of vertical accretion in the MRD are also spatially variable, but the delta-wide median value is $\sim 11 \text{ mm yr}^{-1}$ (Jankowski et al. 2017).

The $\sim 38 \text{ km}^2$ receiving basin at Davis Pond is bounded by guide levees on three sides. To the south, water exits the basin primarily through seven man-made channels cut through the northwestern rim of Lake Cataouatche. From there, water flows through a series of shallow lakes and marshes, eventually reaching the Gulf of Mexico $\sim 80 \text{ km}$ to the south. Tidal range in Lake Cataouatche is limited to $\sim 10 \text{ cm}$, and tides are diurnal. As a result, water levels in Lake Cataouatche and Davis Pond are primarily driven by meteorological conditions (wind direction and strength) and by variations in diversion discharge.

Construction of Davis Pond was completed in 2002 (<http://www.mvn.usace.army.mil/About/Projects/Davis-Pond-Freshwater-Diversion/>). Although freshwater diversions such as Davis Pond are primarily designed and operated to regulate salinity rather than to build land, a new crevasse splay has emerged at the mouth of the Davis Pond inflow channel. Mouthbar deposits and fringing marsh have begun to fill in previously open ponds. Today, wetlands in the receiving basin are dominated by herbaceous species (*Sagittaria lancifolia*, *Colocasia esculenta*, *Mikania scandens*, and *Polygonum punctatum*) with black willow (*Salix nigra*) colonizing higher elevation islands (CPRA 2015).

In this study, we focus on sediment deposition occurring within the relatively small receiving basin immediately adjacent to the Davis Pond inflow channel (Figure 3.1b). The wetland restoration potential of a diversion is greatest if the majority of the sediment passing through it is retained within the immediate ponding area. The concentration of sediment in a targeted area helps to offset relative sea-level rise and facilitates rapid wetland building. Although sediment that bypasses the Davis Pond receiving basin is likely trapped within the larger Barataria Basin, it is insufficient to build land across this entire area and may be considered lost, at least temporarily, from a wetland restoration perspective.

Davis Pond is one of the smallest engineered diversions currently in operation in the Mississippi River Delta. Some proposed diversions are nearly an order of magnitude larger in terms of discharge. The proposed Mid-Barataria Sediment Diversion, for example, will have a maximum discharge of $\sim 2,100 \text{ m}^3 \text{ s}^{-1}$ (CPRA 2017). Despite the small size of Davis Pond, sediment delivery and deposition in the receiving basin are sufficient to build new land, which is clearly visible in historical satellite imagery (Figure A3.1) and analysis by the Deltares Aqua Monitor (<http://aqua-monitor.deltares.nl>; Donchyts et al. 2016). Additionally, critical similarities exist between Davis Pond and the Mid-Barataria diversion. Both diversions direct water and sediment into an existing framework of deteriorating wetlands rather than into an open bay. For this reason, Davis Pond is in some ways more useful as an analogue for the Mid-Barataria diversion than is the Wax Lake Delta, which is prograding into open water with no wetlands. Yet, the Wax Lake Delta is perhaps the most common analogue for the Mid-Barataria and other

proposed diversions on the lower Mississippi River (e.g. Kim et al. 2009, Allison and Meselhe 2010, Paola et al. 2011). Study of the land building at Davis Pond can better inform the design, operation, and expectations of future diversions that will be critical to restoring the MRD and other deltas around the world.

3. METHODS

3.1. Calculation of seasonal sediment input

Total seasonal sediment input into Davis Pond was calculated using daily measurements of water discharge and turbidity following methods described in Allison et al. (2012). The U.S. Geological Survey (USGS) measures discharge in the Davis Pond inflow channel (29.91694° N, 90.31778° W; USGS 2018a) and turbidity in the Mississippi River at Belle Chasse (29.85694° N, 89.97778° W; USGS 2018b), ~70 river km downstream from Davis Pond (Figure 3.1a). Allison et al. (2012) assumed that turbidity of the water entering Davis Pond is the same as that at Belle Chasse, and we make the same assumption here. Turbidity measurements made at Belle Chasse provide a good estimate of turbidity at Davis Pond because only one significant diversion of Mississippi River water exists between Davis Pond and Belle Chasse. The mean discharge through this other diversion (the Caernarvon Freshwater Diversion) was only $\sim 13 \text{ m}^3 \text{ s}^{-1}$ during 2015, and thus was likely much too small to significantly impact downstream Mississippi River sediment loads. Furthermore, results from Allison et al. (2012) indicate that together Davis Pond Freshwater Diversion, Caernarvon Freshwater Diversion, and the Bonnet Carre Spillway (~15 river km upstream from Davis Pond; Figure 3.1a) account for 50% and 26% of the observed decrease in water discharge and

suspended sediment load, respectively, between Baton Rouge and Belle Chasse. The authors hypothesize that the remaining suspended sediment is deposited and stored in the basin via channel aggradation and/or overbank deposition (Allison et al. 2012). Between Davis Pond and Belle Chasse, the Mississippi River levees closely follow the banks of the river, leaving batture that is generally only 30-300 m wide. Erosion and direct runoff into the river is likely minimal. As a result, turbidity measurements at Belle Chasse provide a minimum estimate for the turbidity of the water entering Davis Pond.

Daily suspended sediment concentration of the Mississippi River at Belle Chasse was calculated by inputting daily turbidity measurements into the following best-fit linear regression based on Belle Chasse data collected by the USGS (Figure 3.3):

$$TSS = 2.047 \times \text{turbidity} + 2.1827 \quad (1)$$

where *TSS*, or total suspended solids, is the mean daily suspended sediment concentration at Belle Chasse (mg L^{-1}) and *turbidity* is the mean daily turbidity at Belle Chasse (formazin nephelometric units, FNU).

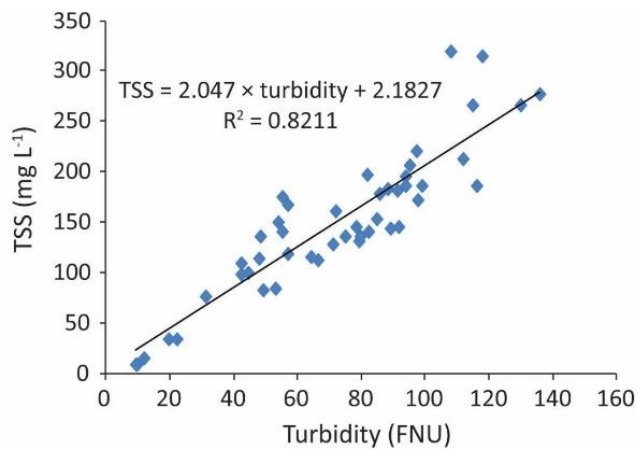


Figure 3.3. Ratings curve used to predict Mississippi River TSS values from measured turbidity at Belle Chasse.

Daily sediment mass input into Davis Pond, $flux_{sed}$, was calculated as

$$flux_{sed} = TSS \times q_{div} \quad (2)$$

where q_{div} is the mean daily discharge through the Davis Pond inflow channel. Total mass of sediment input through the Davis Pond diversion during each study season, $mass_{sed}$, was calculated as

$$mass_{sed} = \int_0^T flux_{sed} dt \quad (3)$$

where $0-T$ is the time interval of interest and t is time. Total mineral sediment input, sed_{input} , was calculated as

$$sed_{input} = mass_{sed} \times mc_{river} \quad (4)$$

where mc_{river} is the average mineral content of Mississippi River suspended sediment (81.54%; Table A3.1). Where gaps existed in the USGS turbidity data (Jun. 16 - Jul. 15 and Oct. 6), values were estimated by linear interpolation between the data points on either side.

3.2. Calculation of Seasonal Sediment deposition

To reconstruct seasonal-scale sediment deposition in Davis Pond, sediment cores 6.5 cm in diameter and 5 cm deep were collected in April and October 2015. Twenty-two coring locations (Figure 3.1b and Table A3.2) were selected to assess lateral and distal variability in sediment mineral content, bulk density, and deposition rate across the receiving basin. Eighteen cores were collected on the marsh platform at elevations ranging from 10 cm above to 25 cm below water level at the time of coring. The four

cores most distal from the diversion inflow channel were collected in 1.5-2 m of water at the northwestern rim of Lake Cataouatche. Initial sampling occurred on April 21, 2015, following an experimental period of high discharge through the diversion from March 13 to March 26. During this period, diversion discharge increased from a mean base flow of $\sim 36 \text{ m}^3 \text{ s}^{-1}$ to a maximum rate of $\sim 300 \text{ m}^3 \text{ s}^{-1}$ (Figure 3.2a). At this time, Mississippi River discharge was rising, nearing its first major peak of the water year (Figure 3.2c). To capture seasonal variability, a second set of cores was collected on October 15, 2015, when river discharge was near minimum for the water year and mean diversion discharge had been $\sim 36 \text{ m}^3 \text{ s}^{-1}$ for the prior ~ 7 months.

In the lab, cores were sectioned into 1-cm depth intervals and analyzed for the following geotechnical parameters (see Tables A3.3 and A3.4): 1) water content, determined by weighing a sample before and after it is dried at 60°C for 24 hours or until a constant weight is reached; 2) mineral content, calculated by combusting a dry sample at 450°C for 6 hours and subtracting the mass loss on ignition; 3) dry bulk density, calculated using water and mineral content (Kolker et al. 2009); and 4) new sediment deposition, determined using activity of the radioisotope beryllium-7 (^7Be) as measured by a low-energy gamma spectrometer (Sommerfield et al. 1999, Esposito et al. 2013; see Figures A3.3 and A3.4). Measurements of mineral content and bulk density were averaged over the interval of ^7Be detection to get a single value for each parameter per core. For cores in which no ^7Be was measured, mineral content and bulk density measurements from the top 1 cm were used for subsequent calculations.

Seasonal sediment deposition was measured using the presence of ^7Be within samples (analyzed at 1-cm depth intervals) as an indicator of newly deposited sediment. ^7Be adheres to mud-size particles and has a short (53-day) half-life, making it an excellent tracer of seasonal-scale sediment dynamics (Sommerfield et al. 1999, Esposito et al. 2013). If a core interval contained detectable surficial ^7Be , the sediments were considered to have been deposited within the last three half-lives of the isotope, or 159 days (Kolker et al. 2012). After three half-lives, the vast majority (87.5%) of the ^7Be has decayed. Sediments in cores containing no detectable ^7Be were considered to have been in place for more than 159 days. At each coring location, the mass of mineral sediment deposited in the previous 159 days, sed_{core} (g cm^{-2}), was calculated as

$$sed_{core} = z_{Be7} \times BD \times mc \quad (5)$$

where z_{Be7} is the depth (cm) to which ^7Be was detected, BD is the dry bulk density (g cm^{-3}), and mc is the mineral content (%) of the sample. Values for sed_{core} were then spatially interpolated across the 13.5 km^2 coring area for each 159-day season using a natural neighbor interpolation algorithm (Sibson 1981) in ArcGIS to provide $sed_{deposit}$, an estimate of the total mineral mass deposited during each season.

Although the coring area encompasses only ~35% of the Davis Pond receiving basin, it includes the channels with the most active sediment transport, as visible in satellite imagery (Figure 3.1b). This visual assessment is supported by data from the two Coastwide Reference Monitoring System (CRMS) stations that are located within the Davis Pond receiving basin (Figures 3.1b and A3.2; <https://www.lacoast.gov/crms2>). At CRMS station 3169, which is located within the coring area (and within the area of high

sediment transport), the top 24 cm of soil show distinct surface-ward trends of increasing bulk density and decreasing organic content, suggesting input of mineral-rich sediment from the diversion. In contrast, at CRMS station 3166, which is located within the receiving basin but outside of the coring area, the top 24 cm of soil have consistently low bulk density and high organic content, suggesting little to no input from the diversion. Additionally, qualitative observations of water flow during field work supported our assertion that waterways outside of the coring area have minimal flow and appear clearer, suggesting they carry less suspended sediment. The locations of these channels remain stable over timescales relevant to this study (months to years; Figure A3.1), and thus our coring area provides a reasonable estimate of basin-wide sediment trapping.

3.3. *Calculation of seasonal sediment retention*

Two study seasons were defined, each the length of three half-lives of ^7Be (159 days) leading up to a core collection date. The winter/spring season is November 14, 2014 to April 21, 2015. The summer/fall season is May 10, 2015 to October 15, 2015. The percent of sediment retained within the receiving basin during each 159-day season, sed_{retain} , was calculated as

$$sed_{retain} = sed_{deposit} / sed_{input} \quad (6)$$

4. RESULTS

4.1. *Geotechnical parameters*

New sediment deposited in the coring area ranged in thickness from 0 to 5 cm in the winter/spring (Figures 3.4a and A3.3) and 0 to 3 cm in the summer/fall (Figures 3.4b

and A3.4). Controlling for distance along the basin axis, the thickness of new sediment was significantly greater in the winter/spring than in the summer/fall, according to a one-way ANCOVA statistical test ($F_{1,721} = 89.92$, $p < .0001$; Figure 3.5a and b).

Spatial patterns of soil mineral content and bulk density corresponded well with field-based qualitative observations of water flow through the Davis Pond receiving basin. In the winter/spring, mineral content ranged from 56% to 96% by mass (Figure 3.4c). Samples collected near the mouth of the inflow channel had the highest mineral content. Adjacent to main channels, mineral content was also high, and generally decreased with downstream distance. Cores with lowest mineral content were collected in areas of backwater marsh where flow was minimal. Soil bulk density in the winter/spring ranged from 0.1 g cm^{-3} to 0.7 g cm^{-3} (Figure 3.4e). Spatial patterns in bulk density were similar to those for mineral content, with higher bulk densities near the mouth of the inflow channel and through the center of the receiving basin in areas proximal to main channels, and lowest bulk densities in areas of backwater marsh with minimal flow and low mineral content. Distributions of mineral content and bulk density were similar in the summer/fall low-flow season (Figures 3.4d and f, respectively), both in terms of the range of measured values and spatial patterns across the study area. Controlling for distance along the basin axis, one-way ANCOVA statistical tests show that there were no significant seasonal differences in soil mineral content ($F_{1,721} = 0.09$, $p > .05$; Figure 3.5c and d) or in bulk density ($F_{1,721} = 0.95$, $p > .05$; Figure 3.5e and f). Detailed sediment core data are available in Tables A3.2-A3.4.

4.2. *Seasonal sediment retention*

In the winter/spring, Davis Pond received an input of 106,800 metric tons of mineral sediment from the Mississippi River, based on measurements of water discharge and turbidity. During this time, mean turbidity of the Mississippi River was 56 FNU, and mean flow velocity in the Davis Pond inflow channel was 0.21 m s^{-1} . Forty-four percent of the mineral sediment flux (47,100 metric tons) was deposited and retained within the 13.5 km^2 coring area. Figure 3.4g shows the spatial distribution of new mineral sediment accumulation. Table 3.1 summarizes seasonal parameters affecting sedimentation.

In the summer/fall, Davis Pond received 35,900 metric tons of mineral sediment from the Mississippi River, about one-third of the sediment mass received in the winter/spring (Table 3.1). According to a one-way ANCOVA statistical test, mineral sediment accumulation was significantly greater in the winter/spring than in the summer/fall, controlling for distance along the axis of the basin ($F_{1,722} = 111.47$, $p < .0001$; Figure 3.5g and h). In the summer/fall, mean turbidity of the Mississippi River was 55 FNU (calculated using the 128 days of available data), and mean flow velocity in the Davis Pond inflow channel was 0.10 m s^{-1} . Although mineral sediment input decreased from the winter/spring to the summer/fall and water turbidity remained the same, sediment retention increased to 81%, as 28,900 metric tons of mineral sediment were deposited in the 13.5 km^2 coring area (Figure 3.4h).

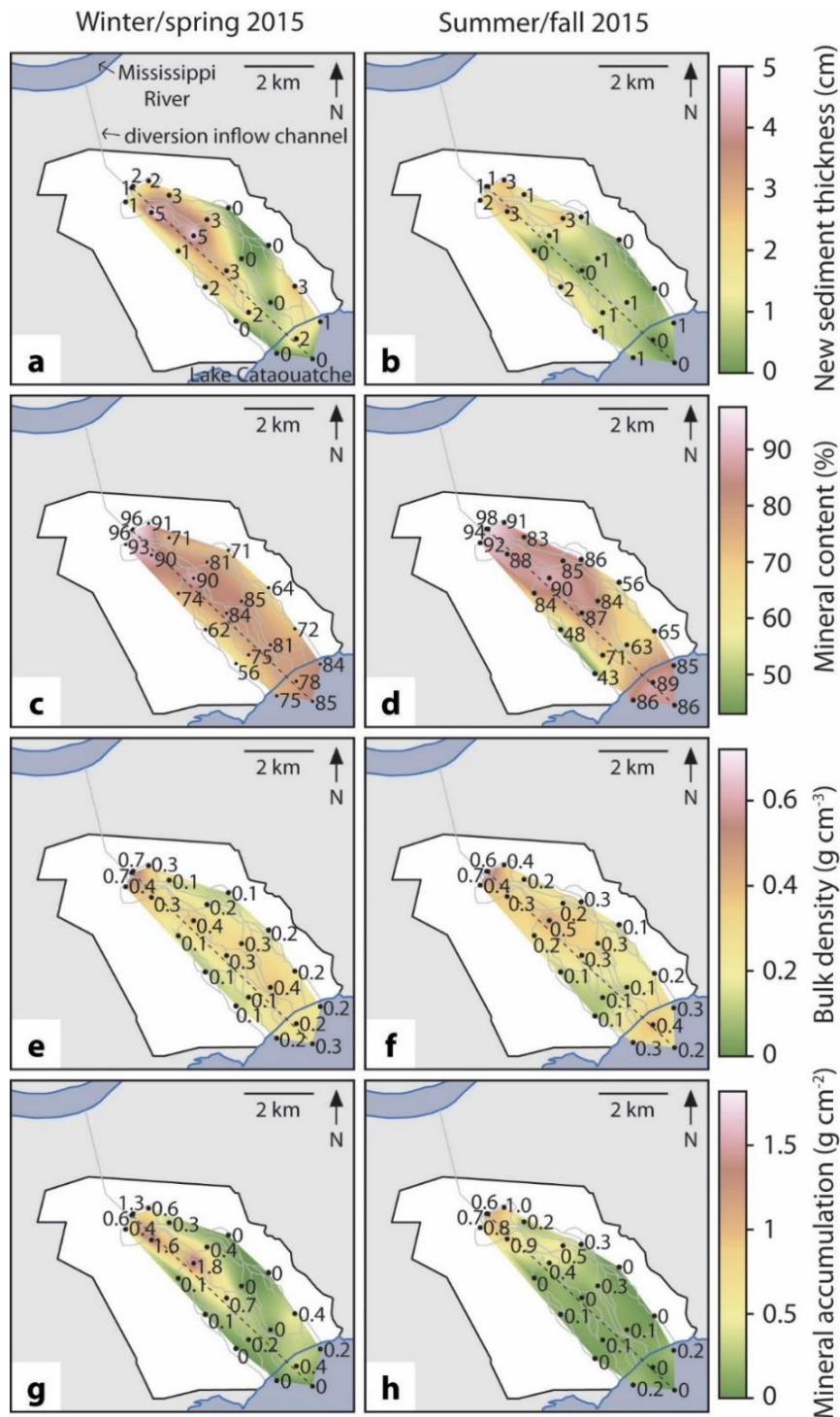


Figure 3.4. Measurements and natural neighbor interpolation of new sediment thickness (a, b), mineral content (c, d), and bulk density (e, f), and calculated mineral accumulation (g, h) at 22 coring locations in the winter/spring and the summer/fall of 2015. Solid grey lines indicate major flow paths through the receiving basin (determined visually from satellite imagery, Figure 3.1b). Dashed black lines indicate the lines of section used in Figure 3.5.

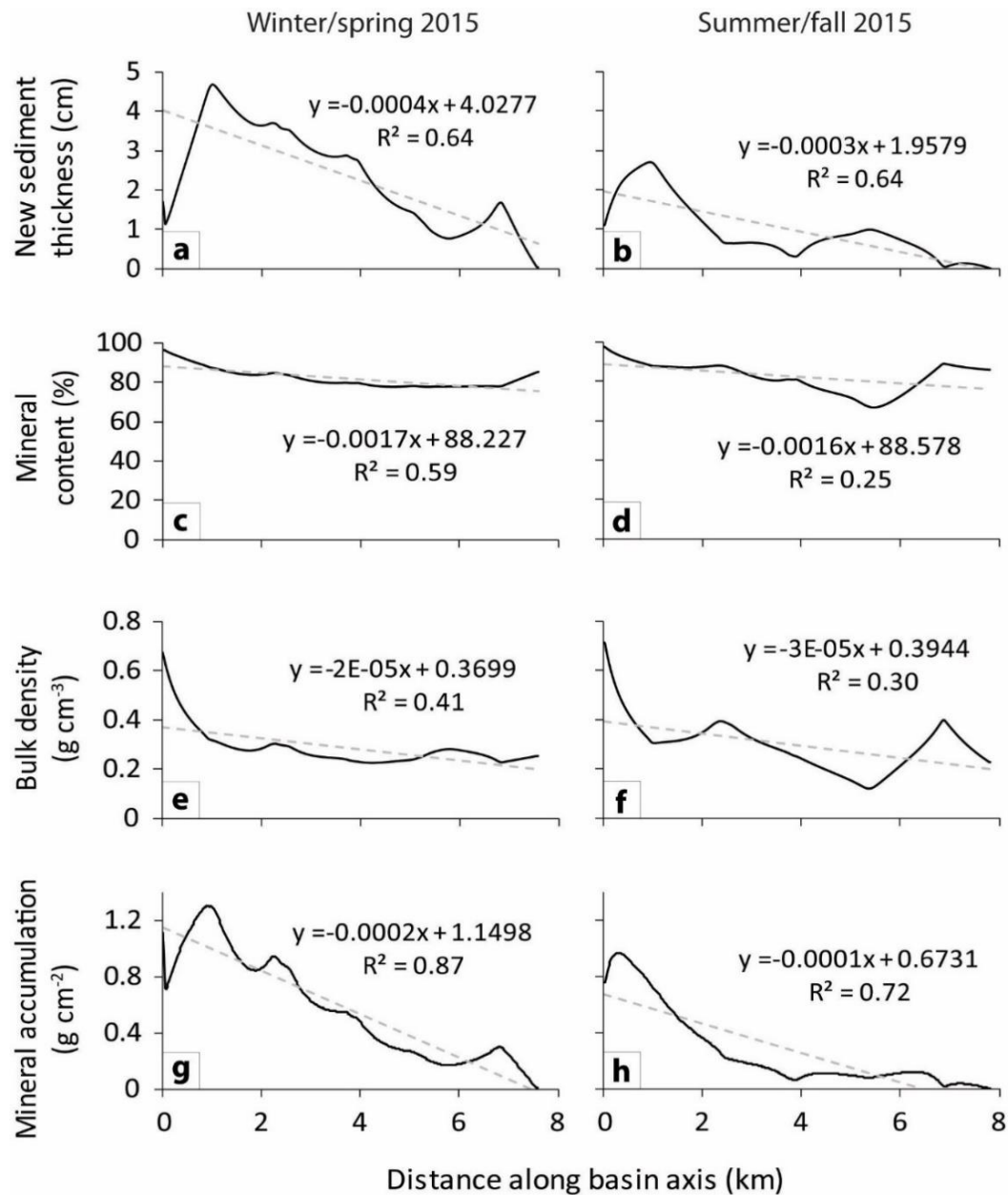


Figure 3.5. Changes in soil geotechnical parameters with distance along the basin axis, in the winter/spring and the summer/fall of 2015. Each profile is constructed from the natural neighbor interpolation data shown in Figure 3.4. See Figure 3.4 for locations of the lines of section.

Table 3.1. Summary of parameters affecting sedimentation within the Davis Pond receiving basin for the two study seasons.

Parameter	Winter/Spring 2015 (Nov 14, 2014 - Apr 21, 2015)	Summer/Fall 2015 (May 10, 2015 - Oct 15, 2015)
Mean water discharge into Davis Pond	62 m ³ s ⁻¹	26 m ³ s ⁻¹
Mass of mineral sediment input into Davis Pond:	106,800 metric tons (656 metric tons day ⁻¹)	35,900 metric tons (220 metric tons day ⁻¹)
Mass of mineral sediment deposited in receiving basin:	47,100 metric tons (296 metric tons day ⁻¹)	28,900 metric tons (182 metric tons day ⁻¹)
Percent of mineral sediment retained in receiving basin:	44%	81%
Mean Mississippi River turbidity at Belle Chasse:	56 FNU	55 FNU
Mean flow velocity in Davis Pond inflow channel:	0.21 m s ⁻¹	0.10 m s ⁻¹

5. DISCUSSION

5.1. Controls on sediment retention

5.1.1. Water discharge, velocity, and turbidity

High sediment flux through the Davis Pond diversion during the winter/spring corresponds with the typical springtime rise in the Mississippi River hydrograph (Figure 3.2c). Sediment stored on the riverbed is remobilized by the increased flow, increasing river TSS concentrations, and is subsequently conveyed through the diversion. The winter/spring season also included a rare two-week pulse of high discharge into Davis Pond that provided ideal conditions for the natural experiment studied here. During this time, the discharge was roughly tenfold higher and velocities roughly double those that

occurred during typical diversion operations for the remainder of the winter/spring (Figure 3.2a, Table 3.1). Increased velocity may account for the lower sediment retention in the winter/spring as compared to the summer/fall. Faster flow retains more sediment in suspension and decreases water residence time in the receiving basin. Accumulation of new sediment at the edge of Lake Cataouatche was slightly higher in the winter/spring than in the summer/fall (Figures 3.4g and h), suggesting more throughput of suspended sediment during the period of elevated flow velocity. Sediment bypassed the receiving basin and settled out of suspension at the edge of the lake, where the channelized flow spread out and slowed.

In the summer of 2015, Mississippi River discharge remained unusually high, exceeding $17,000 \text{ m}^3 \text{ s}^{-1}$ until mid-August (Figure 3.2c). Despite the elevated river discharge, average discharge through Davis Pond diversion in summer/fall was less than half of what it was in the winter/spring, and mineral sediment delivery to the diversion decreased by two-thirds. Though the drop in sediment input is primarily due to the decrease in diversion discharge, it is likely also due in part to a decrease in Mississippi River TSS concentration from the winter/spring to the summer/fall that is not fully captured in the average measurements reported here due to gaps in the USGS turbidity data (Figure 3.6a). The USGS has continuous turbidity data for previous years, however. From the winter/spring to the summer/fall, turbidity dropped by 38% in 2013 and 13% in 2014. In a typical year, the bulk of the sediment stored on the riverbed is remobilized during the first large flood pulse of the spring (Mossa 1996, Snedden et al. 2007). Less

sediment is available for remobilization during subsequent flood pulses later in the summer.

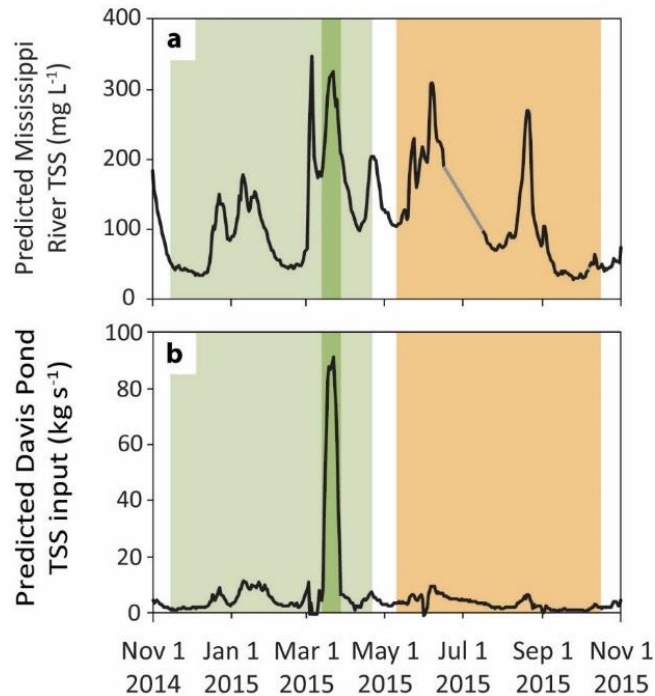


Figure 3.6. Predicted Mississippi River TSS at Belle Chasse (a) and predicted TSS input into Davis Pond (b) from Nov. 1, 2014 to Oct. 31, 2015. In panel a, grey line segments indicate linear interpolations used to fill gaps in the USGS data. The two 159-day seasons used for analysis are shaded: winter/spring is green and summer/fall is orange. The dark green bar in the winter/spring season marks the two-week experimental high discharge event in Davis Pond.

5.1.2. Vegetation

In addition to hydrodynamic regime, vegetation type and density also impact sediment retention rates in wetlands. In general, wetland vegetation tends to decrease water flow velocity and thus decrease turbulence and shear stress at the soil-water interface and reduce soil erosion (Leonard and Luther 1995, Neumeier and Ciavola 2004, Gedan et al. 2011). Previous work has shown that vegetation biomass in marshes is typically maximized at the end of summer (Hopkinson et al. 1978), and several studies

have identified linkages between vegetation density and sediment deposition in salt marshes (e.g. Kadlec 1990, Leonard and Luther 1995, Christiansen et al. 2000, Fagherazzi et al. 2012). In deltaic freshwater marshes, Nardin and Edmonds (2014) found that vegetation of moderate height and density maximizes sediment deposition during river floods. Thus, our fall 2015 cores from Davis Pond include material deposited over the summer growing season when vegetation conditions were near optimal for sediment trapping. This vegetation effect likely contributes to the observed increase in sediment retention from the winter/spring to the summer/fall.

5.1.3. Basin geometry and energy level

The high sediment trapping efficiency we observed in Davis Pond may partially result from the closed geometry and sheltered nature of the receiving basin (Figure 3.7a). Water flows out of the receiving basin and into Lake Cataouatche via seven discrete channels, and each channel mouth is armored to prevent widening. Guide levees prevent lateral flow. This restricted geometry forces water to pond within the receiving basin, decreasing flow velocity and increasing residence time, both of which contribute to increased sediment deposition. In contrast, Wax Lake Delta is prograding into Atchafalaya Bay, restricted only by the pre-existing shoreline (Figure 3.7b). Flow velocity there remains relatively high ($0.05\text{--}0.73\text{ m s}^{-1}$ depending on the tide, Shaw and Mohrig 2014), carrying sediment, particularly mud, out of the semi-enclosed basin. The Birdfoot Delta is an open basin, unrestricted by levees below 16.5 km above Head of Passes (Figure 3.7c). Here, distributaries flow directly into the Gulf of Mexico near the edge of the continental shelf. High river velocity exports sediment into the Gulf, where it

is subject to continued suspension by wind, waves, and currents. As a result, local sediment retention in the Birdfoot Delta is likely low (Wright 1977).

Although our coring area encompasses only ~35% of the Davis Pond receiving basin, it includes all major sediment transport channels and adjacent marsh platform (Figure 3.1b) and thus provides a good estimate of sediment retention in entire receiving basin. Any deposition that occurs in more lateral sections of the receiving basin (and thus not captured in this study) is expected to be very minor. Studies of other crevasse splays (e.g. Esposito et al. 2017) indicate that sediment deposition can be laterally extensive if the depositional basin is unconstrained. But the channels within the Davis Pond receiving basin are tightly constrained. On the west side of the basin, pre-existing topography from an 1884 crevasse splay (visible in satellite images as linear forested ridges) deflects modern channels to the southeast. To the east, intact and un-channelized marsh creates a barrier to substantial water flow. At the southern end of the basin, channel mouths are armored with rip rap and sheet piling to prevent widening and lateral migration. In addition, an examination of historical satellite imagery (Figure A3.1) shows that sediment-laden water is consistently confined to the center of the receiving basin (through time and varying water levels), coincident with our coring area. Bulk density and organic content data from CRMS stations 3169 and 3166 (Figure A3.2) further support these observations. Together, these lines of evidence strongly suggest that sediment deposition is extremely minimal in the lateral portions of the Davis Pond receiving basin. Any deposition that occurs outside of our coring area is not included in our estimates of sediment deposition, and thus our results are conservative. On the other

hand, the coring area includes $\sim 1.2 \text{ km}^2$ at the edge of Lake Cataouatche, which is outside of the receiving basin. Sediment deposition at the edge of Lake Cataouatche builds the initial subaqueous platform necessary for new marsh growth and thus is also useful for wetland restoration.

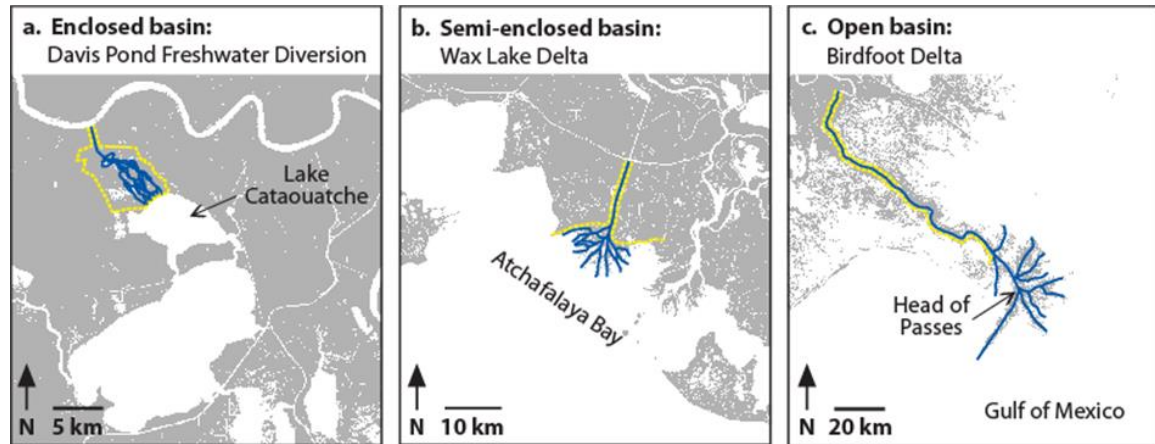


Figure 3.7. Three basin geometry types. Solid blue lines indicate major water flow paths and dashed yellow lines indicate levees or restrictive shorelines. See Figure 3.1a for basin locations.

5.2. Comparison with other systems

Exceeding 80% during parts of the year, sediment retention in Davis Pond (Table 3.1) is higher than in many deltaic wetlands around the world (e.g. Nittrouer et al. 1995, Allison et al. 1998, Draut et al. 2005, Törnqvist et al. 2007, Blum and Roberts 2009). Blum and Roberts (2009) estimate that deltas typically trap between 30% and 70% of sediment and use an estimated delta-wide trapping efficiency of 40% for their calculations of land loss in the Mississippi River Delta. Long-term (multi-decadal to century-scale) sediment retention has been measured at 39-71% in the Ganges-Brahmaputra Delta (using a field-based approach with methodologies similar to those presented in this manuscript; Allison et al. 1998), 33% in the Amazon Delta (using a

mass-balance approach and a review of field-based methods; Nittrouer et al. 1995), 23% in Wax Lake Delta (using both a mass balance and a geometric approach; Törnqvist et al. 2007), and 27% in greater Atchafalaya Bay (using a mass-balance approach; Draut et al. 2005).

The spread in retention rates measured in these global deltas is largely due to the range of energy levels in their depositional environments (Roberts et al. 2015). Whereas these deltas with lower rates of sediment retention are all prograding into open water and subject to waves and currents, the Davis Pond diversion is building land within a framework of existing, sheltered marsh. This low-energy environment allows the deposition and retention of mud-size sediment. In contrast to Wax Lake Delta deposits, which are sand-dominated (Roberts et al. 2003), typical crevasse splay deposits in the MRD consist of $\geq 95\%$ mud (Snedden et al. 2007, Esposito et al. 2017). Furthermore, Esposito et al. (2017) find that crevasse splays that are building into protected environments (such as Davis Pond) experience sediment retention rates that exceed 75% and may approach 100%.

Sedimentation at Davis Pond is comparable to that in the immediate ponding area of the Caernarvon Freshwater Diversion, another controlled Mississippi River diversion located ~60 km downstream. Annual mineral sediment input was 152,300 metric tons at Davis Pond (Nov. 2014 – Oct. 2015; this study) and 100,000 to 130,000 metric tons at Caernarvon (Feb. 2003 – January 2004; Snedden et al. 2007). During the respective study years, the two diversions experienced similar average annual diversion discharge ($43 \text{ m}^3 \text{ s}^{-1}$ at Davis Pond and $42 \text{ m}^3 \text{ s}^{-1}$ at Caernarvon) despite different hydrodynamic regimes.

Flood pulses at Caernarvon were more frequent (2 per year) but had lower discharge ($140\text{--}200\text{ m}^3\text{ s}^{-1}$) and were separated by long periods of zero or near-zero discharge. At Davis Pond, flood pulses were less frequent (1 per year) but had high discharge ($280\text{ m}^3\text{ s}^{-1}$) and typical non-flood discharge was well above zero ($36\text{ m}^3\text{ s}^{-1}$). During water years 2008-2010, water and mineral sediment input were higher for both diversions, although still within the same order of magnitude (Allison et al. 2012). During these years, Davis Pond and Caernarvon received an average of 390,000 and 273,000 metric tons of mineral sediment per year, respectively (calculated using 81.54% as the average mineral content of Mississippi River suspended sediment; Table A3.1).

Seasonal rates of mineral sediment deposition and retention in Davis Pond are also comparable to the rates observed in Caernarvon. Flood season (winter/spring) deposition averaged $22\text{ g m}^{-2}\text{ d}^{-1}$ in the Davis Pond coring area (this study) and $15\text{--}20\text{ g m}^{-2}\text{ d}^{-1}$ (at minimum) in areas within 6 km of the Caernarvon diversion structure (Wheelock 2003). Sediment retention during this time was 44% in Davis Pond (this study) and 48% in Caernarvon (synthesizing sediment deposition data from Wheelock 2003 with co-incident sediment input data from Snedden et al. 2007). Non-flood season (summer/fall) deposition averaged $13\text{ g m}^{-2}\text{ d}^{-1}$ in Davis Pond and $5\text{ g m}^{-2}\text{ d}^{-1}$ in Caernarvon, and sediment retention was 81% in Davis Pond and 78% in Caernarvon.

5.3. Implications for coastal restoration

Efficient sediment trapping in coastal wetlands is critical in order to restore the MRD. Dam construction in the Mississippi River watershed has reduced the suspended sediment load in the river by half (Blum and Roberts 2009). Meanwhile, the current rate

of relative sea-level rise in the MRD averages 13 mm yr^{-1} (CPRA 2017, Jankowski et al. 2017). Although the rapid progradation of Wax Lake Delta indicates that the sediment load in the modern Mississippi River is sufficient to build substantial amounts of land (Shaw and Mohrig 2014), the remaining sediment in the river is a critical resource. For river diversions to be successful in building new deltaic wetlands in the face of subsidence and rising sea levels, sediment deposition and retention must be jointly maximized in the receiving basins. Scaling relationships for many hydrological processes are well known (e.g. Leopold 1994) and in some cases have been validated for diversion-like settings (e.g. Snedden et al. 2007, Esposito et al. 2013, Shaw et al. 2018), providing a pathway for engineering studies to optimize water discharge and velocity in future diversions. While not the central focus of this study, diversion engineering and operation management will likely also incorporate an understanding of ecosystem impacts in the receiving basin and impacts to navigation in the Mississippi River (Allison and Meselhe 2010, De Mutsert et al. 2017, Peyronnin et al. 2017).

Previous work has shown that high-discharge flood pulses are critical for delta building and, in some locations, may deposit enough sediment to offset relative sea-level rise (Snedden et al. 2007, Kolker et al. 2012, Esposito et al. 2013, Rosenheim et al. 2013, Carle et al. 2015, Shen et al. 2015). In Davis Pond, an experimental pulse of high discharge (March 13-26, 2015) delivered 41% of the total annual sediment supply in just 14 days (Figure 3.6b). Although erosion may occur during periods of high discharge, modeling by Nienhuis et al. (2018) indicates that maximum land building in a crevasse splay occurs when rates of sediment deposition and erosion are balanced.

A conceptual model constructed from our data (Figure 3.8) suggests that, for a given TSS concentration and diversion discharge capacity, moderate mean water discharge (which could encompass flood pulses and periods of lower discharge) may maximize sediment deposition in a developing delta. To construct this conceptual model, we first built a sediment input curve (blue curve, Figure 3.8a) by relating observations of daily diversion discharge (Figure 3.2a) to sediment input (Figure 3.6b) using a power function. Next, we developed a sediment retention curve (red curve, Figure 3.8a) by fitting an exponential function through our two sediment retention data points (Table 3.1) and setting the y-intercept to 100%. We chose an exponential function because it asymptotes to zero and sediment retention is unlikely to reach 0%, and a y-intercept of 100% because zero discharge logically produces 100% sediment retention. To generate a hypothesis about sediment retention at discharges greater than those observed in Davis Pond during our study period, we extrapolated the curve to higher discharges. Finally, we developed a sediment deposition curve (Figure 3.8b) by multiplying the sediment input curve by the sediment retention curve. Our conceptual model suggests that as water discharge and sediment input increase, throughput of suspended sediment also increases, leading to a decrease in the basin sediment retention rate. Meanwhile, sediment deposition may eventually reach a maximum where further increases in sediment input no longer lead to greater deposition because the reduced retention rates at higher discharges completely offset the increased sediment input.

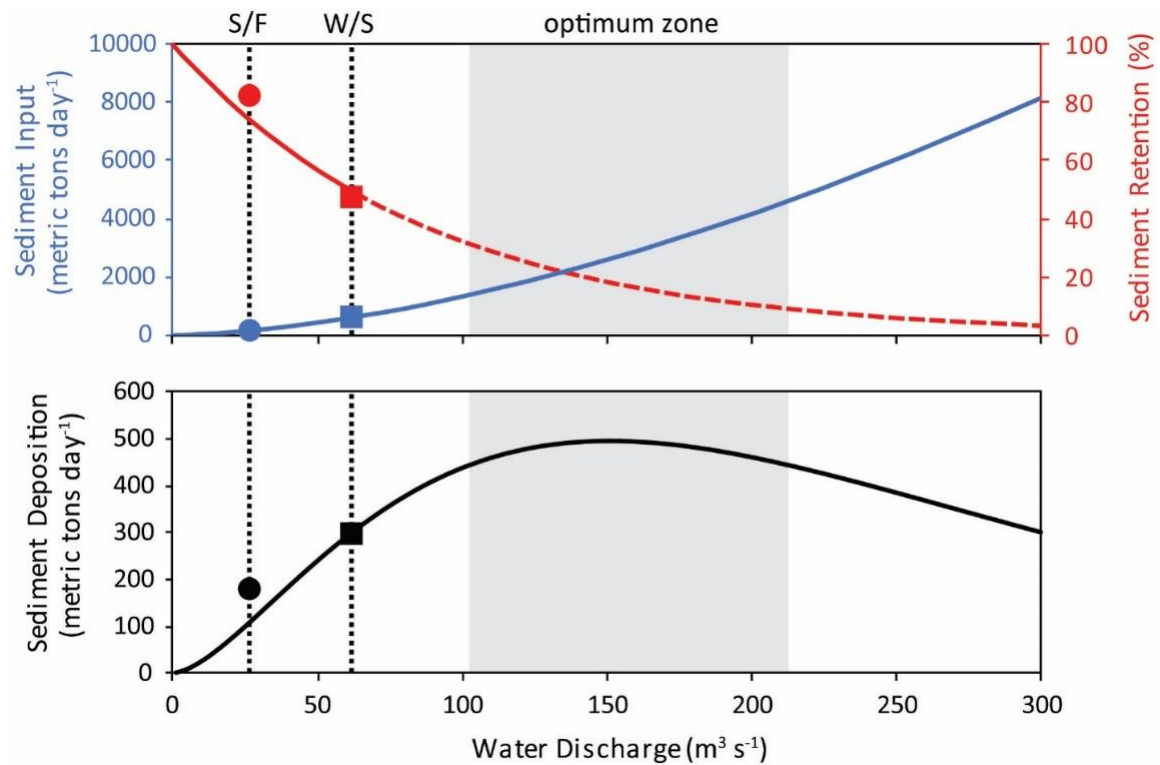


Figure 3.8. (a) Conceptual model relating sediment input (blue) and retention rate (red) to diversion water discharge. The dashed portion of the retention curve offers a hypothesis for sediment retention at discharges higher than those observed in this study. (b) Receiving basin deposition rates predicted by the conceptual model. See text for details on how the curves were constructed. The shaded “optimum zone” encompasses discharges that result in $\geq 90\%$ of maximum sediment deposition. Our observations for the winter/spring (W/S) and the summer/fall (S/F) seasons (Table 3.1) are indicated by the squares and circles, respectively.

The range of moderate discharges that lead to near-maximum sediment deposition are considered optimum in terms of land building. For Davis Pond, discharges within this optimum range are greater than the mean discharges seen during either the winter/spring or the summer/fall seasons studied here, but notably lower than the maximum discharge of the diversion ($\sim 300 \text{ m}^3 \text{s}^{-1}$). At discharges significantly higher than those observed in the present study, we hypothesize that sediment deposition and retention will both decrease. Note that the moderate discharges we describe here as optimal are approximately double to triple the mean discharge seen in the winter/spring of 2015,

which we refer to as our “high-flow” season in order to distinguish it from the low-flow summer/fall 2015 season. In reality, mean discharge during the winter/spring of 2015 was also relatively low, at only 21% of the maximum diversion discharge.

We expect that additional measurements of sediment retention (collected in future studies) will slightly alter the shape of the sediment retention curve seen in Figure 3.8a and thus slightly shift the optimum discharge value (Figure A3.5). However, we expect that the shape of these curves will remain generally the same. Sediment retention cannot exceed 100% and is unlikely to drop to 0%. Thus, additional data will refine our conceptual model and it is likely that an optimum discharge will continue to be evident.

The conceptual model presented here uses parameters specific to the Davis Pond diversion. These parameters (e.g. maximum diversion discharge, rate of sediment input, measurements of sediment retention) can be changed to fit other diversions. Because no two diversions are identical, the zone of optimum discharge is expected to be different for each diversion. However, scaling relationships in hydrology (e.g. Leopold 1994) coupled with a wealth of regional studies (e.g. Allison and Meselhe 2010, Esposito et al. 2013, Peyronnin et al. 2017) and site-specific data provide a means by which this conceptual model can be applied to other systems in the MRD and globally.

Determining optimal flow regime conditions for river diversions is an emerging area of concern for water managers in the MRD (e.g. Peyronnin et al. 2017) and in basins around the world such as the Shatt al-Arab Delta in Iraq (Richardson et al. 2005) and the Ganges-Brahmaputra Delta in Bangladesh (van Staveren et al. 2017). Our findings suggest that optimal discharge conditions for maximizing sediment accumulation at

Davis Pond may exceed those observed here. The validity of this conclusion could be objectively assessed with future investigations that quantify retention rates under higher diversion discharge conditions, using methods applied here or perhaps with a mass-balance approach applied to continuous flux measurements made at the upstream and downstream ends of the receiving basin. Results from future studies can be used to test and refine the conceptual model presented here and adapt it for use in other delta basins.

6. CONCLUSIONS

In this study of a river diversion in the Mississippi River Delta, we quantify relationships between hydrodynamics and sedimentation in a developing delta. We reach the following conclusions:

- Although greater water discharge delivers more sediment to the receiving basin, the corresponding rate of sediment retention is decreased, likely because more of the sediment is retained in suspension and carried out of the basin.
- Thus, increasing discharge results in diminishing returns in terms of sediment deposition.
- As a result, there may be an optimum that occurs at moderate discharge where sediment deposition is maximized.
- Discharges above this optimum zone would result in decreased sediment deposition.

Findings from this research suggest that planning for future diversions may more explicitly investigate sediment trapping efficiency. Maximizing the beneficial impact of river diversions to restoration and management of coastal wetland ecosystems requires an understanding of how to achieve optimal hydrodynamic conditions for sustainable delta building. Diversions of moderate water discharge and flow velocity that discharge into enclosed receiving basins may be effective configurations to explore when planning for future sediment diversions to maximize the land-building potential of the Mississippi River's remaining sediment load.

7. ACKNOWLEDGEMENTS

This work was funded in part by the U.S. Geological Survey, the PADI Foundation, and through the Restore the Mississippi River Delta with support from the Walton Family Foundation. We appreciate thoughtful reviews by two anonymous referees that led to considerable improvement of the manuscript. Thanks to Brandon Boyd, Hongqing Wang, and two anonymous referees for helpful reviews of a previous version. Any use of trade, firm, or product names is for descriptive purposes only and does not imply endorsement by the U.S. Government.

8. DATA AVAILABILITY

All data associated with this manuscript are available on ScienceBase: doi: 10.5066/P9V7N49P.

CONCLUSIONS

In the modern era of accelerated sea-level rise, wetlands in coastal Louisiana are canaries in the coal mine for global environmental change. With its low tidal range and limited elevation, the region is especially sensitive to changes in sediment availability and water level. Globally, low-elevation coastal zones are continually shaped by a balance of accretionary and erosional processes as well as extensive anthropogenic modification.

This dissertation examined processes of sediment accumulation, compaction, and relative sea-level rise in coastal wetlands and assessed strategies for restoration. I reached the following main conclusions:

- In wetland soils, organic content strongly controls sediment compaction. Wetland soils, especially those with high organic content, are highly susceptible to compaction.
- At least 80% of compaction happens quickly, largely within the first 100 years after deposition and in the top 1 m of the subsurface.
- This rapid shallow compaction is generally not recorded by traditional methods of measuring relative sea-level rise in low-elevation coastal zones (i.e. tide gauges and GNSS stations).

- Thus, tide gauges underestimate rates of relative sea-level rise in low-elevation coastal zones.
- As a result, low-elevation coastal zones may be at a greater risk of flooding than previously realized.
- Despite accelerated rates of relative sea-level rise and rapid sediment compaction, coastal restoration efforts such as river diversions can be successful in building new land in some areas.
- Wetlands are more likely to keep up with relative sea-level rise if hydrodynamic conditions are optimized to retain mineral sediment in targeted restoration areas.

Coastal wetlands are critical ecosystems, both economically and ecologically, and thus the study of sediment compaction, relative sea-level rise, and wetland restoration is not merely of academic interest. The research discussed here can inform future action to help stem the tide of coastal land loss in the Mississippi Delta and worldwide.

LIST OF REFERENCES

- Adame, M.F., Neil, D., Wright, S.F., and Lovelock, C.E. 2010. Sedimentation within and among mangrove forests along a gradient of geomorphological settings. *Estuarine, Coastal, and Shelf Science* 86, 21-30.
- Adams, W.A. 1973. The effect of organic matter on the bulk and true densities of some uncultivated podzolic soils. *Journal of Soil Science*, 24, 10-17.
- Alam, M. 1996. Subsidence of the Ganges-Brahmaputra Delta of Bangladesh and associated drainage, sedimentation and salinity problems, in: *Sea-Level Rise and Coastal Subsidence*. Ed.: Milliman, J. D. and Haq, B. U., Springer, Dordrecht, The Netherlands, 169-192.
- Allison, M.A., Kuehl, S.A., Martin, T.C., and Hassan, A. 1998. Importance of flood-plain sedimentation for river sediment budgets and terrigenous input to the oceans: Insights from the Brahmaputra-Jamuna River. *Geology* 26, 175-178.
- Allison, M.A. and Meselhe, E.A. 2010. The use of large water and sediment diversions in the lower Mississippi River (Louisiana) for coastal restoration. *Journal of Hydrology* 387, 346-360.
- Allison, M.A., Demas, C.R., Ebersole, B.A., Kleiss, B.A., Little, C.D., Meselhe, E.A., Powell, N.J., Pratt, T.C., and Vosburg, B.M. 2012. A water and sediment budget for the lower Mississippi-Atchafalaya River in flood years 2008–2010:

- Implications for sediment discharge to the oceans and coastal restoration in Louisiana. *Journal of Hydrology* 432-433, 84-97.
- Allison, M., Yuill, B., Törnqvist, T., Amelung, F., Dixon, T.H., Erkens, G., Stuurman, R., Jones, C., Milne, G., Steckler, M., Syvitski, J., and Teatini, P. 2016. Global risks and research priorities for coastal subsidence. *Eos*, 97(19), 22-27.
- Amer, R., Kolker, A.S., and Muscietta, A. 2017. Propensity for erosion and deposition in a deltaic wetland complex: Implications for river management and coastal restoration. *Remote Sensing of Environment*, 199, 39-50.
- Amorosi, A., Bruno, L., Cleveland, D. M., Morelli, A., and Hong, W. 2017. Paleosols and associated channel-belt sand bodies from a continuously subsiding late Quaternary system (Po Basin, Italy): New insights into continental sequence stratigraphy. *Geological Society of America Bulletin*, 129, 449-463.
- Auerbach, L.W., Goodbred Jr., S.L., Mondal, D.R., Wilson, C.A., Ahmed, K.R., Roy, K., Steckler, M.S., Small, C., Gilligan, J.M., and Ackerly, B.A. 2015. Flood risk of natural and embanked landscapes on the Ganges–Brahmaputra tidal delta plain. *Nature Climate Change*, 5, 153-157.
- Baldwin, B. 1971. Ways of deciphering compacted sediments. *Journal of Sedimentary Petrology*, 41, 293-301.
- Barras, J. 2006. Land area change in coastal Louisiana after the 2005 hurricanes: A series of three maps. U.S. Geological Survey Open File Report 06-1274.

- Begy, R.-C., Preoteasa, L., Timar-Gabor, A., Mihăiescu, R., Tănăsolia, C., Kelemen, S., and Simon, H. 2016. Sediment dynamics and heavy metal pollution history of the Cruhlig Lake (Danube Delta, Romania). *Journal of Environmental Radioactivity*, 153, 167-175.
- Bettinetti, A., Pypaert, P., and Sweerts, J.-P. 1996. Application of an integrated management approach to the restoration project of the Lagoon of Venice. *Journal of Environmental Management*, 46, 207-227.
- Bird, M.I., Fifield, L.K., Chua, S., and Goh, B. 2004. Calculating sediment compaction for radiocarbon dating of intertidal sediments. *Radiocarbon*, 46, 421-435.
- Bloom, A.L. 1964. Peat accumulation and compaction in a Connecticut coastal marsh. *Journal of Sedimentary Petrology*, 34, 599-603.
- Blum, M.D. and Roberts, H.H. 2009. Drowning of the Mississippi Delta due to insufficient sediment supply and global sea-level rise. *Nature Geoscience* 2, 488-491.
- Brain, M.J., Kemp, A.C., Horton, B.P., Culver, S.J., Parnell, A.C., and Cahill, N. 2015. Quantifying the contribution of sediment compaction to late Holocene salt-marsh sea-level reconstructions, North Carolina, USA. *Quaternary Research*, 83, 41-51.
- Braskerud, B.C. 2001. The influence of vegetation on sedimentation and resuspension of soil particles in small constructed wetlands. *Journal of Environmental Quality* 30, 1447-1457.

- Brevik, E.C. and Homburg, J.A. 2004. A 5000 year record of carbon sequestration from a coastal lagoon and wetland complex, Southern California, USA. *Catena*, 57, 221-232.
- Bricker-Urso, S., Nixon, S.W., Cochran, J.K., Hirschberg, D.J., and Hunt, C. 1989. Accretion rates and sediment accumulation in Rhode Island salt marshes. *Estuaries*, 12, 300-317.
- Bridgeman, J.G. 2018. Understanding Mississippi Delta subsidence through stratigraphic and geotechnical analysis of a continuous Holocene core at a subsidence superstation. Master's thesis, Tulane University, 96 p.
- Cahoon, D. R. 2015. Estimating relative sea-level rise and submergence potential at a coastal wetland. *Estuaries and Coasts*, 38, 1077-1084.
- Cahoon, D.R., Reed, D.J., and Day Jr., J.W. 1995. Estimating shallow subsidence in microtidal salt marshes of the southeastern United States: Kaye and Barghoorn revisited. *Marine Geology*, 128, 1-9.
- Carle, M.V., Sasser, C.E., and Roberts, H.H. 2015. Accretion and vegetation community change in the Wax Lake Delta following the historic 2011 Mississippi River flood. *Journal of Coastal Research* 31, 569-587.
- Catianis, I., Rădan, S., and Grosu, D. 2014. Loss of ignition as a proxy indicator for assessing the lithological composition of the recent sediments accumulated in some freshwater lakes from the Danube Delta, Romania. *International Journal of Innovation and Applied Studies*, 9, 260-278.

Chamberlain, E.L. 2017. Dating deltas. PhD dissertation, Tulane University, 184 p.

Christiansen, T., Wilberg, P.L., and Milligan, T.G. 2000. Flow and sediment transport on a tidal salt marsh surface. *Estuarine, Coastal, and Shelf Science* 50, 315-331.

Church, J. A. and White, N. J. 2011. Sea-level rise from the late 19th to the early 21st century. *Surveys in Geophysics*, 32, 585-602.

Church, J.A., Clark, P.U., Cazenave, A., Gregory, J.M., Jevrejeva, S., Levermann, A., Merrifield, M.A., Milne, G.A., Nerem, R.S., Nunn, P.D., Payne, A.J., Pfeffer, W.T., Stammer, D., and Unnikrishnan, A.S. 2013. Sea Level Change, in: *Climate Change 2013: The Physical Science Basis, Contribution of Working Group I to the Fifth Assessment Report of the Intergovernmental Panel on Climate Change*. Ed.: Stocker, T.F., Qin, D., Plattner, G.-K., Tignor, M., Allen, S.K., Boschung, J., Nauels, A., Xia, Y., Bex, V., and Midgley, P.M., Cambridge University Press, New York, NY, USA, 1137-1216.

Cipollini, P., Calafat, F.M., Jevrejeva, S., Melet, A., and Prandi, P. 2017. Monitoring sea level in the coastal zone with satellite altimetry and tide gauges. *Surveys in Geophysics*, 38, 33-57.

Clift, P.D., Giosan, L., Carter, A., Garzanti, E., Galy, V., Tabrez, A.R., Pringle, M., Campbell, I.H., France-Lanord, C., Blusztajn, J., Allen, C., Alizai, A., Lückge, A., Danish, M., and Rabbani, M.M. 2010. Monsoon control over erosion patterns in the Western Himalaya: possible feed-back into the tectonic evolution. *Geological Society Special Publication*, 342, 185-218.

Coastal Protection and Restoration Authority (CPRA) of Louisiana. 2017. Louisiana's comprehensive master plan for a sustainable coast. Baton Rouge, LA, 184 p.

Coastal Protection and Restoration Authority (CPRA) of Louisiana. 2018. Coastwide Reference Monitoring System-Wetlands Monitoring Data. Retrieved from Coastal Information Management System (CIMS) database. Available at: <http://cims.coastal.louisiana.gov>. Accessed on 27 February 2019.

Couvillion, B.R., Barras, J.A., Steyer, G.D., Sleavin, W., Fischer, M., Beck, H., Trahan, N., Griffin, B., and Heckman, D. 2011. Land area change in coastal Louisiana from 1932 to 2010. U.S. Geological Survey Scientific Investigations Map 3164, Scale 1:265,000.

Da Lio, C., Teatini, P., Strozzi, T., and Tosi, L. 2018. Understanding land subsidence in salt marshes of the Venice Lagoon from SAR interferometry and ground-based investigations. *Remote Sensing of Environment*, 205, 56-70.

Day, J., Ibáñez, C., Scarton, F., Pont, D., Hensel, P., Day, J., and Lane, R. 2011. Sustainability of Mediterranean deltaic and lagoon wetlands with sea-level rise: The importance of river input. *Estuaries and Coasts*, 34, 483-493.

Deltares. 2018. D-Settlement embankment design and soil settlement prediction: User manual. Deltares, Delft, The Netherlands, 322 p.

De Mutsert, K., Lewis, K., Milroy, S., Buszowski, J., and Steenbeek, J. 2017. Using ecosystem modeling to evaluate trade-offs in coastal management: Effects of

large-scale river diversions on fish and fisheries. *Ecological Modelling* 360, 14-26.

Den Haan, E.J. and Kruse, G.A.M. 2007. Characterisation and engineering properties of Dutch peats. In: *Characterisation and Engineering Properties of Natural Soils, Volume 3: Proceedings of the Second International Workshop on Characterisation and Engineering Properties of Natural Soils, 29 November – 2 December 2006, Singapore*. Tan, T.S., Phoon, K.K., Hight, D.W., and Leroueil, S., eds. Taylor and Francis, New York, p. 2101-2134.

Dixon, T. H., Amelung, F., Ferretti, A., Novali, F., Rocca, F., Dokka, R., Sella, G., Kim, S.-W., Wdowinski, S., and Whitman, D. 2006. Subsidence and flooding in New Orleans. *Nature*, 441, 587-588.

Dokka, R. K., Sella, G. F., and Dixon, T. H. 2006. Tectonic control of subsidence and southward displacement of southeast Louisiana with respect to stable North America. *Geophysical Research Letters*, 33, L23308.

Donchyts, G., Baart, F., Winsemius, H., Gorelick, N., Kwadijk, J., and van de Giesen, N. 2016. Earth's surface water change over the past 30 years. *Nature Climate Change*, 6, 810-813.

Douglas, B. C. 1991. Global sea level rise. *Journal of Geophysical Research*, 96, 6981-6992.

- Draut, A.E., Kineke, G.C., Velasco, D.W., Allison, M.A., and Prime, R.J. 2005. Influence of the Atchafalaya River on recent evolution of the chenier-plain inner continental shelf, northern Gulf of Mexico. *Continental Shelf Research*, 25, 91-112.
- Erban, L.E., Gorelick, S.M., and Zebker, H.A. 2014. Groundwater extraction, land subsidence, and sea-level rise in the Mekong Delta, Vietnam. *Environmental Research Letters*, 9, 084010.
- Ericson, J. P., Vörösmarty, C. J., Dingman, S. L., Ward, L. G., and Meybeck, M. 2006. Effective sea-level rise and deltas: Causes of change and human dimension implications. *Global and Planetary Change*, 50, 63-82.
- Erkens, G., van der Meulen, M.J., and Middelkoop, H. 2016. Double trouble: subsidence and CO₂ respiration due to 1,000 years of Dutch coastal peatlands cultivation. *Hydrogeology Journal*, 24, 551-568.
- Esposito, C.R., Georgiou, I.Y., and Kolker, A.S. 2013. Hydrodynamic and geomorphic controls on mouth bar evolution. *Geophysical Research Letters*, 40, 1-6.
- Esposito, C.R., Shen, Z., Törnqvist, T.E., Marshak, J., and White, C. 2017. Efficient retention of mud drives land building on the Mississippi Delta plain. *Earth Surface Dynamics*, 5, 387-397.
- Fagherazzi, S., Kirwan, M.L., Mudd, S.M., Guntenspergen, G.R., Temmerman, S., D'Alpaos, A., van de Koppel, J., Rybczyk, J.M., Reyes, E., Craft, C., and Clough, J. 2012. Numerical models of salt marsh evolution: Ecological, geomorphic, and climatic factors. *Reviews of Geophysics*, 50, RG1002.

- Folse, T.M., Sharp, L.A., West, J.L., Hymel, M.K., Troutman, J.P., McGinnis, T.E., Weifenbach, D., Boshart, W.M., Rodrigue, L.B., Richardi, D.C., Wood, W.B., and Miller, C.M. 2014. A standard operating procedures manual for the coast-wide reference monitoring system – wetlands: Methods for site establishment, data collection, and quality assurance/quality control. Louisiana Coastal Protection and Restoration Authority, Office of Coastal Protection and Restoration, Baton Rouge, Louisiana, 228 p.
- Frazier, D.E. 1967. Recent deltaic deposits of the Mississippi River: Their development and chronology. *Transactions of Gulf Coast Association of Geological Societies*, 17, 287-315.
- Funabiki, A., Haruyama, S., Van Quy, N., Van Hai, P., and Thai, D. H. 2007. Holocene delta plain development in the Song Hong (Red River) delta, Vietnam. *Journal of Asian Earth Sciences*, 30, 518-529.
- Gebremichael, E., Sultan, M., Becker, R., El Bastawesy, M., Cherif, O., and Emil, M. 2018. Assessing land deformation and sea encroachment in the Nile Delta: A radar interferometric and inundation modeling approach. *Journal of Geophysical Research: Solid Earth*, 123, 3208-3224.
- Gedan, K.B., Kirwan, M.L., Wolanski, E., Barbier, E.B., and Silliman, B.R. 2011. The present and future role of coastal wetland vegetation in protecting shorelines: Answering recent challenges to the paradigm. *Climatic Change*, 106, 7-29.

- Giosan, L., Constantinescu, S., Filip, F., and Deng, B. 2013. Maintenance of large deltas through channelization: Nature vs. humans in the Danube delta. *Anthropocene*, 1, 35-45.
- Giosan, L., Syvitski, J., Constantinescu, S., and Day, J. 2014. Protect the world's deltas. *Nature*, 516, 31-33.
- Gleason, M.L., Elmer, D.A., and Pien, N.C. 1979. Effects of stem density upon sediment retention by salt marsh cord grass, *Spartina alterniflora* Loisel. *Estuaries*, 2, 271-273.
- Goodbred, S. L. and Kuehl, S. A. 2000. The significance of large sediment supply, active tectonism, and eustasy on margin sequence development: Late Quaternary stratigraphy and evolution of the Ganges–Brahmaputra delta. *Sedimentary Geology*, 133, 227-248.
- Gornitz, V., Lebedeff, S., and Hansen, J. 1982. Global sea level trend in the past century. *Science*, 215, 1611-1614.
- Harris, P. T., Baker, E. K., Cole, A. R., and Short, S. A. 1993. A preliminary study of sedimentation in the tidally dominated Fly River Delta, Gulf of Papua. *Continental Shelf Research*, 13, 441-472.
- Haslett, S.K., Davies, P., Curr, R.H.F., Davies, C.F.C., Kennington, K., King, C.P., and Margetts, A.J. 1998. Evaluating late-Holocene relative sea-level change in the Somerset Levels, southwest Britain. *The Holocene*, 8, 197-207.

- Hay, C. C., Morrow, E., Kopp, R. E., and Mitrovica, J. X. 2015. Probabilistic reanalysis of twentieth-century sea-level rise. *Nature*, 517, 481-484.
- Heinrich, P., Paulsell, R., Milner, R., Snead, J., and Peele, H. 2015. Investigation and GIS development of the buried Holocene-Pleistocene surface in the Louisiana coastal plain. Louisiana Geological Survey and Louisiana State University for the Coastal Protection and Restoration Authority of Louisiana. Baton Rouge, LA, USA, 140 pp.
- Higgins, S. A. 2016. Advances in delta-subsidence research using satellite methods. *Hydrogeology Journal*, 24, 587-600.
- Higgins, S.A., Overeem, I., Steckler, M.S., Syvitski, J.P.M., Seeber, L., and Akhter, S.H. 2014. InSAR measurements of compaction and subsidence in the Ganges-Brahmaputra Delta, Bangladesh. *Journal of Geophysical Research: Earth Surface*, 119, 1768-1781.
- Hijma, M.P., Cohen, K.M., Hoffmann, G., Van der Spek, A.J.F., and Stouthamer, E. 2009. From river valley to estuary: The evolution of the Rhine mouth in the early to middle Holocene (western Netherlands, Rhine-Meuse delta). *Netherlands Journal of Geosciences*, 88, 13-53.
- Holgate, S.J., Matthews, A., Woodworth, P.L., Rickards, L.J., Tamisiea, M.E., Bradshaw, E., Foden, P.R., Gordon, K.M., Jevrejeva, S., and Pugh, J. 2013. New data systems and products at the Permanent Service for Mean Sea Level. *Journal of Coastal Research*, 29, 493-504.

- Hook, P.B. 2003. Sediment retention in rangeland riparian buffers. *Journal of Environmental Quality* 32, 1130-1137.
- Hopkinson, C.S., Gosselink, J.G., and Parrando, R.T. 1978. Aboveground production of seven marsh plant species in coastal Louisiana. *Ecology* 59, 760-769.
- Hori, K., Usami, S., and Ueda, H. 2011. Sediment facies and Holocene deposition rate of near-coastal fluvial systems: An example from the Nobi Plain, Japan. *Journal of Asian Earth Sciences*, 41, 195-203.
- Jankowski, K.L. 2017. Implications of environmental change on wetland vulnerability and carbon sequestration in coastal Louisiana. PhD dissertation, Tulane University, 113 p.
- Jankowski, K.L., Törnqvist, T.E., and Fernandes, A.M. 2017. Vulnerability of Louisiana's coastal wetlands to present-day rates of relative sea-level rise. *Nature Communications*, 8, 14792.
- Jones, C. E., An, K., Blom, R. G., Kent, J. D., Ivins, E. R., and Bekaert, D. 2016. Anthropogenic and geologic influences on subsidence in the vicinity of New Orleans, Louisiana. *Journal of Geophysical Research: Solid Earth*, 121, 3867-3887.
- Kadlec, R.H. 1990. Overland flow in wetlands: Vegetation resistance. *Journal of Hydraulic Engineering*, 116, 691-706.

- Karegar, M. A., Dixon, T. H., and Malservisi, R. 2015. A three-dimensional surface velocity field for the Mississippi Delta: Implications for coastal restoration and flood potential. *Geology*, 43, 519-522.
- Kaye, C.A. and Barghoorn, E.S. 1964. Late Quaternary sea-level change and crustal rise at Boston, Massachusetts, with notes on the autocompaction of peat. *Geological Society of America Bulletin*, 75, 63-80.
- Keogh, M.E., Kolker, A.S., Snedden, G.A., and Renfro, A.A. 2019. Hydrodynamic controls on sediment retention in an emerging diversion-fed delta. *Geomorphology*, 332, 100-111.
- Keogh, M.E. and Törnqvist, T.E. 2019. Measuring rates of present-day relative sea-level rise in low-elevation coastal zones: a critical evaluation. *Ocean Science*, 15, 61-73.
- Kim, W., Mohrig, D., Twilley, R., Paola, C., and Parker, G. 2009. Is it feasible to build new land in the Mississippi River Delta? *Eos*, 90, 373-384.
- Kirwan, M.L., Temmerman, S., Skeeahan, E.E., Guntenspergen, G.R., and Fagherazzi, S. 2016. Overestimation of marsh vulnerability to sea level rise. *Nature Climate Change*, 6, 253-260.
- Kleiss, B.A. 1996. Sediment retention in a bottomland hardwood wetland in eastern Arkansas. *Wetlands*, 16, 321-333.

- Kolker, A.S., Goodbred, Jr., S.L., Hameed, S., and Cochran, J.K. 2009. High-resolution records of the response of coastal wetland systems to long-term and short-term sea-level variability. *Estuarine, Coastal, and Shelf Science*, 84, 493-508.
- Kolker, A.S., Allison, M.A., and Hameed, S. 2011. An evaluation of subsidence rates and sea-level variability in the northern Gulf of Mexico. *Geophysical Research Letters*, 38, L21404.
- Kolker, A.S., Miner, M.D., and Weathers, H.D. 2012. Depositional dynamics in a river diversion receiving basin: The case of the West Bay Mississippi River Diversion. *Estuarine, Coastal and Shelf Science*, 106, 1-12.
- Kolker, A.S. and Ameen, A.D. 2014. Stratigraphic development of crevasse splay islands in West Bay. Unpublished report, 16 p.
- Kopp, R. E., Horton, R. M., Little, C. M., Mitrovica, J. X., Oppenheimer, M., Rasmussen, D. J., Strauss, B. H., and Tebaldi, C. 2014. Probabilistic 21st and 22nd century sea-level projections at a global network of tide-gauge sites. *Earth's Future*, 2, 383-406.
- Koskiahho, J. 2003. Flow velocity retardation and sediment retention in two constructed wetland-ponds. *Ecological Engineering*, 19, 325-337.
- Koster, K., Cohen, K. M., Stafleu, J., and Stouthamer, E. 2018. Using ^{14}C -dated peat beds for reconstructing subsidence by compression in the Holland coastal plain of the Netherlands. *Journal of Coastal Research*, 34, 1035-1045.

- Kuecher, G.J., Chandra, N., Roberts, H.H., Suhayda, J.H., Williams, S.J., Penland, S.P., and Autin, W.J. 1993. Consolidation settlement potential in south Louisiana. Proceedings, 8th Symposium on Coastal and Ocean Management, New Orleans, 1197-1214.
- Larsen, C. E. 1975. The Mesopotamian Delta region: A reconsideration of Lees and Falcon. *Journal of the American Oriental Society*, 95, 43-57.
- Leonard, L.A. and Luther, M.E. 1995. Flow hydrodynamics in tidal marsh canopies. *Limnology Oceanography*, 40, 1474-1484.
- Leopold, L.B. 1994. *A View of the River*. Harvard University Press, Cambridge, Massachusetts, USA, 323 p.
- Li, C., Chen, Q., Zhang, J., Yang, S., and Fan, D. 2000. Stratigraphy and paleoenvironmental changes in the Yangtze Delta during the Late Quaternary. *Journal of Asian Earth Sciences*, 18, 453-469.
- Long, A.J., Waller, M.P., and Stupples, P. 2006. Driving mechanisms of coastal change: Peat compaction and the destruction of late Holocene coastal wetlands. *Marine Geology*, 225, 63-84.
- Lovelock, C.E., Cahoon, D.R., Friess, D.A., Guntenspergen, G.R., Krauss, K.W., Reef, R., Rogers, K., Saunders, M.L., Sidik, F., Swales, A., Saintilan, N., Thuyen, L.X., and Triet, T. 2015. The vulnerability of Indo-Pacific mangrove forests to sea-level rise. *Nature*, 526, 559-563.

- Marriner, N., Flaux, C., Morhange, C., and Kaniewski, D. 2012. Nile Delta's sinking past: Quantifiable links with Holocene compaction and climate-driven changes in sediment supply? *Geology*, 40, 1083-1086.
- Marsh, P., Lesack, L.F.W., and Roberts, A. 1999. Lake sedimentation in the Mackenzie Delta, NWT. *Hydrological Processes*, 13, 2519-2536.
- Mathers, S. and Zalasiewicz, J. 1999. Holocene sedimentary architecture of the Red River Delta. *Journal of Coastal Research*, 15, 314-325.
- Maul, G. A. and Martin, D. M. 1993. Sea level rise at Key West, Florida, 1846-1992: America's longest instrument record? *Geophysical Research Letters*, 20, 1955-1958.
- Mazzotti, S., Lambert, A., Van der Kooij, M., and Mainville, A. 2009. Impact of anthropogenic subsidence on relative sea-level rise in the Fraser River delta. *Geology*, 37, 771-774.
- McAlpin, T.O., Letter, Jr., J.V., and Martin, S.K. 2008. A hydrodynamic study of Davis Pond, near New Orleans, LA. Coastal and Hydraulics Laboratory, U.S. Army Engineer Research and Development Center Report ERDC/CHL TR-08-11, 108 p.
- Meade, R.H. and Moody, J.A. 2010. Causes for the decline of suspended-sediment discharge in the Mississippi River system, 1940-2007. *Hydrological Processes*, 24, 35-49.

- Miller, R.L., Fram, M.S., Fujii, R., and Wheeler, G. 2008. Subsidence reversal in a re-established wetland in the Sacramento-San Joaquin Delta, California, USA. *San Francisco Estuary and Watershed Science*, 6, 20 p.
- Minderhoud, P.S.J., Erkens, G., Pham, V.H., Bui, V.T., Erban, L., Kooi, H., and Stouthamer, E. 2017. Impacts of 25 years of groundwater extraction on subsidence in the Mekong delta, Vietnam. *Environmental Research Letters*, 12, 064006.
- Minderhoud, P.S.J., Coumou, L., Erban, L.E., Middelkoop, H., Stouthamer, E., and Addink, E.A. 2018. The relationship between land use and subsidence in the Vietnamese Mekong delta. *Science of the Total Environment*, 634, 715-726.
- Mojski, J. E. 1995. Geology and evolution of the Vistula Delta and Vistula Bar. *Journal of Coastal Research, Special Issue*, 22, 141-149.
- Morris, J.T., Barber, D.C., Callaway, J.C., Chambers, R., Hagen, S.C., Hopkinson, C.S., Johnson, B.J., Megonigal, P., Neubauer, S.C., Troxler, T., and Wigand, C. 2016. Contributions of organic and inorganic matter to sediment volume and accretion in tidal wetlands at steady state. *Earth's Future*, 4, 110-121.
- Mossa, J. 1996. Sediment dynamics in the lowermost Mississippi River. *Engineering Geology*, 45, 457-479.
- Nardin, W. and Edmonds, D.A. 2014. Optimum vegetation height and density for inorganic sedimentation in deltaic marshes. *Nature Geoscience*, 7, 722-726.

- National Oceanic and Atmospheric Administration (NOAA). 2013. CO-OPS specifications and deliverables for installation, operation, and removal of water level stations, Center for Operational Oceanographic Products and Services, Engineering Division, National Ocean Service, Silver Spring, MD, USA, 30 pp.
- Netherlands Standardization Institute (NEN). 2006. NEN 6740: Geotechnics - TGB 1990 - Basic requirements and loads. Publisher NEN, 98 pp.
- Neubauer, S.C. 2008. Contributions of mineral and organic components to tidal freshwater marsh accretion. *Estuarine, Coastal, and Shelf Science*, 78, 78-88.
- Neumann, B., Vafeidis, A.T., Zimmermann, J., and Nicholls, R.J. 2015. Future coastal population growth and exposure to sea-level rise and coastal flooding – A global assessment. *PLoS ONE*, 10, e0118571.
- Neumeier, U. and Ciavola, P. 2004. Flow resistance and associated sedimentary processes in a *Spartina maritima* salt-marsh. *Journal of Coastal Research*, 20, 435-447.
- Nicholls, R. J. and Cazenave, A. 2010. Sea-level rise and its impact on coastal zones. *Science*, 328, 1517-1520.
- Nienhuis, J.H., Törnqvist, T.E., Jankowski, K.L., Fernandes, A.M., and Keogh, M.E. 2017. A new subsidence map for coastal Louisiana. *GSA Today*, 27 (9), 58-59.

- Nienhuis, J.H., Törnqvist, T.E., and Esposito, C.R. 2018. Crevasse splays versus avulsions: A recipe for land building with levee breaches. *Geophysical Research Letters*, 45, 4058-4067.
- Nittrouer, C.A., Kuehl, S.A., Sternberg, R.W., Figueiredo, Jr., A.G., and Faria, L.E.C. 1995. An introduction to the geological significance of sediment transport and accumulation on the Amazon continental shelf. *Marine Geology*, 125, 177-192.
- Nummedal, D. 1983. Future sea level changes along the Louisiana coast. *Shore and Beach*, 51 (2), 10-15.
- Nyman, J.A., Delaune, R.D., and Patrick., Jr., W.H. 1990. Wetland soil formation in the rapidly subsiding Mississippi River Deltaic Plain: Mineral and organic matter relationships. *Estuarine, Coastal and Shelf Science*, 31, 57-69.
- Nyman, J.A., Walters, R.J., Delaune, R.D., and Patrick, Jr., W.H. 2006. Marsh vertical accretion via vegetative growth. *Estuarine, Coastal and Shelf Science*, 69, 370-380.
- Osland, M.J., Griffith, K.T., Larriviere, J.C., Feher, L.C., Cahoon, D.R., Enwright, N.M., Oster, D.A., Tirpak, J.M., Woodrey, M.S., Collini, R.C., Baustian, J.J., Breithaupt, J.L., Cherry, J.A., Conrad, J.R., Cormier, N., Coronado-Molina, C.A., Donoghue, J.F., Graham, S.A., Harper, J.W., Hester, M.W., Howard, R.J., Krauss, K.W., Kroes, D.E., Lane, R.R., McKee1, K.L., Mendelssohn, I.A., Middleton, B.A., Moon, J.A., Piazza, S.C., Rankin, N.M., Sklar, F.H., Steyer, G.D., Swanson, K.M., Swarzenski, C.M., Vervaeke, W.C., Willis, J.M., and Van Wilson, K. 2017.

Assessing coastal wetland vulnerability to sea-level rise along the northern Gulf of Mexico coast: Gaps and opportunities for developing a coordinated regional sampling network. *PLoS ONE*, 12, e0183431.

Paola, C., Twilley, R.R., Edmonds, D.A., Kim, W., Mohrig, D., Parker, G., Viparelli, E., and Voller, V.R. 2011. Natural processes in delta restoration: Application to the Mississippi Delta. *Annual Review of Marine Science*, 3, 67-91.

Penland, S. and Ramsey, K. E. 1990. Relative sea-level rise in Louisiana and the Gulf of Mexico: 1908-1988, *Journal of Coastal Research*, 6, 323-342.

Peyronnin, N.S., Caffey, R.H., Cowan, Jr., J.H., Justic, D., Kolker, A.S., Laska, S.B., McCorquodale, A., Melancon, Jr., E., Nyman, J.A., Twilley, R.R., Visser, J.M., White, J.R., and Wilkins, J.G. 2017. Optimizing sediment diversion operations: Working group recommendations for integrating complex ecological and social landscape interactions. *Water*, 9, 368.

Pfeffer, J. and Allemand, P. 2016. The key role of vertical land motions in coastal sea level variations: A global synthesis of multisatellite altimetry, tide gauge data and GPS measurements. *Earth and Planetary Science Letters*, 439, 39-47.

Phien-wej, N., Giao, P.H., and Nutalaya, P. 2006. Land subsidence in Bangkok, Thailand. *Engineering Geology*, 82, 187-201.

Pugh, D. T. 1987. *Tides, Surges, and Mean Sea-Level*. John Wiley and Sons, New York, NY, USA, 472 pp.

- Redfield, A.C. 1972. Development of a New England salt marsh. *Ecological Monographs*, 42, 201-237.
- Reed, D.J., Beall, A., Martinez, L., Minello, T.J., Uzee O'Connell, A.M., Rozas, L.P., Penland, S., Cashner, R.C., and Commagere, A.M. 2007. Modeling relationships between the abundance of fishery species, coastal wetland landscapes, and salinity in the Barataria Basin, Louisiana. University of New Orleans and NOAA National Marine Fisheries Service Report, 160 p.
- Restrepo, J.D. and Kettner, A. 2012. Human induced discharge diversion in a tropical delta and its environmental implications: The Patía River, Colombia. *Journal of Hydrology*, 424-425, 124-142.
- Richardson, C.J., Reiss, P., Hussain, N.A., Alwash, A.J., and Pool, D.J. 2005. The restoration potential of the Mesopotamian marshes of Iraq. *Science*, 307, 1307-1311.
- Rieke, H.H. and Chilingarian, G.V. 1974. *Compaction of Argillaceous Sediments: Developments in Sedimentology*, 16. Elsevier, Amsterdam, 423 p.
- Roberts, H.H. 1997. Dynamic changes of the Holocene Mississippi River delta plain: The delta cycle. *Journal of Coastal Research*, 13, 605-627.
- Roberts, H.H., Coleman, J.M., Bentley, S.J., and Walker, N. 2003. An embryonic major delta lobe: A new generation of delta studies in the Atchafalaya-Wax Lake Delta system. *Transactions of Gulf Coast Association of Geological Societies*, 53, 690-703.

- Roberts, H.H., DeLaune, R.D., White, J.R., Li, C., Sasser, C.E., Braud, D., Weeks, E., and Khalil, S. 2015. Floods and cold front passages: Impacts on coastal marshes in a river diversion setting (Wax Lake Delta area, Louisiana). *Journal of Coastal Research*, 31, 1057-1068.
- Rosen, T. and Xu, Y.J. 2013. Recent decadal growth of the Atchafalaya River Delta complex: Effects of variable riverine sediment input and vegetation succession. *Geomorphology*, 194, 108-120.
- Rosenheim, B.E., Roe, K.M., Roberts, B.J., Kolker, A.S., Allison, M.A., and Johannesson, K.H. 2013. River discharge influences on particulate organic carbon age structure in the Mississippi/Atchafalaya River System. *Global Biogeochemical Cycles*, 27, 1-13.
- San Francisco Estuary Institute – Aquatic Science Center (SFEI-ASC). 2016. A delta renewed: A guide to science-based ecological restoration in the Sacramento-San Joaquin Delta. Prepared for the California Department of Fish and Wildlife and Ecosystem Restoration Program. A Report of SFEI-ASC's Resilient Landscapes Program, Publication 799, Richmond, CA, 164 p.
- Shaw, J.B. and Mohrig, D. 2014. The importance of erosion in distributary channel network growth, Wax Lake Delta, Louisiana, USA. *Geology*, 42, 31-34.
- Shaw, J.B., Miller, K., and McElroy, B. 2018. Island formation resulting from radially symmetric flow expansion. *Journal of Geophysical Research: Earth Surface*, 123, 363-383.

- Shen, Z., Törnqvist, T.E., Mauz, B., Chamberlain, E.L., Nijhuis, A.G., and Sandoval, L. 2015. Episodic overbank deposition as a dominant mechanism of floodplain and delta-plain aggradation. *Geology*, 43, 875-878.
- Shennan, I. and Woodworth, P. L. 1992. A comparison of late Holocene and twentieth-century sea-level trends from the UK and North Sea region. *Geophysical Journal International*, 109, 96-105.
- Shi, X., Wu, J., Ye, S., Zhang, Y., Xue, Y., Wei, Z., Li, Q., and Yu, J. 2008. Regional land subsidence simulation in Su-Xi-Chang area and Shanghai City, China. *Engineering Geology*, 100, 27-42.
- Sibson, R. 1981. A brief description of natural neighbor interpolation. In: Barnett, V. (Ed.), *Interpreting Multivariate Data*. Wiley, New York, pp. 21-36.
- Snedden, G.A., Cable, J.E., Swarzenski, C., and Swenson, E. 2007. Sediment discharge into a subsiding Louisiana deltaic estuary through a Mississippi River diversion. *Estuarine, Coastal, and Shelf Science*, 71, 181-193.
- Snedden, G.A., Cretini, K., and Patton, B. 2015. Inundation and salinity impacts to above- and belowground productivity in *Spartina patens* and *Spartina alterniflora* in the Mississippi River deltaic plain: Implications for using river diversions as restoration tools. *Ecological Engineering*, 81, 133-139.
- Sommerfield, C.K., Nittrouer, C.A., and Alexander, C.R. 1999. ^7Be as a tracer of flood sedimentation on the northern California continental margin. *Continental Shelf Research*, 19, 335-361.

- Stanley, D.J. and Warne, A.G. 1993. Nile delta: Recent geological evolution and human impact. *Science*, 260, 628-634.
- Stevenson, J.C., Ward, L.G., and Kearney, M.S. 1988. Sediment transport and trapping in marsh systems: Implications of tidal flux studies. *Marine Geology*, 80, 37-59.
- Suarez, B.E.S. 2004. The Sinú River Delta on the northwestern Caribbean coast of Colombia: Bay infilling associated with delta development. *Journal of South American Earth Sciences*, 16, 623-631.
- Swanson, R. L. and Thurlow, C. I. 1973. Recent subsidence rates along the Texas and Louisiana coasts as determined from tide measurements. *Journal of Geophysical Research*, 78, 2665-2671.
- Syvitski, J.P.M., Vörösmarty, C.J., Kettner, A.J., and Green, P. 2005. Impact of humans on the flux of terrestrial sediment to the global coastal ocean. *Science*, 308, 376-380.
- Syvitski, J.P.M. and Saito, Y. 2007. Morphodynamics of deltas under the influence of humans. *Global and Planetary Change*, 57, 261-282.
- Syvitski, J. P. M., Kettner, A. J., Overeem, I., Hutton, E. W. H., Hannon, M. T., Brakenridge, G. R., Day, J., Vörösmarty, C., Saito, Y., Giosan, L., and Nicholls, R. J. 2009. Sinking deltas due to human activities. *Nature Geoscience*, 2, 681-686.

- Ta, T.K.O., Nguyen, V.L., Tateishi, M., Kobayashi, I., Tanabe, S., and Saito, Y. 2002. Holocene delta evolution and sediment discharge of the Mekong River, southern Vietnam. *Quaternary Science Reviews*, 21, 1807-1819.
- Talke, S. A., Kemp, A. C., and Woodruff, J. 2018. Relative sea level, tides, and extreme water levels in Boston Harbor from 1825 to 2018. *Journal of Geophysical Research: Oceans*, 123, 3895-3914.
- Tanabe, S., Saito, Y., Sato, Y., Suzuki, Y., Sinsakul, S., Tiypairach, S., and Chaimanee, N. 2003a. Stratigraphy and Holocene evolution of the mud-dominated Chao Phraya delta, Thailand. *Quaternary Science Reviews*, 22, 789-807.
- Tanabe, S., Ta, T. K. O., Nguyen, V. L., Tateishi, M., Kobayashi, I., and Saito, Y. 2003b. Delta evolution model inferred from the Holocene Mekong delta, southern Vietnam. *SEPM (Society for Sedimentary Geology) Special Publication*, 76, 175-188.
- Tanabe, S., Nakanishi, T., Ishihara, Y., and Nakashima, R. 2015. Millennial-scale stratigraphy of a tide-dominated incised valley during the last 14 kyr: Spatial and quantitative reconstruction in the Tokyo Lowland, central Japan. *Sedimentology*, 62, 1837-1872.
- Teatini, P., Tosi, L., Strozzi, T., Carbognin, L., Wegmüller, U., and Rizzetto, F. 2005. Mapping regional land displacements in the Venice coastland by an integrated monitoring system. *Remote Sensing of Environment*, 98, 403-413.

- Tessler, Z. D., Vörösmarty, C. J., Grossberg, M., Gladkova, I., Aizenman, H., Syvitski, J. P. M., and Foufoula-Georgiou, E. 2015. Profiling risk and sustainability in coastal deltas of the world. *Science*, 349, 638-643.
- Törnqvist, T.E., Paola, C., Parker, G., Liu, K., Mohrig, D., Holbrook, J.M., and Twilley, R.R. 2007. Comment on “Wetland sedimentation from Hurricanes Katrina and Rita”. *Science*, 316, 201b.
- Törnqvist, T.E., Wallace, D.J., Storms, J.E.A., Wallinga, J., Van Dam, R.L., Blaauw, M., Derksen, M.S., Klerks, C.J.W., Meijneken, C., and Snijders, E.M.A. 2008. Mississippi Delta subsidence primarily caused by compaction of Holocene strata. *Nature Geoscience*, 1, 173-176.
- Turner, R.E. 1997. Wetland loss in the Northern Gulf of Mexico: Multiple working hypotheses. *Estuaries*, 20, 1-13.
- Turner, R.E., Swenson, E.M., and Milan, C.S. 2002. Organic and inorganic contributions to vertical accretion in salt marsh sediments. In: M.P. Weinstein and D.A. Kreeger, eds., *Concepts and Controversies in Tidal Marsh Ecology*. Kluwer Academic Publishers, New York, p. 583-595.
- Turner, R.E., Milan, C.S., and Swenson, E.M. 2006. Recent volumetric changes in salt marsh soils. *Estuarine, Coastal, and Shelf Science*, 69, 352-359.
- U.S. Geological Survey (USGS). 2018a. USGS Current Conditions for USGS 295501090190400 Davis Pond Freshwater Diversion near Boutte, LA. Available at:

https://waterdata.usgs.gov/la/nwis/uv/?site_no=295501090190400&PARAMeter_cd=00065,72020,63160,00060.

U.S. Geological Survey (USGS). 2018b. USGS Current Conditions for USGS 07374525 Mississippi River at Belle Chasse, LA. Available at:

https://waterdata.usgs.gov/la/nwis/uv/?site_no=07374525&PARAMeter_cd=00065,72020,63160,00060.

Van Asselen, S. 2011. The contribution of peat compaction to total basin subsidence: Implications for the provision of accommodation space in organic-rich deltas. *Basin Research*, 23, 239-255.

Van Asselen, S., Stouthamer, E., and Van Asch, T.W.J. 2009. Effects of peat compaction on delta evolution: A review on processes, responses, measuring and modeling. *Earth-Science Reviews*, 92, 35-51.

Van Asselen, S., Stouthamer, E., and Smith, N.D. 2010. Factors controlling peat compaction in alluvial floodplains: A case study in the cold-temperate Cumberland Marshes, Canada. *Journal of Sedimentary Research*, 80, 155-166.

Van Asselen, S., Karssenberg, D., and Stouthamer, E. 2011. Contribution of peat compaction to relative sea-level rise within Holocene deltas. *Geophysical Research Letters*, 38, L24401.

Van Asselen, S., Erkens, G., Stouthamer, E., Woolderink, H.A.G., Geeraert, R.E.E., and Hefting, M.M. 2018. The relative contribution of peat compaction and oxidation

to subsidence in built-up areas in the Rhine-Meuse delta, The Netherlands.

Science of the Total Environment, 636, 177-191.

Van Staveren, M.F., Warner, J.F., and Shah Alam Kahn, M. 2017. Bringing in the tides: From closing down to opening up delta polders via tidal river management in the southwest delta of Bangladesh. Water Policy, 19, 147-164.

Veatch, W. 2015. Updated atlas of U.S. Army Corps of Engineers historic daily tide data in coastal Louisiana. U.S. Army Corps of Engineers, New Orleans District, New Orleans, LA, USA, Mississippi River Geomorphology and Potamology Program Report 14, 40 pp. 2017.

Vignudelli, S., Kostianoy, A. G., Cipollini, P., and Benveniste, J. (Eds.). 2011. Coastal Altimetry. Springer, Berlin, Germany, 578 pp.

Vörösmarty, C.J., Meybeck, M., Fekete, B., Sharma, K., Green, P., and Syvitski, J.P.M. 2003. Anthropogenic sediment retention: major global impact from registered river impoundments. Global and Planetary Change, 39, 169-190.

Vos, P. C., Bazelmans, J., Weerts, H. J. T., and Van der Meulen, M. J. (Eds.). 2011. Atlas van Nederland in het Holoceen. Bert Bakker, Amsterdam, The Netherlands, 94 pp.

Wang, H., Piazza, S.C., Sharp, L.A., Stagg, C.L., Couvillion, B.R., Steyer, G.D., and McGinnis, T.E. 2017. Determining the spatial variability of wetland soil bulk density, organic matter, and the conversion factor between organic matter and

organic carbon across Coastal Louisiana, U.S.A. *Journal of Coastal Research*, 33, 507-517.

Webb, E. L., Friess, D. A., Krauss, K. W., Cahoon, D. R., Guntenspergen, G. R., and Phelps, J. 2013. A global standard for monitoring coastal wetland vulnerability to accelerated sea-level rise. *Nature Climate Change*, 3, 458-465.

Wheelock, K. 2003. Pulsed river flooding effects on sediment deposition in Breton Sound estuary, Louisiana. Master's thesis, Louisiana State University. Retrieved from Louisiana State University's electronic thesis and dissertation collection: http://etd.lsu.edu/docs/available/etd-0404103-084700/unrestricted/Wheelock_thesis.pdf. Accessed 12 July 2017.

Woodroffe, C. D., Curtis, R. J., and McLean, R. F. 1983. Development of a chenier plain, Firth of Thames, New Zealand. *Marine Geology*, 53, 1-22.

Woodworth, P. L., Menéndez, M., and Gehrels, W. R. 2011. Evidence for century-timescale acceleration in mean sea levels and for recent changes in extreme sea levels. *Surveys in Geophysics*, 32, 603-618.

Wöppelmann, G., Letetrel, C., Santamaria, A., Bouin, M.-N., Collilieux, X., Altamimi, Z., Williams, S. D. P., and Martín Míguez, B. 2009. Rates of sea-level change over the past century in a geocentric reference frame. *Geophysical Research Letters*, 36, L12607.

Wöppelmann, G. and Marcos, M. 2016. Vertical land motion as a key to understanding sea level change and variability. *Reviews of Geophysics*, 54, 64-92.

- Wright, L.D. 1977. Sediment transport and deposition at river mouths: A synthesis. Geological Society of America Bulletin, 88, 857-868.
- Xue, C. 1993. Historical changes in the Yellow River delta, China. Marine Geology, 113, 321-329.
- Yang, Y. and Aplin, A.C. 2004. Definition and practical application of mudstone porosity-effective stress relationships. Petroleum Geoscience, 10, 153-162.
- Yang, S.L., Zhang, J., Zhu, J., Smith, J.P., Dai, S.B., Gao, A., and Li, P. 2005. Impact of dams on Yangtze River sediment supply to the sea and delta intertidal wetland response. Journal of Geophysical Research, 110, F03006.
- Yang, Z., Wang, H., Saito, Y., Milliman, J.D., Xu, K., Qiao, S., and Shi, G. 2006. Dam impacts on the Changjiang (Yangtze) River sediment discharge to the sea: The past 55 years and after the Three Gorges Dam. Water Resources Research, 42, W04407.
- Yi, S., Saito, Y., Oshima, H., Zhou, Y., and Wei, H. 2003. Holocene environmental history inferred from pollen assemblages in the Huanghe (Yellow River) delta, China: climatic change and human impact. Quaternary Science Reviews, 22, 609-628.
- Zecchin, M., Brancolini, G., Tosi, L., Rizzetto, F., Caffau, M., and Baradello, L. 2009. Anatomy of the Holocene succession of the southern Venice lagoon revealed by very high-resolution seismic data. Continental Shelf Research, 29, 1343-1359.

Zhang, J.Z., Huang, H., and Bi, H. 2015. Land subsidence in the modern Yellow River Delta based on InSAR time series analysis. *Natural Hazards*, 75, 2385-2397.

Zoccarato, C. and Teatini, P. 2017. Numerical simulations of Holocene salt-marsh dynamics under the hypothesis of large soil deformations. *Advances in Water Resources*, 110, 107-119.

Zoccarato, C., Minderhoud, P.S.J., and Teatini, P. 2018. The role of sedimentation and natural compaction in a prograding delta: insights from the mega Mekong delta, Vietnam. *Scientific Reports*, 8, 11437.

APPENDICES

APPENDIX I

1. Correcting calculated values of bulk density

Two primary methods exist for measuring the dry bulk density of sediment. In the first method, bulk density (ρ_d) is directly measured using a sampler with a known volume (V) and using the following equation:

$$\rho_d = V / m \quad (\text{A1.1})$$

where m is the mass of the sample. This method was used for sediment samples in the CRMS, Upper Lafourche, and Myrtle Grove I cores.

The second method of calculating dry bulk density uses measurements of LOI and assumed densities of mineral and organic matter (Adams 1973; Kolker et al. 2009; Morris et al. 2016). Bulk density is calculated as

$$\rho_d = 1 - W / [(W / \rho_w) + ((1 - W) / \rho_s)] \quad (\text{A1.2})$$

where W is the water mass (expressed as a fraction), ρ_w is the density of water (assumed to be 1.02 g cm^{-3}), and ρ_s is the density of sediment and is calculated as

$$\rho_s = (1 - \text{LOI} \times 2.6) + (\text{LOI} \times 1.2) \quad (\text{A1.3})$$

where 2.6 and 1.2 g cm^{-3} are the assumed densities of mineral and organic matter, respectively. This method was used for samples in the Davis Pond and West Bay cores.

Based on comparisons of these two methods using data from the Upper Lafourche and Myrtle Grove I cores (Figures A1.1-A1.4), a best-fit correction factor of 1.75 was applied to all Davis Pond and West Bay bulk density values.

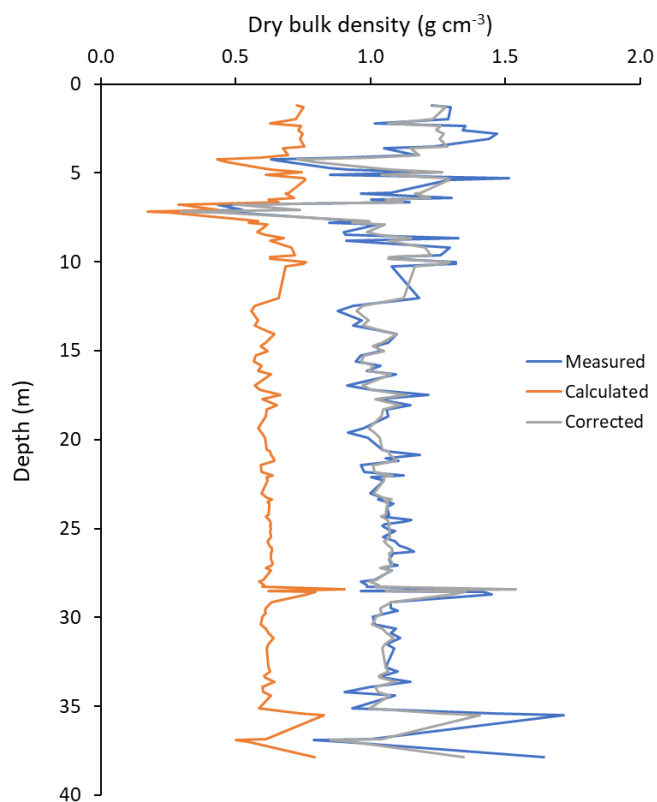


Figure A1.1. Comparison of two methods of measuring bulk density using data from the Myrtle Grove I core. The blue curve represents the measured (true) bulk densities. The orange curve represents the calculated bulk densities. The calculated values have been corrected to match the measured values using a correction factor of 1.70 (grey curve).

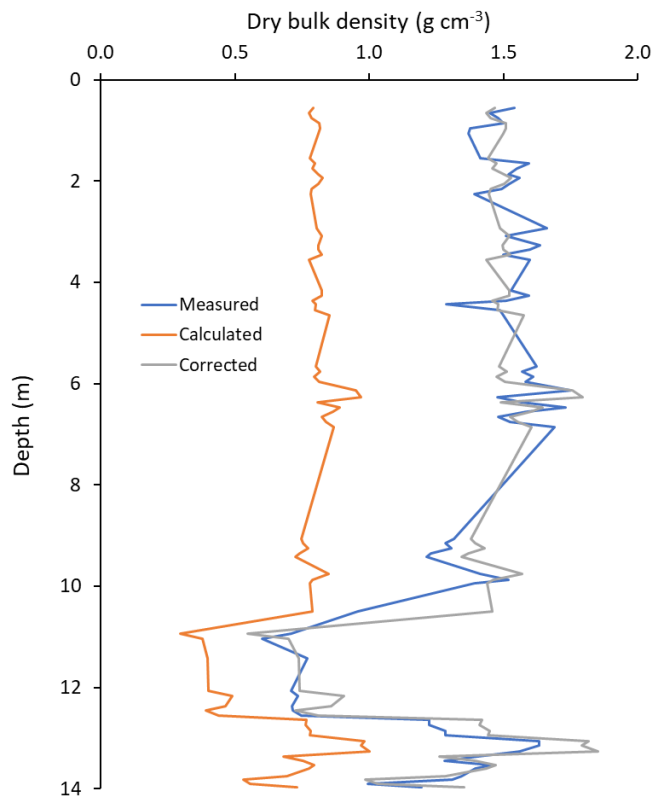


Figure A1.2. Comparison of two methods of measuring bulk density using data from the Napoleonville II core. The blue curve represents the measured (true) bulk densities. The orange curve represents the calculated bulk densities. The calculated values have been corrected to match the measured values using a correction factor of 1.85 (grey curve).

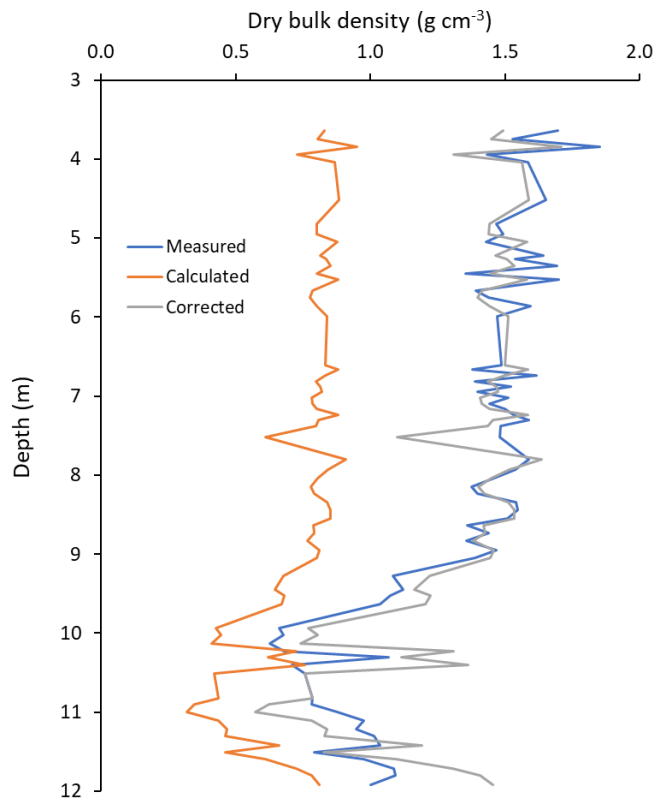


Figure A1.3. Comparison of two methods of measuring bulk density using data from the Paincourtville I core. The blue curve represents the measured (true) bulk densities. The orange curve represents the calculated bulk densities. The calculated values have been corrected to match the measured values using a correction factor of 1.80 (grey curve).

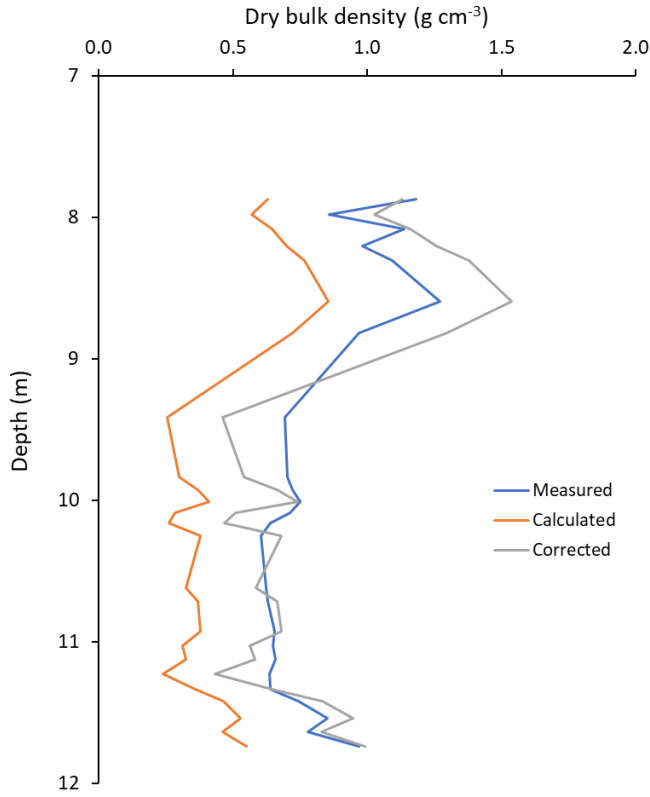


Figure A1.4. Comparison of two methods of measuring bulk density using data from the Napoleonville IV core. The blue curve represents the measured (true) bulk densities. The orange curve represents the calculated bulk densities. The calculated values have been corrected to match the measured values using a correction factor of 1.80 (grey curve).

2. Calculation of effective stress

For each sediment sample interval, we calculated effective stress following the steps outlined in the supplementary material to Van Asselen et al. (2018).

To begin, the mass density (ρ_m , g cm^{-3}) of is calculated using the following equation:

$$\rho_m = 1 / [(f_{\text{org}} / 1.47) + (f_{\text{clast}} \times f_{\text{clay}} / 2.70) + (f_{\text{clast}} \times f_{\text{silt}} / 2.65) + (f_{\text{clast}} \times f_{\text{sand}} / 2.65)] \quad (\text{A1.4})$$

where f_{org} is the fraction of organic matter determined from measurements of loss on ignition (LOI; $f_{\text{org}} = \text{LOI}/100$) and f_{clast} is the fraction of clastic material ($f_{\text{clast}} = 1 - f_{\text{org}}$). The variables f_{clay} , f_{silt} , and f_{sand} refer to the fraction of clay, silt, and sand that make up the clastic material. The specific gravities of organic matter, clay, silt, and sand are assumed to be 1.47, 2.70, 2.65, and 2.65 g cm^{-3} , respectively.

Pore volume (ϕ , dimensionless) is then calculated as

$$\phi = 1 - (\rho_d / \rho_m) \quad (\text{A1.5})$$

where ρ_d is the measured dry bulk density (g cm^{-3}).

The unit weight of the sediment (γ_{sed} , kN m^{-3}) is calculated as

$$\gamma_{\text{sed}} = [(\rho_d \times 1000) + (S \times \phi \times \rho_w)] \times (\gamma_{\text{water}} / 1000) \quad (\text{A1.6})$$

where S is the saturation of the sediment, which is assumed to be 0.98, ρ_w is the density of water, which equals 1000 kg m^{-3} , and γ_{water} is the unit weight of water, which equals 9.81 kN m^{-3} .

Total stress (σ , kN m^{-2}) and pore water pressure (μ , kN m^{-2}) are calculated as

$$\sigma = h \times \gamma_{\text{sed}} \quad (\text{A1.7})$$

and

$$\mu = h \times \gamma_{\text{water}} \quad (\text{A1.8})$$

respectively, where h is the thickness of the overlying column of sediment (m).

Finally, effective stress (σ' , kN m^{-2}) is calculated as

$$\sigma' = \sigma - \mu \quad (\text{A1.9})$$

3. Geotechnical parameters used for compaction modeling

Table A1.1. Values for the reloading/swelling ratio (RR), compression ratio (CR), and coefficient of secondary compaction (Ca) based on sediment type (Netherlands Standardization Institute, 2006).

Consistency			RR		CR		Ca	
sand	pure	weak	0.0038		0.0115		0	
		moderately stiff	0.0013		0.0038		0	
		stiff	0.0008	0.0005	0.0023	0.0015	0	
	weakly silty		0.0017	0.0012	0.0051	0.0035	0	
	silty		0.0038	0.0019	0.0115	0.0058	0	
loam	weakly sandy	weak	0.0307		0.0920		0.0037	
		moderately stiff	0.0170		0.0511		0.0020	
		stiff	0.0110	0.0077	0.0329	0.0230	0.0013	0.0009
	sandy		0.0170	0.0110	0.0511	0.0329	0.0020	0.0013
clay	pure	weak	0.1095		0.3286		0.0131	
		moderately stiff	0.0511		0.1533		0.0061	
		stiff	0.0307	0.0256	0.0920	0.0767	0.0037	0.0031
	weakly sandy	weak	0.0767		0.2300		0.0092	
		moderately stiff	0.0383		0.1150		0.0046	
		stiff	0.0256	0.0153	0.0767	0.0460	0.0031	0.0018
	sandy		0.0307	0.0055	0.0920	0.0164	0.0037	0.0007
	organic	weak	0.1022		0.3067		0.0153	
		moderately stiff	0.0767	0.0511	0.2300	0.1533	0.0115	0.0077
peat	no loading	weak	0.1533	0.1022	0.4600	0.3067	0.0230	0.0153
	moderate loading	moderately stiff	0.1022	0.0767	0.3067	0.2300	0.0153	0.0115

APPENDIX II

Table A2.1. Information on 131 tide gauges in coastal Louisiana. Note that several tide gauges have no published benchmarks; in this case, the benchmark setting type and foundation depth are left blank. Other tide gauges have benchmarks with unknown foundations depths. Unknown foundation depth should not be interpreted as foundation depth = 0.

Tide Gauge Name	Station Number	Agency	Website	Latitude (N)	Longitude (E)	Record start date	Record end date	Years active	Number of published benchmarks	Benchmark setting type(s)	Benchmark foundation depths (m)	Depth of deepest known benchmark foundation (m)	Depth of shallowest known benchmark foundation (m)	Depth of primary benchmark foundation (m)	Depth to reference surface (m)	Minimum benchmark foundation height above reference surface (m)
Amerasia Pass	8764227	NOAA	https://tidesandcurrents.noaa.gov/stationhome.html?id=8764227	29.4500	-91.3883	11/1/2005	10/22/2018	12.97	9	steel rod, concrete foundation	23.23, 23.23, 27.4, 27.4, 27.4	27.4	23	23	21	Set in Pleistocene
Bay Gardens	8761108	NOAA	https://tidesandcurrents.noaa.gov/stationhome.html?id=8761108	29.5983	-89.6183	10/16/1980	7/12/1988	7.74	5	steel rod	19.5, 19.5, 19.5, 19.5, 23.2	23.2	19.5	19.5	43	20
Bay Rambo, Teacoo Dock	8761962	NOAA	https://tidesandcurrents.noaa.gov/stationhome.html?id=8761962	29.3617	-90.1400	10/29/1986	2/8/1988	1.28	5	steel rod	24.4, 24.4, 24.4, 24.4, 24.4	24.4	24.4	24.4	54	30
Bayou St. Denis, I.V. Petroleum Dock	8761799	NOAA	https://tidesandcurrents.noaa.gov/stationhome.html?id=8761799	29.4967	-90.0250	7/17/1985	9/4/1986	1.13	5	steel rod	19.5, 21.9, 20.7, 23.2, 21.9	23.2	19.5	19.5	44	21
Billet Bay	8761414	NOAA	https://tidesandcurrents.noaa.gov/stationhome.html?id=8761414	29.3717	-89.7517	7/20/1985	11/4/1986	1.29	5	steel rod	20.7, 21.9, 21.9, 21.9, 20.7	21.9	20.7	20.7	52	30
Breton Island	8760595	NOAA	https://tidesandcurrents.noaa.gov/stationhome.html?id=8760595	29.4933	-89.1733	3/17/1980	11/1/1980	0.63	6	steel rod, concrete monument	15.2, 16.8, 18.3	18.3	15.2	15.2	70	52
Calcasieu Pass	8768094	NOAA	https://tidesandcurrents.noaa.gov/stationhome.html?id=8768094	29.7683	-93.3433	8/11/2002	10/22/2018	16.20	5	steel rod, concrete fishing pier, large boulder, davit plate	25, 24	25	24	25	18	Set in Pleistocene
Caminada Pass	8761826	NOAA	https://tidesandcurrents.noaa.gov/stationhome.html?id=8761826	29.2100	-90.0400	10/27/1986	2/2/1988	1.27	6	steel rod, retaining wall	21.9, 15.8, 18.3, 18.3, 17.1	21.9	15.8	15.8	55	33
Chef Menteur Pass	8761487	NOAA	https://tidesandcurrents.noaa.gov/stationhome.html?id=8761487	30.0650	-89.8000	11/25/1982	1/2/1991	8.10	6	steel rod, concrete bridge	23.1, 9.1, 39.5, 35.1, 21.9	35.1	9.1	23	13	Set in Pleistocene
Crocodile	8762928	NOAA	https://tidesandcurrents.noaa.gov/stationhome.html?id=8762928	29.2450	-90.6617	1/1/1997	1/1/2000	3.00	0		16.8, 16.8, 16.8, 16.8, 16.8	16.8	16.8	16.8	38	21
Comfort Island	8760742	NOAA	https://tidesandcurrents.noaa.gov/stationhome.html?id=8760742	29.8233	-89.2700	3/16/1980	3/3/1982	1.96	5	steel rod	15.7, 19.4	19.4	15.7	15.7	10	Set in Pleistocene
Cypremort Point	8765251	NOAA	https://tidesandcurrents.noaa.gov/stationhome.html?id=8765251	29.7133	-91.8800	8/8/2005	11/11/2010	5.26	5	unspecified pier/rod, seawall						
Deer Island	8764101	NOAA	https://tidesandcurrents.noaa.gov/stationhome.html?id=8764101	29.4733	-91.2667	3/18/1978	11/24/1978	0.69	0							
Devon Energy Bayou, Pass A Loure	8760417	NOAA	https://tidesandcurrents.noaa.gov/stationhome.html?id=8760417	29.2000	-89.0400	4/4/2008	2/10/2009	0.85	5	concrete support beam, steel rod, concrete platform, concrete pier, concrete foundation	unknown	unknown	unknown	unknown	106	91
East Bay, Shell Oil Island, D'Arbonne, Lake Pato	8760781	NOAA	https://tidesandcurrents.noaa.gov/stationhome.html?id=8760781	29.0533	-89.3050	1/8/1985	2/20/1986	1.12	6		14.6	14.6	14.6			
East Timbalier Island	8762223	NOAA	https://tidesandcurrents.noaa.gov/stationhome.html?id=8762223#fides	29.0767	-90.2850	10/28/1986	1/6/1988	1.19	5	steel rod	20.7, 21.9, 23.9, 28.8, 21.9	28.8	20.7	20.7	46	17
Empire, Doullut Canal	8761207	NOAA	https://tidesandcurrents.noaa.gov/stationhome.html?id=8761207	29.3750	-89.6017	7/23/1985	1/2/1991	5.45	0							
Equitable Petroleum Dock, Turtle Bay	8761959	NOAA	https://tidesandcurrents.noaa.gov/stationhome.html?id=8761959	29.5200	-90.1383	10/29/1986	6/13/1987	0.62	0							
Eugene Island	8764311	NOAA	https://tidesandcurrents.noaa.gov/stationhome.html?id=8764311	29.3717	-91.3850	6/1/1959	8/16/2005	66.21	0							
Eugene Island, North of	8764314	NOAA	https://tidesandcurrents.noaa.gov/stationhome.html?id=8764314	29.3667	-91.3833	11/15/2014	10/22/2018	3.93	0							

Avoca Island Cutoff south of Morgan City	03820	USACE	http://nivergates.mvr.usace.army.mil/WaterControl/s/tactioninf02.cfm?sid=03820	29.5333	-91.2494	2/29/1956	3/12/2015	59.03	at least 1	regular concrete	unknown	unknown	(primary benchmark not specified)
Golden Meadow Floodgate (North)	82250	USACE	http://nivergates.mvr.usace.army.mil/WaterControl/s/tactioninf02.cfm?sid=82250	29.3442	-90.2464	3/16/2004	5/8/2014	10.14	at least 1	concrete headwall	unknown	unknown	(primary benchmark not specified)
Golden Meadow Floodgate (South)	82260	USACE	http://nivergates.mvr.usace.army.mil/WaterControl/s/tactioninf02.cfm?sid=82260	29.3425	-90.2464	3/16/2004	5/8/2014	10.14	at least 1	concrete headwall	unknown	unknown	(primary benchmark not specified)
Bayou Des Allendres at Des Allendres	82700	USACE	http://nivergates.mvr.usace.army.mil/WaterControl/s/tactioninf02.cfm?sid=82700	29.8239	-90.4767	5/22/2009	10/22/2018	9.42	at least 1	concrete monument	unknown	unknown	(primary benchmark not specified)
Mississippi River South Pass at Port Eads	01850	USACE	http://nivergates.mvr.usace.army.mil/WaterControl/s/tactioninf02.cfm?sid=01850	28.9323	-89.4071	1/1/1950	7/7/2015	65.51	at least 2	steel rod	0.9	0.9	(primary benchmark not specified)
Lake Pontchartrain at Frenier	85550	USACE	http://nivergates.mvr.usace.army.mil/WaterControl/s/tactioninf02.cfm?sid=85550	30.1061	-90.4214	1/26/1950	6/4/2005	55.35	0				
Calcasieu River and Pass near Cameron Canal at Freshwater	73650	USACE	http://nivergates.mvr.usace.army.mil/WaterControl/s/tactioninf02.cfm?sid=73650	29.7758	-93.3479	1/1/1955	8/14/2005	50.62	unknown	unknown	unknown	unknown	unknown
Bayou Lock - North	76592	USACE	http://nivergates.mvr.usace.army.mil/WaterControl/s/tactioninf02.cfm?sid=76592	29.5547	-92.3046	3/15/2004	10/22/2018	14.60	unknown	unknown	unknown	unknown	unknown
Canal at Freshwater	76593	USACE	http://nivergates.mvr.usace.army.mil/WaterControl/s/tactioninf02.cfm?sid=76593	29.5524	-92.3050	7/28/1968	10/21/2012	44.23	unknown	unknown	unknown	unknown	unknown
Bayou Lock - South	76593	USACE	http://nivergates.mvr.usace.army.mil/WaterControl/s/tactioninf02.cfm?sid=76593	29.5524	-92.3050	7/28/1968	10/21/2012	44.23	unknown	unknown	unknown	unknown	unknown
Schooner Bayou Control Structure - West	76680	USACE	http://nivergates.mvr.usace.army.mil/WaterControl/s/tactioninf02.cfm?sid=76680	29.7578	-92.2642	1/1/1961	1/27/2015	54.07	unknown	unknown	unknown	unknown	unknown
Schooner Bayou Control Structure - East	76600	USACE	http://nivergates.mvr.usace.army.mil/WaterControl/s/tactioninf02.cfm?sid=76600	29.7578	-92.2638	1/1/1955	5/21/2014	59.38	unknown	unknown	unknown	unknown	unknown
IWW at Leland Bowman Lock - West	76800	USACE	http://nivergates.mvr.usace.army.mil/WaterControl/s/tactioninf02.cfm?sid=76800	29.7870	-92.2093	1/1/1951	7/7/2013	62.51	unknown	unknown	unknown	unknown	unknown
IWW at Leland Bowman Lock - East	76720	USACE	http://nivergates.mvr.usace.army.mil/WaterControl/s/tactioninf02.cfm?sid=76720	29.7852	-92.2041	1/1/1959	11/18/2014	55.88	unknown	unknown	unknown	unknown	unknown
Achafalaya Bay at Eugene Island	88600	USACE	http://nivergates.mvr.usace.army.mil/WaterControl/s/tactioninf02.cfm?sid=88600	29.3791	-91.3818	9/30/2008	10/22/2018	10.06	unknown	unknown	unknown	unknown	unknown
Mississippi River at Venice	01480	USACE	http://nivergates.mvr.usace.army.mil/WaterControl/s/tactioninf02.cfm?sid=01480	29.2758	-89.3528	1/15/1953	12/31/2014	61.96	unknown	unknown	unknown	unknown	unknown
Mississippi River at West Bay	01515	USACE	http://nivergates.mvr.usace.army.mil/WaterControl/s/tactioninf02.cfm?sid=01515	29.2401	-89.2984	2/20/2009	10/22/2018	9.67	unknown	unknown	unknown	unknown	unknown
West Bay Receiving Area - Outflow	01516	USACE	http://nivergates.mvr.usace.army.mil/WaterControl/s/tactioninf02.cfm?sid=01516	29.2192	-89.3151	8/14/2008	10/22/2018	10.19	unknown	unknown	unknown	unknown	unknown

Mississippi River at Head of Passes	01545	USACE	http://rivergates.mvr.usac.e.army.mil/WaterControl/s/tationinfo2.cfm?sid=01545	29.1338	-89.2465	4/11/2008	10/22/2018	10.53	unknown	unknown	unknown	unknown	unknown
Mississippi River Southwest Pass Mile 7.5 BHP	01575	USACE	http://rivergates.mvr.usac.e.army.mil/WaterControl/s/tationinfo2.cfm?sid=01575	29.0564	-89.3086	12/9/2010	10/22/2018	7.89	unknown	unknown	unknown	unknown	unknown
Mississippi River Sector Gate - at East Jetty	01670	USACE	http://rivergates.mvr.usac.e.army.mil/WaterControl/s/tationinfo2.cfm?sid=01670	28.9323	-89.4071	1/1/1953	7/7/2015	62.51	unknown	unknown	unknown	unknown	unknown
Bayou DuPre Sector Gate - West/Protected Side	76005	USACE	http://rivergates.mvr.usac.e.army.mil/WaterControl/s/tationinfo2.cfm?sid=76005	29.9346	-89.8372	4/29/2008	10/22/2018	10.48	unknown	unknown	unknown	unknown	unknown
Bayou DuPre Sector Gate - East/Flood Side	76010	USACE	http://rivergates.mvr.usac.e.army.mil/WaterControl/s/tationinfo2.cfm?sid=76010	29.9352	-89.6366	4/29/2008	10/22/2018	10.48	unknown	unknown	unknown	unknown	unknown
Blenville Floodgate - West/Protected Side	76024	USACE	http://rivergates.mvr.usac.e.army.mil/WaterControl/s/tationinfo2.cfm?sid=76024	29.9978	-89.9165	4/29/2008	10/22/2018	10.48	unknown	unknown	unknown	unknown	unknown
Bayou Blenville Floodgate - East/Flood Side	76025	USACE	http://rivergates.mvr.usac.e.army.mil/WaterControl/s/tationinfo2.cfm?sid=76025	29.9987	-89.9153	1/1/2007	10/22/2018	11.81	unknown	unknown	unknown	unknown	unknown
IHC Surge Barrier West/ Protected Side	76032	USACE	http://rivergates.mvr.usac.e.army.mil/WaterControl/s/tationinfo2.cfm?sid=76032	30.0124	-89.9006	2/17/2010	10/22/2018	8.68	unknown	unknown	unknown	unknown	unknown
IHC Surge Barrier East/ Flood Side	76030	USACE	http://rivergates.mvr.usac.e.army.mil/WaterControl/s/tationinfo2.cfm?sid=76030	30.0124	-89.9005	10/15/2010	10/22/2018	8.02	unknown	unknown	unknown	unknown	unknown
Chef Menteur Pass near Lake Bogrie	85750	USACE	http://rivergates.mvr.usac.e.army.mil/WaterControl/s/tationinfo2.cfm?sid=85750	30.0667	-89.8010	10/9/2007	10/22/2018	11.04	unknown	unknown	unknown	unknown	unknown
Rigolets near Lake Pontchartrain	85700	USACE	http://rivergates.mvr.usac.e.army.mil/WaterControl/s/tationinfo2.cfm?sid=85700	30.1634	-89.7379	1/1/1950	8/6/2001	51.59	unknown	unknown	unknown	unknown	unknown
Lake Pontchartrain at Lafayetteville	85575	USACE	http://rivergates.mvr.usac.e.army.mil/WaterControl/s/tationinfo2.cfm?sid=85575	30.3658	-90.0923	8/2/1957	7/26/2002	44.98	unknown	unknown	unknown	unknown	unknown
Pontchartrain at Lakefront	85670	USACE	http://rivergates.mvr.usac.e.army.mil/WaterControl/s/tationinfo2.cfm?sid=85670	30.0399	-90.0188	1/1/2007	10/22/2018	11.81	unknown	unknown	unknown	unknown	unknown
Seabrook Floodgate Closure - Lake Side	76065	USACE	http://rivergates.mvr.usac.e.army.mil/WaterControl/s/tationinfo2.cfm?sid=76065	30.0304	-90.0347	7/19/2012	10/22/2018	6.26	unknown	unknown	unknown	unknown	unknown
Seabrook Floodgate Closure - IHC Side	76062	USACE	http://rivergates.mvr.usac.e.army.mil/WaterControl/s/tationinfo2.cfm?sid=76062	30.0302	-90.0346	7/19/2012	10/22/2018	6.26	unknown	unknown	unknown	unknown	unknown
Seabrook Bridge - Inner Harbor Nav Canal	76060	USACE	http://rivergates.mvr.usac.e.army.mil/WaterControl/s/tationinfo2.cfm?sid=76060	30.0242	-90.0313	5/21/2010	10/22/2018	8.42	unknown	unknown	unknown	unknown	unknown
Bayou St John at Lake Pontchartrain	85634	USACE	http://rivergates.mvr.usac.e.army.mil/WaterControl/s/tationinfo2.cfm?sid=85634	30.0243	-90.0827	4/29/2011	10/22/2018	7.48	unknown	unknown	unknown	unknown	unknown
Lake Pontchartrain at West End	85625	USACE	http://rivergates.mvr.usac.e.army.mil/WaterControl/s/tationinfo2.cfm?sid=85625	30.0222	-90.1156	3/10/1949	12/31/2014	65.81	unknown	unknown	unknown	unknown	unknown

Lake Pontchartrain at Bonnet Carré Spillway	85555	USACE	http://nrivergates.mvr.usace.army.mil/WaterControl/s/tationinf02.cfm?id=85555&id=8dt=S	30.0559	-90.3722	1/1/2007	5/20/2011	4.38	unknown	unknown	unknown	unknown
Pass Manchac near Pontchartrain	85420	USACE	http://nrivergates.mvr.usace.army.mil/WaterControl/s/tationinf02.cfm?id=85420&id=8dt=S	30.2814	-90.4003	4/17/2009	10/22/2018	9.51	unknown	unknown	unknown	unknown
Cattfish Point Control Structure - North	70675	USACE	http://nrivergates.mvr.usace.army.mil/WaterControl/s/tationinf02.cfm?id=70675&id=8dt=S	29.8636	-92.8484	1/1/1955	3/12/2015	60.19	unknown	unknown	unknown	unknown
Cattfish Point Control Structure - South	70750	USACE	http://nrivergates.mvr.usace.army.mil/WaterControl/s/tationinf02.cfm?id=70750&id=8dt=S	29.8629	-92.8492	1/1/1955	3/12/2015	60.19	unknown	unknown	unknown	unknown
Inner Harbor Navigation Canal (IHNC) Lock New Orleans	76160	USACE	http://nrivergates.mvr.usace.army.mil/WaterControl/s/tationinf02.cfm?id=76160&id=8dt=S	29.9665	-90.0268	1/1/1945	3/12/2015	70.19	unknown	unknown	unknown	unknown
Bayou Beaufort Lock - East	76360	USACE	http://nrivergates.mvr.usace.army.mil/WaterControl/s/tationinf02.cfm?id=76360&id=8dt=S	29.6830	-91.1711	9/8/1954	3/12/2015	60.51	unknown	unknown	unknown	unknown
Calcasieu Lock - West	76960	USACE	http://nrivergates.mvr.usace.army.mil/WaterControl/s/tationinf02.cfm?id=76960&id=8dt=S	30.0887	-93.2949	1/1/1951	8/27/2014	63.65	unknown	unknown	unknown	unknown
Mississippi River at New Orleans (Carrollton)	01300	USACE	http://nrivergates.mvr.usace.army.mil/WaterControl/s/tationinf02.cfm?id=01300&id=8dt=S	29.9347	-90.1361	1/1/1950	1/1/2015	65.00	unknown	unknown	unknown	unknown
Mississippi River at IHNC Lock	01340	USACE	http://nrivergates.mvr.usace.army.mil/WaterControl/s/tationinf02.cfm?id=01340&id=8dt=S	29.9644	-90.0274	1/1/1945	1/27/2015	70.07	unknown	unknown	unknown	unknown
Mississippi River at West Pointe à la Hache	01400	USACE	http://nrivergates.mvr.usace.army.mil/WaterControl/s/tationinf02.cfm?id=01400&id=8dt=S	29.5711	-89.7969	1/1/1950	12/31/2014	65.00	unknown	unknown	unknown	unknown
Calcasieu River & Pass at Lake Charles	73550	USACE	http://nrivergates.mvr.usace.army.mil/WaterControl/s/tationinf02.cfm?id=73550&id=8dt=S	30.2131	-93.2569	1/1/1950	7/7/2003	53.51	unknown	unknown	unknown	unknown
GIWW at Houma	76320	USACE	http://nrivergates.mvr.usace.army.mil/WaterControl/s/tationinf02.cfm?id=76320&id=8dt=S	29.5961	-90.7100	1/1/1959	11/17/2008	49.88	unknown	unknown	unknown	unknown
Bayou Lafourche at Leesville	82350	USACE		29.2478	-90.2089	11/4/1955	4/8/2000	44.43	unknown	unknown	unknown	unknown
Bayou Baratania at Baratania	82750	USACE	http://nrivergates.mvr.usace.army.mil/WaterControl/s/tationinf02.cfm?id=82750&id=8dt=S	29.7414	-90.1322	1/6/1950	11/12/1992	42.85	unknown	unknown	unknown	unknown
Bayou Terre Aux Boeufs at Delacroix, La. MRGO at Shell Beach	85780	USACE	http://nrivergates.mvr.usace.army.mil/WaterControl/s/tationinf02.cfm?id=85780&id=8dt=S	29.7639	-89.7922	5/15/1975	8/28/2005	30.29	unknown	unknown	unknown	unknown
	85800	USACE	http://nwis.waterdata.usgs.gov/nwis/inventory/site_no=08017118&agency_cd=USGS	29.8500	-89.6833	6/30/1961	12/16/2002	41.46	unknown	unknown	unknown	unknown
Calcasieu River	08017118	USGS	http://nwis.waterdata.usgs.gov/nwis/inventory/site_no=08017118&agency_cd=USGS	29.8156	-93.3489	10/1/2007	10/22/2018	11.06	unknown	unknown	unknown	unknown
Caillou Bay	07381349	USGS	http://waterdata.usgs.gov/la/nwis/uv/?site_no=07381349&agency_cd=USGS	29.0781	-90.8714	10/1/2007	10/22/2018	11.06	unknown	unknown	unknown	unknown
Black Bay	07374527	USGS	http://waterdata.usgs.gov/nwis/uv/?site_no=07374527&agency_cd=USGS	29.5693	-89.5122	5/21/2014	10/22/2018	4.42	unknown	unknown	unknown	unknown
Crooked Bayou	07374525	USGS	http://waterdata.usgs.gov/nwis/uv/?site_no=07374525&agency_cd=USGS	29.7081	-89.7194	10/1/2007	10/22/2018	11.06	unknown	unknown	unknown	unknown

Cow Bayou at American Bay	07374525 B	USGS	http://waterdata.usgs.gov/nwis/inventory/?site_no=07374525	29.5706	-89.7039	1/28/1999	10/22/2018	19.73	unknown	unknown	unknown	unknown	unknown (primary benchmark not specified)
Barataria Pass at Grand Isle	07380251 S	USGS	http://waterdata.usgs.gov/nwis/uv/?site_no=07380251&agency_cd=USGS	29.2728	-89.9468	10/1/2008	10/22/2018	10.06	at least 1	concrete retaining wall	unknown	unknown	unknown
Mouth of Atchafalaya River	07381652 S	USGS	http://waterdata.usgs.gov/nwis/uv/?site_no=07381652&agency_cd=USGS	29.4303	-91.3339	5/21/2015	10/22/2018	3.42	unknown	unknown	unknown	unknown	unknown
Crewboat Channel at Wax Lake Outlet	07381592 S	USGS	http://waterdata.usgs.gov/nwis/inventory/?site_no=07381592&agency_cd=USGS	29.5400	-91.4356	10/1/2002	10/22/2018	16.06	unknown	unknown	unknown	unknown	unknown
Vermilion Bay	07387040	USGS	http://waterdata.usgs.gov/nwis/uv/?site_no=07387040&agency_cd=USGS	29.7131	-91.8803	10/23/1997	10/22/2018	21.00	unknown	unknown	unknown	unknown	unknown
Vermilion Bay Bayou Farman Lower Atchafalaya River at Morgan City	07387050 07381600	USGS	http://waterdata.usgs.gov/nwis/uv/?site_no=07387050&agency_cd=USGS&multi_referenced_module=sw	29.6744	-92.1356	10/1/1999	10/22/2018	19.06	unknown	unknown	unknown	unknown	unknown
Calumet (Wax Lake Outlet)	07381590	USGS	http://waterdata.usgs.gov/nwis/uv/?site_no=07381590&agency_cd=USGS	29.6926	-91.2118	10/1/1992	9/30/2015	23.00	unknown	unknown	unknown	unknown	unknown
North Calcasieu Lake (Hackberry)	08017095	USGS	http://waterdata.usgs.gov/nwis/uv/?site_no=08017095&parameter_cd=000	29.6978	-91.3728	10/1/1995	9/30/2015	20.00	unknown	unknown	unknown	unknown	unknown
				30.0317	-93.2994	7/26/1997	10/22/2018	21.24	unknown	unknown	unknown	unknown	unknown

Table A2.2. Information on 17 GNSS stations in coastal Louisiana.

GNSS station code	Latitude	Longitude	Foundation depth (m)	Depth to Pleistocene surface (m)	Benchmark foundation height above Pleistocene surface (m)
AWES	30.10	-90.98	1	29	28
BVHS	29.34	-89.41	>20	62	<42
CAMR	29.80	-93.33	unknown		
DSTR	29.96	-90.38	unknown		
ENG1	29.88	-89.94	~3	27	~24
ENG2	29.88	-89.94	~3	27	~24
FRAN	29.80	-91.53	14.7	10	Set in Pleistocene
FSHS	29.81	-91.50	1	15	14
GRIS	29.27	-89.96	unknown		
HOMA	29.57	-90.76	18.3	40	21.7
HOUM	29.59	-90.72	>15	40	<25
LAFR	29.79	-91.50	unknown		
LMCN	29.25	-90.66	36.5	57	20.5
LWES	29.90	-90.35	unknown		
MSSC	30.38	-89.61	unknown		
NDBC	30.36	-89.61	unknown		
VENI	29.28	-89.36	30.5	78	47.5

APPENDIX III

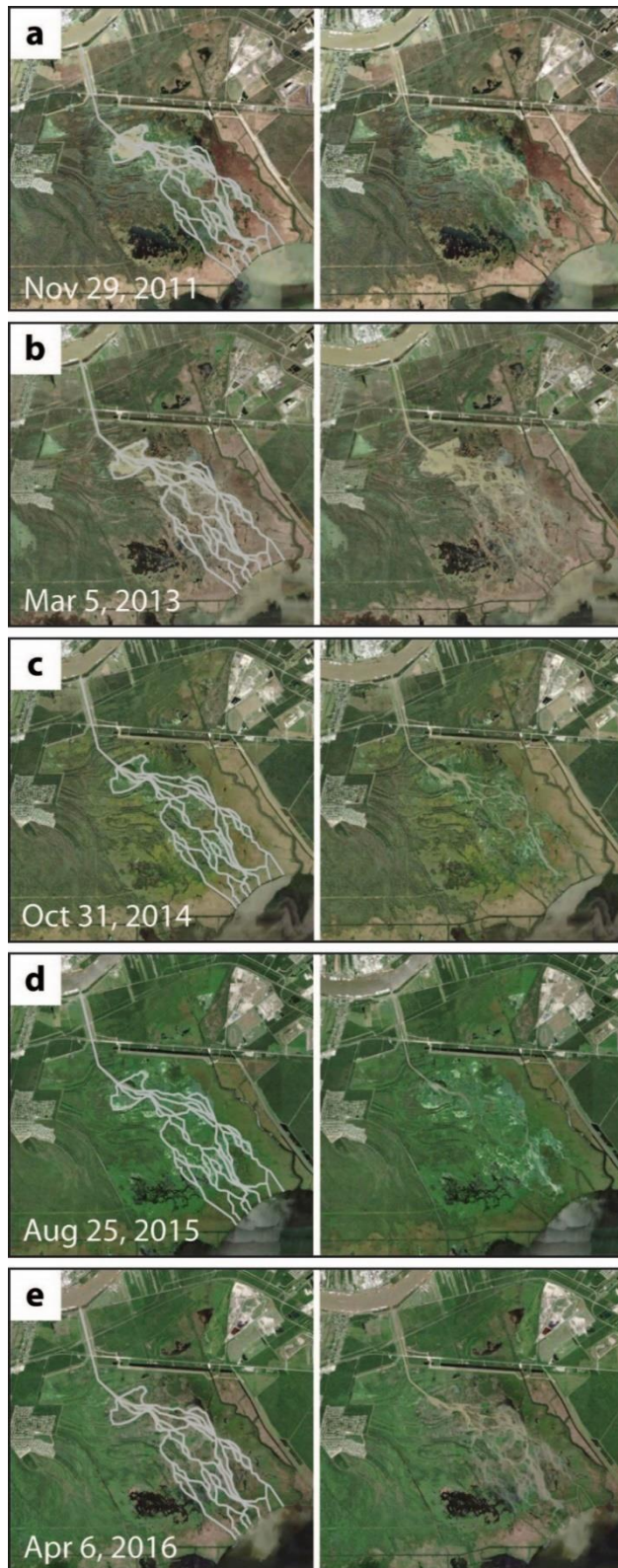


Figure A3.1. Satellite imagery of the Davis Pond receiving basin from November 29, 2011 (a), March 5, 2013 (b), October 31, 2014 (c), August 25, 2015 (d), and April 6, 2016 (e). In each panel, the satellite image on the left is overlain by the outline of the main channels used in Figure 3.4 in the main text. The satellite images on the right are un-annotated. The main channels in Davis Pond are stable over the timescales relevant to this study (months to years) and channel geometry did not change appreciably in the five years surrounding the study period (Nov. 2014 – Oct. 2015). Satellite imagery modified from Google Earth.

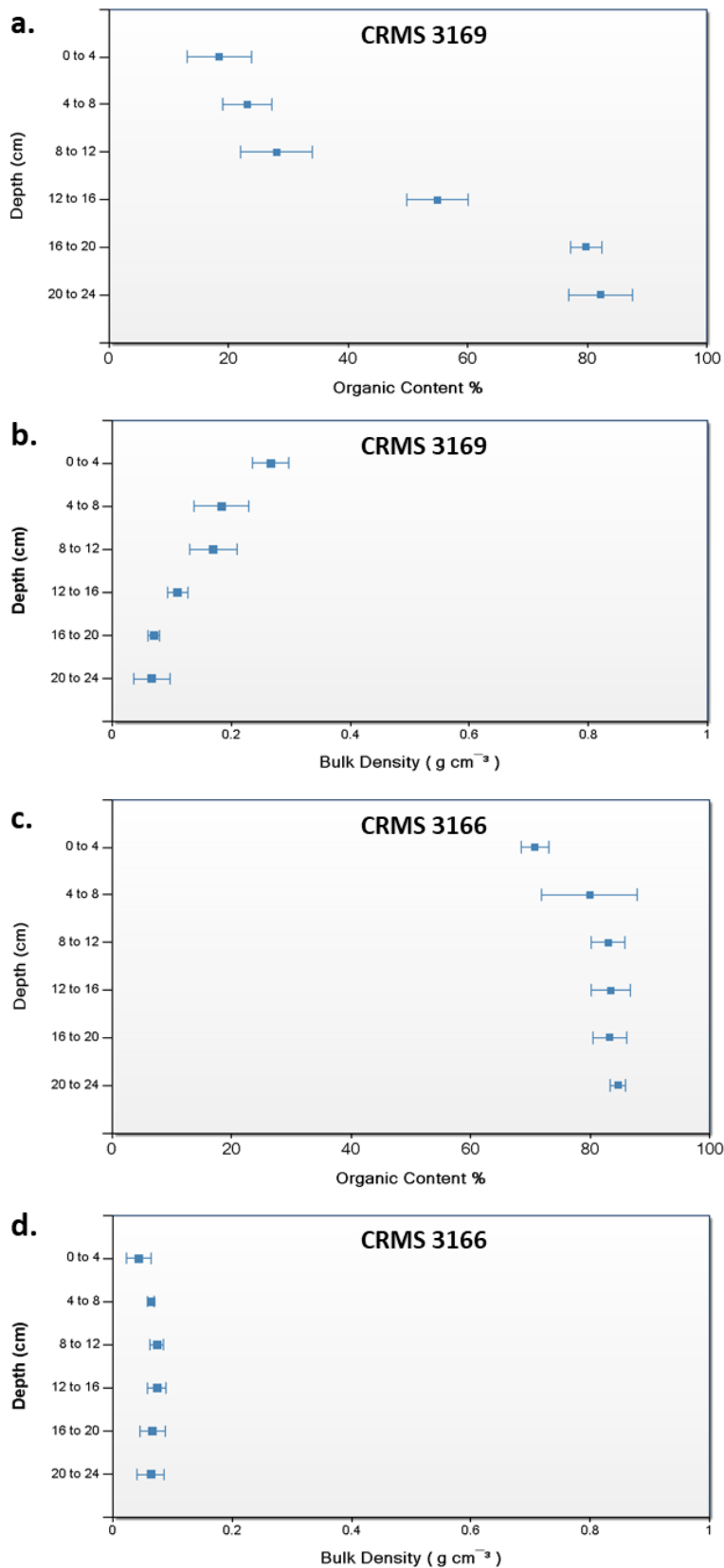


Figure A3.2. Bulk density and organic content data from the top 24 cm of soil at two Coastwide Reference Monitoring System (CMRS) stations located within the receiving basin of the Davis Pond Freshwater Diversion. The soil at CRMS station 3169, which is within the coring area of the present study, shows distinct surface-ward trends of decreasing organic content (a) and increasing bulk density (b), suggesting input of mineral-rich sediment from the diversion. At CRMS station 3166, which is outside the coring area of the present study, the soil has consistently high organic content (c) and low bulk density (d), suggesting little to no input from the diversion.

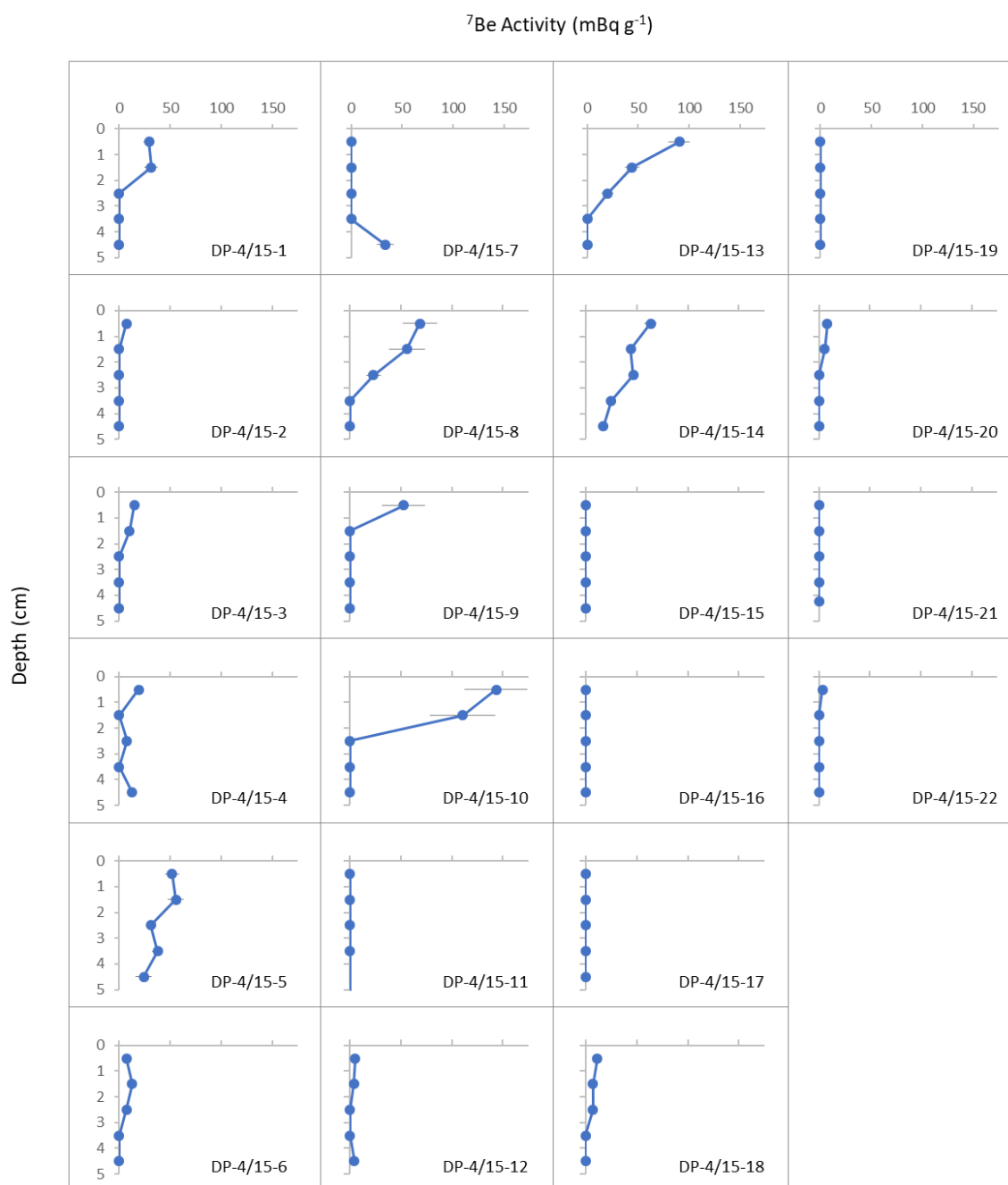


Figure A3.3. ^7Be activity vs. depth profiles for the 22 sediment cores collected in April 2015. Note that when an interval containing measurable ^7Be occurred below an interval with no measurable ^7Be (e.g. as seen in core DP-4/15-7), the ^7Be in the deeper interval was not used for analysis.

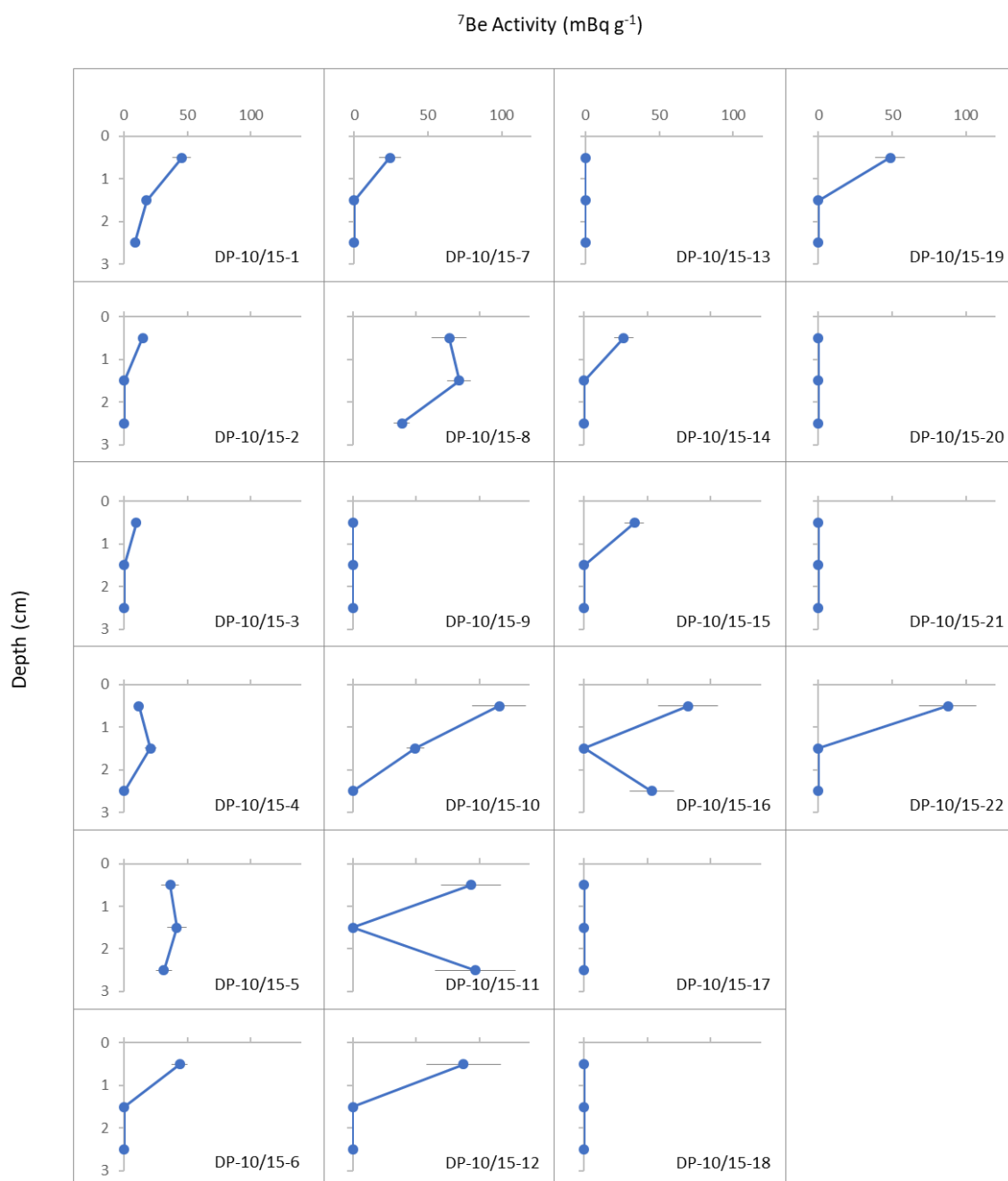


Figure A3.4. ^7Be activity vs. depth profiles for the 22 sediment cores collected in October 2015. Note that when an interval containing measurable ^7Be occurred below an interval with no measurable ^7Be (e.g. as seen in core DP-10/15-16), the ^7Be in the deeper interval was not used for analysis.

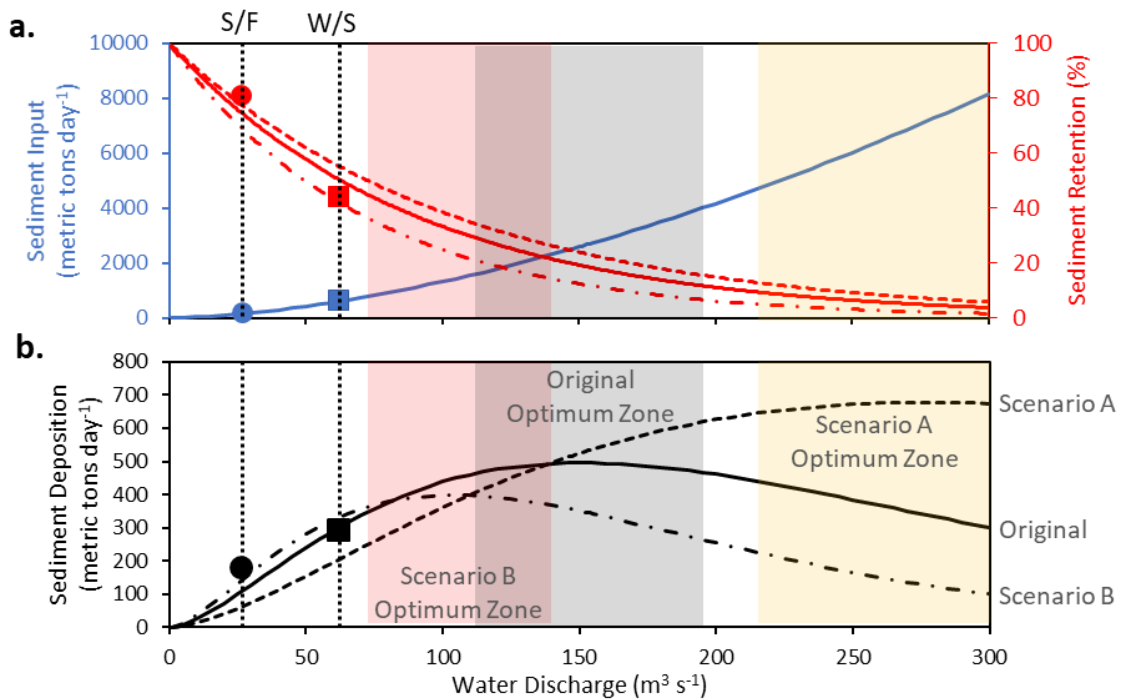


Figure A3.5. Changes to the conceptual model (Figure 3.8) that could result from hypothetical additional data. Adjustments to the best-fit exponential curve representing sediment retention (red curves, panel a) result in different sediment deposition curves (corresponding black curves, panel b), each with a different zone of optimum water discharge. Although the optimum zone shifts dramatically, it continues to exist. As long as the sediment deposition curve remains convex-up, there will be a corresponding optimum water discharge, above which higher discharges will lead to decreasing sediment deposition and retention. Solid lines indicating sediment input (blue), retention (red), and deposition (black, “Original” curve) are the same as in Figure 3.8 in the main text. Circles and squares indicate measured values from the summer/fall (S/F) and winter/spring (W/S) study seasons, respectively.

In panel a, the three sediment retention curves (shown in red) are exponential functions with a y-intercept of 100% and the following equations:

Original (solid line): $y = 100e^{-0.011x}$

Scenario A (dashed line): $y = 100e^{-0.010x}$

Scenario B (dash-dot line): $y = 100e^{-0.014x}$

The equations for Scenario A and B were selected in order to bracket the original exponential equation.

Table A3.1. Mean mineral content of Mississippi River suspended sediment. As part of a previous study of the Caernarvon Freshwater Diversion (Snedden et al. 2007), TSS concentrations and loss-on-ignition were determined from water samples obtained at four depths along five equally-spaced vertical transects across the diversion outfall channel that conveys diverted river water into the Breton Sound estuary immediately (~100m) downstream of the Caernarvon diversion structure. This procedure was performed on five dates under discharge conditions ranging from 0 to ~200 m³ s⁻¹. The TSS concentrations were reported in Table 1 of Snedden et al. 2007; the loss-on-ignition values were not. They are reported here. For each date in the table presented here, the cross-sectional average and standard deviation of mineral sediment concentration (mg L⁻¹) and mineral content (%) are reported. The average mineral content across all five dates was 81.54%.

Date	Caernarvon water discharge (m ³ s ⁻¹)	Mineral sediment concentration (mg L ⁻¹)		Mineral content (%)	
		Mean	Standard deviation	Mean	Standard deviation
1/23/2002	0	25.93	5.58	84.25	3.19
2/7/2002	152	177.00	8.83	90.97	0.53
2/28/2002	19	46.67	8.01	91.28	1.24
3/14/2002	189	7.88	2.52	53.55	4.05
4/10/2002	16	62.04	16.41	87.78	2.25
overall:		64.33	60.70	81.54	14.62

Table A3.2. Collection date and location of sediment cores

Core ID	Date Collected	Latitude	Longitude
DP-4/15-1	4/21/2015	29.9056	-90.3015
DP-4/15-2	4/21/2015	29.9037	-90.3066
DP-4/15-3	4/21/2015	29.9038	-90.3069
DP-4/15-4	4/21/2015	29.8999	-90.3088
DP-4/15-5	4/21/2015	29.8970	-90.3005
DP-4/15-6	4/21/2015	29.9019	-90.2952
DP-4/15-7	4/21/2015	29.8983	-90.2763
DP-4/15-8	4/21/2015	29.8950	-90.2830
DP-4/15-9	4/21/2015	29.8865	-90.2921
DP-4/15-10	4/21/2015	29.8765	-90.2834
DP-4/15-11	4/21/2015	29.8671	-90.2738
DP-4/15-12	4/21/2015	29.8695	-90.2700
DP-4/15-13	4/21/2015	29.8810	-90.2767

DP-4/15-14	4/21/2015	29.8906	-90.2874
DP-4/15-15	4/21/2015	29.8844	-90.2721
DP-4/15-16	4/21/2015	29.8722	-90.2630
DP-4/15-17	4/21/2015	29.8879	-90.2635
DP-4/15-18	4/21/2015	29.8766	-90.2551
DP-4/15-19	4/21/2015	29.8582	-90.2610
DP-4/15-20	4/21/2015	29.8620	-90.2548
DP-4/15-21	4/21/2015	29.8568	-90.2499
DP-4/15-22	4/21/2015	29.8668	-90.2471
DP-10/15-1	10/15/2015	29.9056	-90.3014
DP-10/15-2	10/15/2015	29.9039	-90.3069
DP-10/15-3	10/15/2015	29.9039	-90.3069
DP-10/15-4	10/15/2015	29.9000	-90.3089
DP-10/15-5	10/15/2015	29.8969	-90.3003
DP-10/15-6	10/15/2015	29.9017	-90.2950
DP-10/15-7	11/4/2015	29.8956	-90.2772
DP-10/15-8	10/15/2015	29.8953	-90.2828
DP-10/15-9	10/15/2015	29.8864	-90.2919
DP-10/15-10	10/15/2015	29.8764	-90.2836
DP-10/15-11	10/15/2015	29.8644	-90.2728
DP-10/15-12	11/4/2015	29.8694	-90.2703
DP-10/15-13	10/15/2015	29.8811	-90.2769
DP-10/15-14	10/15/2015	29.8906	-90.2872
DP-10/15-15	10/15/2015	29.8843	-90.2719
DP-10/15-16	11/4/2015	29.8722	-90.2628
DP-10/15-17	10/15/2015	29.8894	-90.2653
DP-10/15-18	10/15/2015	29.8761	-90.2542
DP-10/15-19	10/14/2015	29.8572	-90.2608
DP-10/15-20	10/14/2015	29.8619	-90.2547
DP-10/15-21	10/14/2015	29.8558	-90.2478
DP-10/15-22	10/14/2015	29.8667	-90.2481

Table A3.3. Winter/spring sediment core data

Core ID	Depth interval (cm)	Water content (% by mass)	Loss on ignition (%)	Bulk density (g cm ⁻³)	⁷ Be activity (mBq g ⁻¹)	⁷ Be activity error (mBq g ⁻¹)	Mineral accumulation (g cm ⁻²)	Total mineral accumulation per core, <i>sed_{core}</i> (g cm ⁻²)
DP-4/15-1	0-1	62.7887	8.0847	0.3595	29.1507	5.0812	0.33	0.62
	1-2	66.4373	10.6049	0.3210	31.2504	6.4438	0.29	

	2-3	67.1964	11.7011	0.3121	0		0	
	3-4	69.5721	14.0504	0.2868	0		0	
	4-5	67.9471	14.3737	0.3003	0		0	
DP-4/15-2	0-1	31.3380	3.5185	0.6670	7.0706	4.8010	0.64	0.64
	1-2	29.6239	3.6210	0.6821	0		0	
	2-3	28.6675	3.9962	0.6881	0		0	
	3-4	27.8662	3.9243	0.6960	0		0	
	4-5	28.6651	4.2411	0.6863	0		0	
DP-4/15-3	0-1	25.9287	3.6744	0.7156	14.6955	2.6923	0.69	1.34
	1-2	29.3939	4.2836	0.6794	10.0076	3.2609	0.65	
	2-3	28.2277	4.0580	0.6917	0		0	
	3-4	31.2785	5.1685	0.6561	0		0	
	4-5	27.9288	4.0923	0.6941	0		0	
DP-4/15-4	0-1	56.5078	6.9364	0.4199	19.0549	4.6583	0.39	0.39
	1-2	47.3652	5.8568	0.5072	0		0	
	2-3	40.9904	5.2786	0.5679	7.5730	3.2672	0	
	3-4	40.5768	5.6245	0.5698	0		0	
	4-5	50.4947	8.0617	0.4701	12.3457	3.4688	0	
DP-4/15-5	0-1	63.2757	8.0239	0.3551	51.7745	6.9958	0.33	1.58
	1-2	63.1362	9.0307	0.3541	55.4473	7.6063	0.32	
	2-3	62.5689	9.2193	0.3588	30.7764	4.6248	0.33	
	3-4	62.1010	10.3120	0.3603	37.5286	5.4151	0.32	
	4-5	66.0779	12.9816	0.3193	23.9511	7.7074	0.28	
DP-4/15-6	0-1	87.8802	27.5449	0.1145	7.1757	2.3024	0.08	0.28
	1-2	85.4374	28.2258	0.1350	12.7497	3.4018	0.10	
	2-3	85.0649	29.9687	0.1369	7.2292	3.4490	0.10	
	3-4	82.7112	29.0745	0.1568	0		0	
	4-5	79.2263	26.1479	0.1881	0		0	
DP-4/15-7	0-1	88.1046	28.7948	0.1119	0		0	0
	1-2	87.0233	30.9322	0.1199	0		0	
	2-3	86.1971	30.0718	0.1274	0		0	
	3-4	85.0814	28.6540	0.1377	0		0	
	4-5	80.6096	24.5513	0.1786	33.3544	7.8182	0	
DP-4/15-8	0-1	85.0245	17.4923	0.1451	68.7449	16.6450	0.12	0.38
	1-2	84.2408	20.0943	0.1508	55.8371	17.4245	0.12	
	2-3	81.8745	18.9046	0.1728	23.1846	6.7175	0.14	
	3-4	79.9640	19.2771	0.1893	0		0	
	4-5	78.3067	18.3320	0.2047	0		0	
DP-4/15-9	0-1	88.7847	26.2821	0.1070	52.7137	21.0643	0.08	0.08
	1-2	82.0483	22.7305	0.1681	0		0	
	2-3	79.4172	21.6690	0.1916	0		0	

	3-4	77.7928	20.9594	0.2062	0		0	
	4-5	75.4588	20.2954	0.2267	0		0	
DP-4/15-10	0-1	88.2992	38.0716	0.1048	143.5070	30.6735	0.06	0.13
	1-2	87.6794	38.9113	0.1090	110.8580	31.9069	0.07	
	2-3	87.0772	40.0587	0.1126	0		0	
	3-4	86.8608	43.3553	0.1108	0		0	
	4-5	86.7949	45.6911	0.1085	0		0	
DP-4/15-11	0-1	83.1233	44.1941	0.1342	0		0	0
	1-2	84.9375	51.9469	0.1088	0		0	
	2-3	84.7749	50.9020	0.1119	0		0	
	3-4	82.8321	45.0808	0.1344	0		0	
	4-7	86.4535	52.6480	0.0994	0		0	
DP-4/15-12	0-1	88.1515	26.5938	0.1125	5.3077	2.5291	0.08	0.20
	1-2	83.6457	24.3287	0.1531	4.1675	2.4388	0.12	
	2-3	83.1074	25.0707	0.1571	0		0	
	3-4	81.4885	23.9563	0.1718	0		0	
	4-5	82.2175	26.8996	0.1629	4.2727	2.5857	0	
DP-4/15-13	0-1	70.8651	14.8919	0.2741	90.2321	10.4410	0.23	0.67
	1-2	72.4586	16.6217	0.2576	44.1798	6.8737	0.21	
	2-3	71.5801	16.1952	0.2658	20.1282	5.6563	0.22	
	3-4	71.2356	15.8568	0.2693	0		0	
	4-5	68.0012	15.5624	0.2974	0		0	
DP-4/15-14	0-1	58.8365	7.7724	0.3963	63.4783	5.9287	0.37	1.83
	1-2	53.3006	7.6061	0.4468	44.0947	4.6819	0.41	
	2-3	54.3391	9.3968	0.4314	46.5830	4.5105	0.39	
	3-4	58.2120	11.3059	0.3916	24.9850	3.9008	0.35	
	4-5	60.4645	13.3762	0.3663	17.2941	4.6373	0.32	
DP-4/15-15	0-1	66.4873	15.3773	0.3106	0		0	0
	1-2	65.8617	15.2409	0.3162	0		0	
	2-3	66.0983	15.1216	0.3145	0		0	
	3-4	64.9285	14.7453	0.3252	0		0	
	4-5	63.7045	14.4467	0.3362	0		0	
DP-4/15-16	0-1	53.3431	18.9504	0.4029	0		0	0
	1-2	51.8254	17.2088	0.4216	0		0	
	2-3	49.4390	15.4259	0.4476	0		0	
	3-4	48.2136	14.0746	0.4634	0		0	
	4-5	47.1715	13.0802	0.4763	0		0	
DP-4/15-17	0-1	77.9817	36.1644	0.1819	0		0	0
	1-2	81.9005	45.4797	0.1391	0		0	
	2-3	84.1212	46.8921	0.1234	0		0	
	3-4	85.5156	48.9177	0.1116	0		0	

	4-5	85.9458	50.0000	0.1072	0		0	
DP-4/15-18	0-1	74.4206	24.7505	0.2282	11.4910	2.9877	0.17	0.45
	1-2	77.3284	29.5290	0.1981	6.9570	2.5260	0.14	
	2-3	77.2217	30.6411	0.1970	6.8869	3.6526	0.14	
	3-4	76.6994	30.2536	0.2015	0		0	
	4-5	76.5910	30.9249	0.2012	0		0	
DP-4/15-19	0-1	75.4984	25.3482	0.2188	0		0	0
	1-2	76.6710	23.5409	0.2121	0		0	
	2-3	79.8656	30.5893	0.1774	0		0	
	3-4	76.0613	27.5551	0.2108	0		0	
	4-5	72.0542	22.1932	0.2513	0		0	
DP-4/15-20	0-1	74.4513	21.3549	0.2335	7.9904	3.2389	0.18	0.36
	1-2	75.8885	22.1320	0.2205	5.5130	4.3468	0.17	
	2-3	78.0348	24.3350	0.2000	0		0	
	3-4	82.5439	33.8753	0.1530	0		0	
	4-5	83.9718	44.0109	0.1292	0		0	
DP-4/15-21	0-1	73.2387	14.7011	0.2537	0		0	0
	1-2	70.1710	13.8622	0.2819	0		0	
	2-3	72.4309	15.0127	0.2603	0		0	
	3-4	62.9122	17.1774	0.3356	0		0	
	4-4.5	71.4214	13.5390	0.2714	0		0	
DP-4/15-22	0-1	75.7165	16.2521	0.2298	3.2344	2.7324	0.19	0.19
	1-2	73.4007	16.2487	0.2500	0		0	
	2-3	73.2973	16.0166	0.2512	0		0	
	3-4	74.9797	17.1504	0.2351	0		0	
	4-5	75.8304	18.1730	0.2264	0		0	

Table A3.4. Summer/fall sediment core data

Core ID	Depth interval (cm)	Water content (% by mass)	Loss on ignition (%)	Bulk density (g cm ⁻³)	⁷ Be activity (mBq g ⁻¹)	⁷ Be activity error (mBq g ⁻¹)	Mineral accumulation (g cm ⁻²)	Total mineral accumulation per core, <i>sed_{core}</i> (g cm ⁻²)
DP-10/15-1	0-1	78.9302	11.9584	0.2052	45.6763	7.0149	0.18	1.02
	1-2	64.4450	8.2204	0.3440	17.6725	2.8378	0.32	
	2-3	40.1716	7.3957	0.5638	8.6781	2.9096	0.52	
DP-10/15-2	0-1	34.0756	6.3021	0.6236	14.6544	2.4404	0.58	0.58
	1-2	36.9491	8.2857	0.5863	0		0	
	2-3	41.8154	11.4205	0.5277	0		0	

DP-10/15-3	0-1	24.9385	2.3295	0.7356	9.5808	2.2786	0.72	0.72
	1-2	25.2590	2.4768	0.7314	0		0	
	2-3	24.4659	2.4443	0.7391	0		0	
DP-10/15-4	0-1	59.9266	8.1332	0.3854	11.8123	3.3972	0.35	0.76
	1-2	54.9344	6.9335	0.4343	21.0485	4.6720	0.40	
	2-3	51.3390	6.9541	0.4668	0		0	
DP-10/15-5	0-1	73.0110	13.1330	0.2579	36.4140	7.0058	0.22	0.86
	1-2	67.7251	11.7129	0.3074	41.7632	7.3251	0.27	
	2-3	57.5066	9.7330	0.4025	31.4341	6.1480	0.36	
DP-10/15-6	0-1	80.4998	16.8868	0.1867	43.9240	6.0162	0.16	0.16
	1-2	76.5262	15.1042	0.2240	0		0	
	2-3	75.5793	15.6716	0.2317	0		0	
DP-11/15-7	0-1	64.2227	14.1580	0.3325	24.2568	7.2681	0.29	0.29
	1-2	59.6198	13.1283	0.3742	0		0	
	2-3	56.6312	13.0060	0.3995	0		0	
DP-10/15-8	0-1	84.8810	17.9767	0.1462	76.2683	13.6676	0.12	0.50
	1-2	79.6887	15.5932	0.1951	84.0434	9.0803	0.16	
	2-3	74.4572	12.8065	0.2453	38.8017	5.9208	0.21	
DP-10/15-9	0-1	74.0070	16.4659	0.2444	0		0	0.00
	1-2	76.4139	18.0133	0.2216	0		0	
	2-3	70.7848	15.1931	0.2743	0		0	
DP-10/15-10	0-1	84.1582	55.1755	0.1041	115.6265	21.2160	0.05	0.11
	1-2	82.4628	49.0050	0.1283	49.4961	6.7260	0.07	
	2-3	87.3010	57.5095	0.0842	0		0	
DP-10/15-11	0-1	87.3197	57.0858	0.0852	93.4572	23.7078	0.04	0.04
	1-2	83.7181	42.7606	0.1328	0		0	
	2-3	85.4766	46.2413	0.1162	96.9651	31.5201	0	
DP-11/15-12	0-1	89.3844	28.8150	0.1007	87.4577	29.2888	0.07	0.07
	1-2	87.8373	27.1417	0.1150	0		0	
	2-3	86.3929	25.5408	0.1285	0		0	
DP-10/15-13	0-1	70.4239	13.1618	0.2809	0		0	0.00
	1-2	76.0672	16.5468	0.2264	0		0	
	2-3	74.2665	16.2480	0.2425	0		0	
DP-10/15-14	0-1	49.2930	9.8545	0.4732	31.3160	7.5534	0.43	0.43
	1-2	44.1711	8.7326	0.5222	0		0	
	2-3	42.6371	8.5515	0.5363	0		0	
DP-10/15-15	0-1	64.0194	15.9902	0.3297	39.6994	7.4132	0.28	0.28
	1-2	55.3445	13.1621	0.4097	0		0	
	2-3	65.7061	17.9975	0.3110	0		0	
DP-11/15-16	0-1	85.5796	36.9110	0.1268	82.1468	23.2179	0.08	0.08

	1-2	85.5932	37.7820	0.1258	0		0	
	2-3	85.9421	39.2857	0.1217	53.4043	17.2705	0	
DP-10/15-17	0-1	87.3755	44.3340	0.1061	0		0	0.00
	1-2	84.8020	38.0872	0.1314	0		0	
	2-3	84.1157	37.3824	0.1372	0		0	
DP-10/15-18	0-1	73.7444	35.0448	0.2120	0		0	0.00
	1-2	69.8653	26.1111	0.2598	0		0	
	2-3	70.9203	26.0518	0.2522	0		0	
DP-10/15-19	0-1	72.0044	14.3994	0.2650	48.6378	9.9155	0.23	0.23
	1-2	77.6941	22.2047	0.2055	0		0	
	2-3	82.4236	32.2774	0.1557	0		0	
DP-10/15-20	0-1	56.3981	10.8780	0.4085	0		0	0.00
	1-2	73.4470	21.5503	0.2413	0		0	
	2-3	74.2759	24.4898	0.2298	0		0	
DP-10/15-21	0-1	76.5811	14.1961	0.2245	0		0	0.00
	1-2	69.8514	13.0601	0.2861	0		0	
	2-3	70.5833	13.9124	0.2782	0		0	
DP-10/15-22	0-1	72.1298	15.3409	0.2624	87.7644	19.1794	0.22	0.22
	1-2	70.0316	13.7322	0.2834	0		0	
	2-3	69.7125	13.3667	0.2868	0		0	

BIOGRAPHY

Margaret Elizabeth Herring Keogh was born and raised in Oregon and developed an appreciation for rocks at an early age. Molly went on to study geology at the University of Oregon, graduating *magna cum laude* in 2010 with a B.S. in Geological Sciences and a minor in Biology. After college, Molly worked in environmental consulting before returning to graduate school to study coastal geology at Tulane University. In 2019, she earned her Ph.D. in Earth and Environmental Sciences under the guidance of Dr. Alexander Kolker and Dr. Torbjörn Törnqvist. Molly will go on to a career studying coastal landscape change and its impact on people.